LATVIJAS UNIVERSITATE

DOCTORAL THESIS

Nonlinear crack problems with application to composites and geomechanics

Sergejs Tarasovs

University of Latvia
Institute of Polymer Mechanics

Riga 2008

Sergejs Tarasovs

Nelineāras plaisu problēmas ar pielietojumiem kompozītos un ģeomehānikā

Nonlinear crack problems with application to composites and geomechanics

Zinātnisku publikāciju kopa / Scientific papers

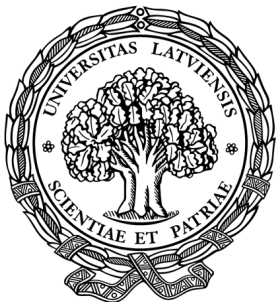

Latvijas Universitāte / University of Latvia

Rīga — 2008

Table of contents

Anotācija

Nelineāru problēmu risinājums mehānikā parasti ir sarežģīts uzdevums. Tas prasa lielu darba ieguldījumu analītiskajā un skaitliskajā risinājuma daļā (analītiskais risinājums lielākai problēmu daļai neeksistē). Šīs darbs ietver sevī nelineāru problēmu risinājumu ieskaitot plaisu izplatīšanos un materiāla sabrukšanu.

Darba pirmā daļā tika izstrādāta eksperimentāla metodika ar mērķi noskaidrot vienvirziena un transversāli stiegrotu kompozītu atslāņošanas īpašības. Šķērssaišu likums, kas var tikt aprēķināts, izmantojot eksperimentālus datus tiek uzskaitīts par svarīgu materiāla īpašību. Vienkārša skaitliska procedūra ar iepriekšnoteiktu šķērssaišu likuma izmantošanu ir ierosināta plaisu palielināšanās slāņainos kompozītos simulēšanai.

Darba otrā daļā tiek piedāvāts trīsdimensiju matemātiskais modelis Hot Dry Rock ģeotermāla rezervuāra analīzei. Izmantojot Laplasa integrālo transformāciju un Grīna funkciju risinājums tiek pārvērsts integrāla vienādojuma veidā plaisas virsmā, kas izslēdz vajadzību diskredizēt bezgalīgu 3D rezervuāru.

Izmantojot esošo modeli temperatūra un inducētie termiskie spriegumi var būt noteikti rezervuārā jebkura laika momentā, kas padara sistēmu ļoti efektīvu ģeotermālu rezervuāru analīžu veikšanā.

Abstract

The solution of non-linear problems in mechanics is usually a complex task. It requires much more efforts in analytical and numerical part of the solution (pure analytical solution for most problems is not possible at all). This work comprises solutions of several non-linear problems involving cracks growth and fractures.

In the first part of the work experimental procedure was elaborated in order to find delamination properties of the unidirectional and translaminar-reinforced composites. Bridging law, which can be calculated from experimental data, is found to be important material property. Simple numerical procedure, which uses previously found bridging law, is proposed in order to simulate crack growth in composite laminates.

In the second part the mathematical model for three-dimensional non-stationary analysis of Hot Dry Rock geothermal reservoirs is presented. By utilizing Laplace integral transform and Green's function the solution is reduced to integral equation over the surface of the fracture, which eliminates the need for discretizing the unbounded 3D reservoir. Using presented model temperature and thermally induced stresses can be found anywhere in the reservoir at any time, which makes this model quite efficient in geothermal reservoirs analysis.

Acknowledgments

The study and research work presented in this thesis has been carried out both at the Institute of Polymer Mechanics, University of Latvia (Riga, Latvia) and University of North Dakota (Grand Forks, ND, USA).

First of all, I would like to express my sincere gratitude to my supervisor, Professor Vitauts Tamužs for his invaluable guidance and continuous support during the research.

I would like to thank Dr. Ahmad Ghassemi for oportunity to work at University of North Dakota and for his guidance throughout the research.

I would also like to thank Mr. Vilis Skruls and Mr. Uldis Vilks for help in performing experiments, Dr. Janis Andersons for valuable discussions and all colleagues from Institute of Polymer Mechanics for their support.

The partial financial support of European Social Fond is gratefully acknowledged.

List of papers

The main part of this thesis consists of the following papers:

I. V. Tamuzs, S. Tarasovs and U. Vilks Progressive delamination and fiber bridging modeling in double cantilever beam composite specimens, *Eng. Frac. Mech.*, 2001, **68**, 513–525.

II. V. Tamuzs, S. Tarasovs and U. Vilks Delamination and fiber bridging phenomenon experimental and numerical investigation. Proc. International Conference on New Challenges in Mesomechanics, Vol. 2, Aalborg University, Denmark, August 26–30, 2002, pp. 605–611.

III. V. Tamuzs, S. Tarasovs and U. Vilks Delamination properties of translaminar-reinforced composites. *Comp. Sci. Technol.*, 2003, **63**, 1423–1431.

IV. A. Ghassemi, S. Tarasovs and A. H.-D. Cheng An integral equation solution for three-dimensional heat extraction from planar fracture in hot dry rock. *Int. J. Num. & Anal. Methods in Geomechanics.*, 2003, **27**, 989–1004.

V. A. Ghassemi, S. Tarasovs and A. H.-D. Cheng Integral equation solution of heat extraction induced thermal stress in enhanced geothermal reservoirs. *Int. J. Num. & Anal. Methods in Geomechanics.*, 2005, **29**, 829–844.

VI. A. Ghassemi, S. Tarasovs and A. H.-D. Cheng A 3-D study of the effects of thermomechanical loads on fracture slip in enhanced geothermal reservoirs, *Int. J. of Rock Mech. & Min. Sci.*, Vol. 44, 2007, pp. 1132–1148.

1 Introduction

The history of facture mechanics started from pioneering work of British engineer Alan Arnold Griffith in 1920 [1], where he addressed the problem of rupture of elastic solids using the theorem of minimum energy.

"Rupture of the soil has occurred, if the system can pass from the unbroken to the broken condition by a process involving a continuous decrease in potential energy. In order, however, to apply this extended theorem to the problem of finding the breaking loads of real soil, it is necessary to take account of the increase in potential energy, which occurs in the formation of new surfaces in the interior of such solids. It is known that, in the formation of a crack in a body composed of molecules which attract one another, work must be done against the cohesive forces of the molecules on either side of the crack. This work appears as potential energy, and if the width of the crack is greater than the very small distance called the 'radius of molecular action', the energy per unit area is a constant of the material, namely its surface tension".

Applying his theory to an infinite cracked panel he came up with the condition that the crack may extend as

$$\frac{\partial}{\partial a}\left(U_{rel}^{el} - U_{sep}\right) \geq 0 \tag{1}$$

where U_{rel}^{el} is the change of elastic strain energy due to crack and second term, U_{sep}, is the potential energy of two crack surfaces per unit thickness of the panel,

$$U_{sep} = 2a\gamma \tag{2}$$

where a is the crack length and γ is the "surface tension", having the dimension of an energy per area.

Crack propagation criteria can be rewritten in such form:

$$\frac{\partial U^{el}}{B\partial a} \geq G \tag{3}$$

where B is the thickness of plate and G is the energy release rate (amount of energy necessary to create new fracture surfaces and which is supposed to be a material constant in fracture mechanics).

Griffith's theory was based on experiments on brittle materials and did not include ductile materials in its consideration. Almost four decades later

George R. Irwin investigated how the theory would apply to small-scale yielding conditions, meaning "that a region of large plastic deformations may exist closer to the crack but does not extend away from the crack by more than a small fraction of the crack length" [2]. In order to account for crack tip plasticity, crack propagation criteria becomes

$$\frac{\partial U^{el}}{B\partial a} \geq G^{el} + G^{pl} \tag{4}$$

where G^{pl} is a plastic contribution to the energy necessary to separate body.

The other fracture parameter, called the stress intensity factor, introduced by Irwin at the same time, is widely used in linear elastic fracture mechanics (LEFM). It was shown that in case of linear elastic material stress intensity factor (K) is directly connected to Griffith's energy release rate,

$$G = \frac{K^2}{E'} \tag{5}$$

where E' is Young's modulus in plane stress or plane stress conditions. However, since stress intensity factor is a coefficient at singular term in stress solution near crack tip in case of elastic material, its usage for non-linear problems is limited to the case of small scale yielding only.

Another big step in development of fracture mechanics theory was made by Rice in 1968 with introduction of the J-integral [3]. In elasticity, J-integral equals G^{el}, and in plasticity it is an energy release rate, $J = \partial U / B\partial a$ The J-integral is defined as

$$J = \int_{\Gamma} \left(W n_x - T_i \frac{\partial u_i}{\partial x} \right) ds \tag{6}$$

where Γ is any path beginning at the lower crack face and ending at the upper crack face, W is an strain energy density, n_x is the x-component of the outward normal to Γ, $T_i = \sigma_{ij} n_j$ and u_i are the traction and displacement vector evaluated on Γ, respectively, and ds is differential arc length.

The J-integral plays an important role in non-linear fracture mechanics, since small scale yielding restriction places rather severe limitations on the applicability of linear elastic mechanics solutions to low and intermediate strength metals and other materials with high plasticity. In large scale yielding elastic-plastic solutions must be used in their place. The J-integral is used to extend fracture mechanics into the large scale yielding range.

With introduction of R-curves (resistance curves, energy release rate as a function of crack extension - $J(\Delta a)$) it was found, that R-curves reveal

significant geometry and loading dependences. J-integral gives the total amount of dissipated energy; in case of plasticity it is the energy of plastic deformations and the energy necessary for new surface formation. Local and global contributions of plastic strain energy to J could not be separated.

Phenomenological "cohesive models" describing the fracture process by a relation between surface tractions σ and crack opening δ were found very useful in numerical fracture simulations. Cohesive model approach refers to Dugdale's [4] and Barenblatt's [5] idea of introducing a "process zone" ahead of the crack tip where material degradation and separation occur. In finite element simulations special cohesive surface elements are introduced at the boundaries of solid elements along a predefined crack path. The constitutive relation of the interface elements represents the effective mechanical behavior due to the physical processes of micro-void nucleation, growth and coalescence in a ductile material. The fracture toughness in this model is represented by the area under the traction-opening law.

$$G = \int_0^{\delta_c} \sigma(\delta) \partial\delta \tag{7}$$

The cohesive models allow to separate the total dissipated work into the local work of separation in the process zone and the global plastic work in the embedding material.

The cohesive fracture model was successfully used for concrete fracture since the work by Hilleborg *et al.* (1976) [6]. The zone of material non-linearity that exists in the neighborhood of the crack tip in a concrete structure is called fracture process zone (FPZ). The FPZ is characterized as a zone of diffuse failure in which both micro- and macro-cracks exist. Microcracks are created on the surfaces of aggregates and from voids in the cement paste. Some microcracks stabilize after nucleation while others grow and eventually coalesce with other microcracks. When the coalescence of microcracks becomes sufficiently localized macrocracks are formed. In the work of Hilleborg *et al.* discrete crack is assumed with cohesive stresses σ applied on the crack surfaces near the crack tip. But contrary to the model of Dugdale for metals, the cohesive stresses are function of crack opening, which is called softening law.

Current work attempts to solve several problems in non-linear fracture mechanics: delamination of unidirectional fiber composites in presence of large scale bridging and non-stationary coupled hydro-thermal-elastic problem for Hot Dry Rock geothermal reservoirs.

2 Delamination properties of composites

The fracture process of composites laminates is often accompanied by extensive fiber crossover bridging phenomenon. In **Papers I-III** applicability of cohesive model is examined for composites.

2.1 Delamination of unidirectional composites

The resistance to interlaminar fracture is one of the most important characteristics of laminate and unidirectional composites. The most popular method of determining the iterlaminar fracture toughness in composites is the test of double cantilever beam (DCB) specimens [7].

It is well known that the crack faces in unidirectional composites with a crack propagated parallel to fibers are joined by more or less extensive fiber crossover bridging. Such bridging increases the crack growth resistance G during crack growth, which is expressed and measured by R-curves — G as a function of crack extension. More then 10 years ago [8], it was noted that the R-curves for DCB specimens, due to extensive bridging, depend not only on the material properties but also on the geometry of specimens. Various papers on the problem were published during this decade. In 1992 [9], it was noticed that the DCB specimens with a higher bending stiffness required a longer crack extension before the steady-state crack growth resistance was attained. In 1991 [10] the concept of a bridging law was introduced to characterize the R-curve for DCB specimens.

Papers I-II describe the experimental procedure for determination of bridging law. Standard DCB specimens with additional strain clip gauge located at the initial precrack tip for crack opening measurements were used. The energy release rate (G) was calculated from experimental load displacement curve and bridging law then can be computed as

$$\sigma(\delta) = \frac{\partial G}{\partial \delta^*} \tag{8}$$

where δ^* is the crack opening at the initial precrack tip.

It was shown that bridging law does not depend on specimen thickness, contrary to R-curves, and therefore can be considered as a material property. The bridging law is then used in finite element analysis as constitutive relation for interface elements definition. Numerical simulations show that bridging law obtained from experiments with specimens of one thickness only can be used to predict material resistance to delamination for laminates of other thicknesses.

2.2 Delamination of tanslaminar-reinforced composites

In order to improve delamination properties of composites laminates through-the-thickness reinforcement is used. The reinforcement acts as crack bridging, greatly improving material resistance to delamination. Glass and carbon fiber composites with volume fraction of transverse fibers equal 2-5% and produced by 3TEX company were used in experiments. In **Paper III** experiments with this materials have been performed using double cantilever beam technique and models elaborated for large scale bridging in unidirectional composites.

High performance fibrous composites usually consist of stacked layers in which the fibers can have any in-plane orientation. The main disadvantage of these composites is low resistance to interlaminar crack propagation. Interlaminar stresses generated during impacts or near the edge are often sufficient to initiate damage in the form of delamination. Several types of 3D composites have been recently developed to improve interlaminar properties: 3D woven and braided structures, orthogonal and angle stitched laminates. The orthogonal 3D woven laminate used in this work was elaborated and produced by 3TEX Inc (USA). These laminates consist of unidirectional in-plane layers oriented in 0° and 90° directions. The transversal reinforcements are yarns oriented along normal to mid-plane. These yarns bind the material and hold the in-plane fibers together. This is achieved without interweaving the in-plane fibers, and hence avoids reduction of in-plane stiffness caused by fiber waviness.

Materials with through-the-thickness fibers have much higher fracture toughness then usual layered composites, therefore specimen's arms break when loading regular DCB specimen. In order to prevent this, special side-grooved specimens with metal tabs glued to bottom and upper sides of the specimen were designed.

The elaborated methodology was used to estimate the influence of transverse fibers to fracture resistance of glass and carbon fiber composite laminates. For investigated material it is found that the fracture toughness of glass and carbon fiber composite without transverse fibers is close to known fracture toughness data for laminated composites: 0.4 0.5 kJ/m^2 for carbon and 0.2 kJ/m^2 at crack initiation and 2 kJ/m^2 at steady state propagation for glass fiber composite. The microcracking at the tip of crack in 3D woven material starts at the same G_{IC} values as matrix cracking: 0.3 - 0.6 kJ/m^2. These results show that translaminar reinforcement does not delay damage initiation. At crack opening equal to 0.2 mm, the crack propagation resistance increases up to 10 times and for steady state propagation at crack

opening 0.5 mm reaches very high values (till 20 kJ/m^2).

3 Three-dimensional analysis of Hot Dry Rock reservoir

Hot rocks and geothermal fluids in the subsurface can be an economical source of energy. The temperature in the subsurface rock can rise to 350 C at a depth of 5 km. According to [11], seventy two countries have reported direct utilization of geothermal energy (space heating, industrial use, bathing and swimming, etc.) with total installed capacity 28,268 MW$_t$. The total annual energy use is 273,372 TJ (75,943 GWh), indicating a 43% increase over 2000. Geothermal electricity is currently being generated in 24 countries with total running capacity approximately 8030 MW$_e$ and electric energy production is nearly 57,000 GWh [12].

The Hot Dry Rock (HDR) concept of geothermal energy production involves drilling two or more wells into the reservoir to intersect permeable fractures of natural or man-made origin, injecting cold water into one part of the well system, and recovering hot water from the other.

Physical and mathematical models play an important role in the planning and development of geothermal reservoirs. A number of analytical and numerical solutions exist for the prediction of heat extraction from fracture systems in geothermal reservoirs. The physical mechanisms are sometimes complicated and include mechanical, hydraulic, thermal, and chemical effects and their coupling. The geometry, however, is often simplified. Particularly, the heat conduction in the reservoir is typically modeled as one-dimensional heat flow perpendicular to the fracture surface. The primary reason for such simplification is the inefficiency in modeling an unbounded three-dimensional domain by numerical discretization.

In **Paper IV** the effect of three-dimensional heat conduction in hot dry rock is studied. The physical mechanisms considered are limited to the advective heat transport in the fracture by fluid flow and the heat exchange with the reservoir. The numerical difficulty of modeling a three dimensional, unbounded domain is overcome by utilizing the integral equation formulation and the three-dimensional Green's function of heat conduction. The need for discretizing the reservoir is entirely eliminated, and the final numerical solution system involves only the two-dimensional fracture plane, resulting in a much more efficient numerical scheme. The three-dimensional heat conduction effect is investigated against its one-dimensional simplification. It is demonstrated that the simplification of reservoir heat flow to one

dimension can significantly underestimate the extraction temperature and reservoir life.

Paper V is focused on the thermo-mechanical coupling during injection operations with time scale of months to years. Thermally induced stresses can significantly contribute to seismicity in petroleum and geothermal fields. The mechanism by which seismicity occurs is shear slip on natural fractures resulting from a reduction of normal stress across the fracture.

The magnitude of the thermal stresses associated with advective cooling has been estimated analytically [13] using an axisymmetric model of injection into a planar reservoir and a 1D heat flow in the rock mass. It has been shown that one- and two-dimensional heat flow models underestimate heat transfer to the fluid from the crack. Thus, rock cooling and the associated thermal stresses should be studied using three-dimensional heat transfer and stress models. This requires coupling a 3D heat flow model to a 3D elasticity model.

A reason for ignoring the three-dimensional nature of heat conduction in the reservoir is the difficulty in treating the infinite geothermal reservoir geometry by numerical discretization. However, using 3D Green's function for heat conduction in an integral equation formulation, the need for discretizing the 3D reservoir is eliminated.

In this paper a technique for evaluating the thermal stresses induced by water injection into enhanced geothermal reservoirs is presented. Key to this technique is that Green's function is used to model the three-dimensional infinite space such that the numerical discretization is needed only on the planar fracture surface. The technique is first applied to the solution of water injection into a infinite fracture for the comparison with a semianalytical solution. It is next applied to an injection/extraction problem in an arbitrarily shaped fracture.

In **Paper VI** a 3D heat extraction/thermal stress model is coupled with a 3D elastic displacement discontinuity method to investigate the fracture opening and slip in response to fluid pressure and cooling of the rock under a given in-situ stress field. Using this approach, the effects of each mechanism on fracture slip is estimated. The closed part of the fracture is modeled using a rigid perfectly plastic Mohr-Coulomb element. The standard Coulomb friction model assumes that no relative motion occurs if the equivalent shear stress is less than the critical stress. Iterative procedure is used to solve elastic problem with friction. The results indicate that under the conditions of the numerical experiments, a substantial increase in fracture slip is observed when thermal stresses are taken into account.

Mathematical model developed for analysis of Hot Dry Rock reservoirs in

Papers IV-VI includes system of non-stationary hydro-thermo-mechanical equations. Solution of this complex set of equations involves:

a) Laplace integral transform is used to eliminate time variable. At the end obtained solution is transformed back into time domain using approximate Laplace inversion method. The Stehfest method is adopted for this purpose.

b) The fluid flow in facture is laminar and governed by lubrication flow equation. For circular fracture fluid flow can be found analytically using method of images, for fracture of general shape finite element procedure is used to solve flow equation. The flow singularities at the wells locations were treated using singularity extraction and superposition procedure.

c) The heat energy transport by diffusion (in rock mass) and advection (in fracture) was solved using integral equation. By means of Green's function the three-dimensional diffusion equation is reduced to a two-dimensional integral equation, where integral is taken over the fracture surface only.

d) The temperature solution from previous step is then used to calculate thermally induced stresses anywhere in the reservoir.

e) 3D displacement discontinuity method is used to solve elastic problem of fracture opening and slip due to injected fluid pressure and thermally induced stresses.

This mathematical model was implemented in a computer program for the solution of temperature and stresses in cold-water injection into hot fracture problem. Program has a user-friendly graphical interface (Figure 1.) to set up the properties of reservoir and for solution visualization. The three-dimensional plot of inclined fracture with one injection well and two production wells is presented in Figure 2.

4 Conclusions

Experimental procedure has been developed for determination of unidirectional composite intralaminar fracture toughness. This procedure allows not only measure R-curves, which are dependent on the specimens geometry, but also it is possible to calculate bridging law. It was demonstrated, that bridging law is characterictics of material and therefore can be used to predict

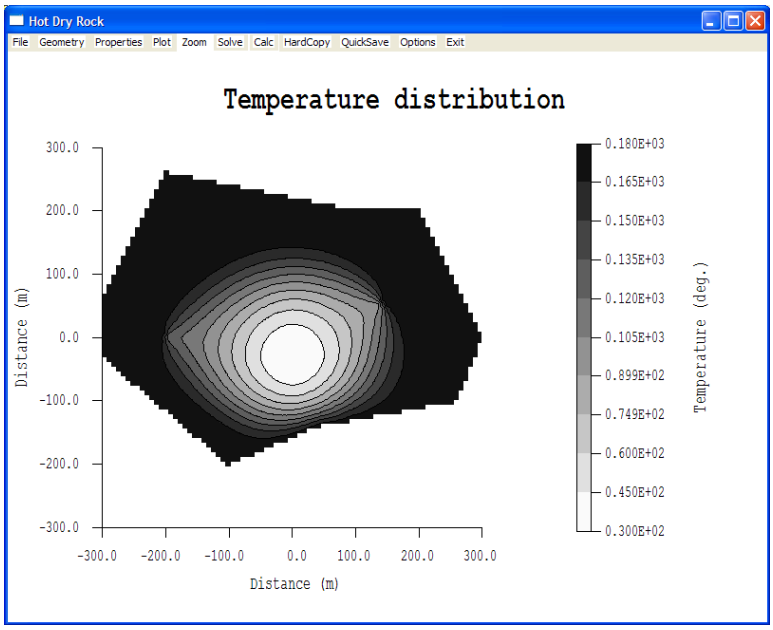

Figure 1: Screenshot of the program (temperature distribution in fracture).

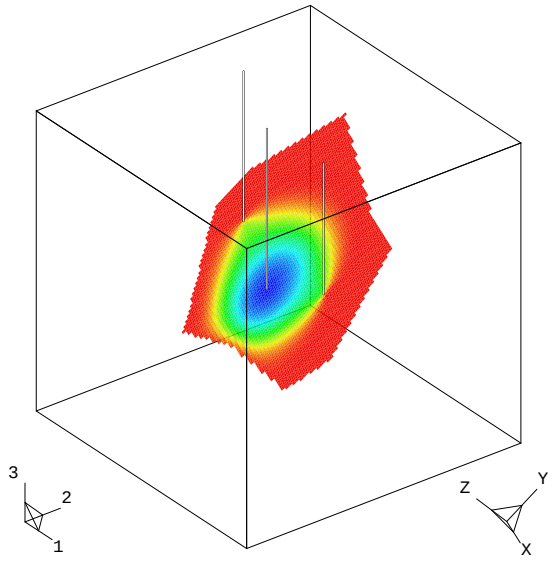

Figure 2: Inclined fracture with one injection well and two production wells.

fracture propagation in other situations. Simple numerical procedure has been used to simulate crack propagation in unidirectional composites, using experimentally calculated bridging law.

Similar methodology can be applied to tanslaminar-reinforced composites. The additional parameter crack opening displacement at the initial precrack tip (ICOD) was measured to obtain the bridging law, which is independent on the geometry of specimen. It is recommended to use the graphs G_{IC} vs. ICOD, instead of traditional R-curves (G_{IC} vs. Δa) for characterization of delamination fracture resistance of composite with extensive bridging.

The elaborated methodology is used to estimate the influence of transverse fibers to fracture resistance of laminate glass and carbon fiber composites. For investigated material it is found that the fracture toughness of glass and carbon fiber composite without transverse fibers is close to known fracture toughness data for laminated composites: 0.4–0.5 kJ/m^2 for carbon and 0.2 kJ/m^2 at crack initiation. The microcracking at the tip of crack in 3D woven material starts at the same G_{IC} values as matrix cracking: 0.3–0.6 kJ/m^2. Presence of transefse fibers does not delay damage initiation, but resistance to crack propagation is greatly improved for such matrials. For steady state crack propagation fracture toughness could reach value of 20 kJ/m^2 for carbon fiber composites.

A 3D boundary element model for heat extraction/thermal stress has been coupled with a 3D elastic displacement discontinuity method to investigate the fracture opening and slip in response to pressure and cooling of the rock under a given in-situ stress field. Using this approach, the effects of each mechanism on rock stress and fracture slip have been estimated. It has been found that not only tensile stresses develop due to the cooling, but also compressive stresses are generated in the range just outside the fracture or the fluid front. The results of displacement analysis indicate that under typical field conditions, a substantial increase in fracture slip is observed when thermal stresses are taken into account. The amount of slip would depend on the rock properties, in-situ stress, pressure, injection rate, and degree of cooling. This slip can be accompanied by seismicity; it would also result in redistribution of stresses in the rock mass and may induce slip and seismicity elsewhere in the reservoir.

This work can be distinguished form other analytical and numerical studies that treat the heat conduction in the geothermal reservoir as one-dimensional and perpendicular to the fracture. For the few numerical work that treats three dimensional heat flow and thermal stresses, the three dimensional infinite reservoir needs to be discretized. In comparison, the

present integral equation scheme only discretizes the planar fracture surface, which is a much reduced numerical solution system.

5 Suggestions for future work

There are several subjects that would be of interest for continued investigations, based on the results presented in this thesis. Some of them are shortly described here.

The first is to perform a systematic evaluation of the DCB method to measure fracture energies and bridging laws in composite materials. Possible sources of error such as non-linear beam behavior and specimen preparation should be investigated.

The second is to pursue further investigation of the effect of mixed-mode delamination of composite materials. New sets of experiments should be performed.

The third is to continue development of Hot Dry Rock reservoir numerical model. The basic steps could be to extend current computer code for multiple fractures interactions and to find stress intensity factors at the fracture edges to answer the question of fracture stability.

References

[1] Grifftih, A.A. The phenomena of rupture and flow in solids, *Phil. Trans. Roy. Soc.* London A211, 1920, 163–198.

[2] Irwin, G.R. Analysis of stresses and strains near the end of a crack traversing a plate, *J. Appl. Mech.*, 24, 1957, 361–364.

[3] Rice J.R. A path independent integral and the approximate analysis of strain concentrations by notches and cracks, *J. Appl. Mech*, 35, 1968, 379–386.

[4] Dugdale, D.S. Yielding of steel sheets containing slits, *J. Mech. Phys. Solids*, 8, 1960, 100–104.

[5] Barenblatt, G.I. The mathematical theory of euilibrium cracks in brittle fracture, *Advances in Applied Mechanics*, 7, 1962, 55–129.

[6] Hilleborg, A.M., Modeer, M., Petersson P.-E. Analysis of crack formation and crack growth by means of fracture mechanics and finite elements, *Cement and Concrete Research*, Vol. 6, 1976, 773–782.

[7] ASTM D 5528-94a. Standard test method for mode I interlaminar fracture toughness of unidirectional fiber-reinforced polymer matrix composites. Annual Book of ASTM Standards, American Society for Testing and Materials, Philadelphia.

[8] Zok F.W., Hom C.L.(1990) Large scale bridging in brittle matrix composites. *Acta Metall.Mater*. 38, 1895–1904.

[9] Spearing S.M. and Evans A.G. (1992) The role of fiber bridging in the delamination resistance of fiber-reinforced composites. *Acta Metall.Mater*. 40, 2191.

[10] Suo Z., Bao G. and Fan B. (1992) Delamination R-curve phenomena due to damage. *J.Mech.Phys.Solids*. 40,1.

[11] Lunda, J.W., Freeston, D.H. and Boyd, T.L Direct application of geothermal energy: 2005 Worldwide review, *Geothermics,* **34** (2005), 691–727.

[12] Bertani, R. World geothermal power generation in the period 2001–2005, *Geothermics,* **34** (2005), 651–690

[13] Mossop, A. Seismicity, subsidence and strain at the Geysers geothermal field, Ph.D.Dissertation, Stanford University, 2001.

Appendix

Paper I

Progressive delamination and fiber bridging modeling in double cantilever beam composite specimens

V. Tamuzs[1], S. Tarasovs, U. Vilks

Institute of Polymer Mechanics, 23 Aizkraukles St., Riga, LV 1006, LATVIA

Abstract

The dependence of R-curves on the geometry of double cantilever beam (DCB) specimens was investigated for a unidirectional epoxy-carbon composite. Extended bridging was observed during the crack propagation and R-curves for three different thicknesses were obtained. A simple numerical procedure was proposed for the crack propagation modeling by taking into account linear and nonlinear bridging laws. The results were compared with different approximate formulae for the energy release rate calculations and an appropriate formula was found. By measuring the deflection in two points of a DCB specimen and the applied load as a function of crack propagation, an exact bridging law for the composite investigated was found. These data and the numerical procedure proposed allowed us to predict the R-curve for any thickness of a DCB specimen.

Keywords: Unidirectional composite; R-curve; Bridging; Double cantilever beam.

[1]Corresponding author: Tel.: +371-2525705; fax: +371-7820467, e-mail - tamuzs@pmi.lv

1 Introduction

The resistance to delamination is one of the most important characteristics of laminate and unidirectional composites. The most popular method of determining the delamination toughness in composites is the test of double cantilever beam (DCB) specimens [1].

It is well known that the crack faces in unidirectional composites with a crack propagated parallel to fibers are joined by more or less extensive fiber crossover bridging. Such bridging increases the crack growth resistance G during crack growth, which is expressed and measured by R-curves – G as a function of crack extension. As long as 10 years ago [2], it was noted that the R-curves for DCB specimens, due to extensive bridging, depend not only on the material properties but also on the geometry of specimens. Various papers on the problem were published during this decade. In 1992 [3], it was noticed that the DCB specimens with a higher bending stiffness required a longer crack extension before the steady-state crack growth resistance was attained. In [4] (1991), the concept of a bridging law was introduced to characterize the R-curve for DCB specimens.

Among the last papers on the subject, the publications [5] should be mentioned, where the DCB specimens with different geometries loaded by pure bending moments were investigated. An appropriate bridging law was found by measuring the crack opening at the beginning of the bridging zone.

In the present paper, we investigate the peculiarities of R-curves obtained on traditional DCB specimens loaded by wedge forces, the influence of specimen geometry on R-curves and propose a scheme of measurements and calculations to predict the resistance of crack propagation in specimens of different thicknesses.

2 Energy release rate in double cantilever beam specimens

The geometry of a DCB specimen is shown in Fig. 1, where h is the thickness of the specimen, which was varied, a_0 is an initial notch, a is the length of a propagated crack, d is the crack opening under the applied wedge forces P, and δ^* is the crack opening at the tip of the initial notch. The description of the loading and measurement method is given later, in the experimental part.

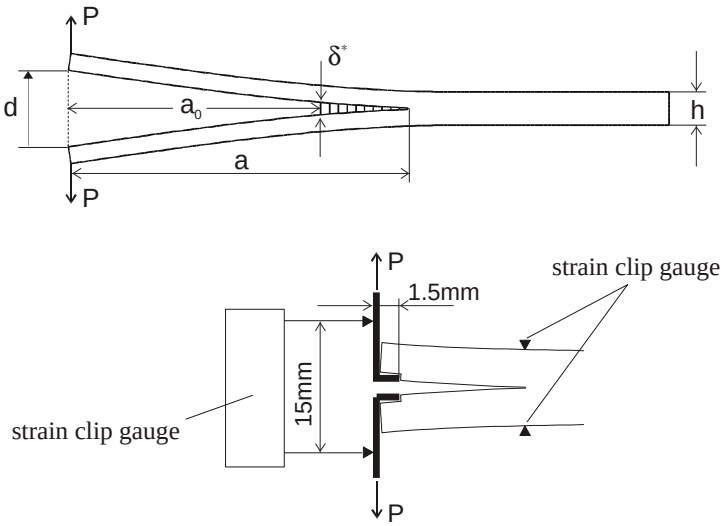

Figure 1: The specimen geometry and loading scheme and parameters measured.

The energy release rate in a DCB specimen is defined in a usual way:

$$G = -\frac{\partial \Pi}{b \partial a}, \tag{1}$$

where b is the width of a specimen, a is the crack length, Π is the potential energy accumulated in the system, and P is the force by which both sides of the specimen are loaded. The potential energy of a linearly elastic system is equal to

$$\Pi = \frac{1}{2} \int_v \sigma_{ij} \epsilon_{ij} dv - \int_0^u P(u) du, \tag{2}$$

where σ_{ij} and ϵ_{ij} are the stress and strain, v is the volume, and $P(u)$ is the the force applied, which is a function of displacement. The first term is an energy stored in the linearly elastic body and the second one is the work produced by the applied external force. The displacement u is a full opening of the DCB specimen at the point where P is applied. The first term is also expressed through the force acting on the system,

$$\Pi = \frac{1}{2} P u - \int_0^u P(u) du \tag{3}$$

From Eqs. (1) and (3) it follows that

$$G = -\frac{1}{2b}\frac{\partial P}{\partial a}u - \frac{1}{2b}P\frac{\partial u}{\partial a} + \frac{1}{b}P\frac{\partial u}{\partial a} = \frac{1}{2b}\left(P\frac{\partial u}{\partial a} - u\frac{\partial P}{\partial a}\right)$$

or

$$G = \frac{P^2}{2b}\frac{\partial c}{\partial a} \tag{4}$$

where $c = u/P$ is the compliance of the system. The formula (4) is well-known and widely used. Note that no assumptions about the type of the crack tip structure was made, therefore the formula (4) is general and should be valid for any bridging law and specimen shape. But the G values obtained can be functions of the specimen shape, not only of the characteristics of the material. G depends on the compliance $c = u/P$, which is measured experimentally or calculated theoretically by using some bridging law.

Neglecting the bridging effect, the deflection of an ideal cantilever beam, with length a and bending stiffness $EI = Ebh^3/12$, under a load P is equal to $a^3P/3EI$. The full opening of the DCB equals the doubled deflection,

$$d = \frac{2a^3P}{3EI} \tag{5}$$

and the compliance is

$$c = \frac{2a^3}{3EI} \tag{6}$$

Using Eqs. (4) and (6), the most popular formula for the DCB is obtained:

$$G(P,a) = \frac{P^2a^2}{EIb} \tag{7}$$

Combining Eqs. (7) and (5), we get three another modified formulae for G

$$G(P,a,d) = \frac{3Pd}{2ba} \tag{8}$$

$$G(P,d) = \frac{P^2}{EIb}\left(\frac{3EId}{2P}\right)^{2/3} \tag{9}$$

$$G(a,d) = \frac{9EId^2}{4ba^4} \tag{10}$$

Applying Eqs. (7) – (10) to an ideal isotropic cantilever beam, equal results will be obtained. But, strictly speaking, they are all invalid for DCB specimens since boundary conditions at the end of cracked part of specimen are not the same as at the clamped end of cantilever beam. As

result, the deflection of real specimen for given load and crack extension always will be greater, then it is predicted by beam theory (Eqn. (5)). The deflection is even higher for unidirectional composites, since in Eqn. (5) we neglect the interlaminar shear. The error is very big for short crack and diminishes when the crack propagates. Therefore, formulas (7) – (10) will give different results and it is expedient to compare the predictions obtained by Eqs. (7) – (10) and by general formula (4). For this aim the finite element model of DCB specimen without and with bridging was used. Comparing G calculated directly from finite element analyses with formulas (7) – (10), we can conclude, that formula (9) performs better even for very short cracks. Very rough explanation of this fact could be following: we exclude crack length form formula (7) and, in result, the formula (9) is written in term of compliance, as it was before derivation (Eqn. (4)). The results of finite element simulation of specimen with bridging will be presented in next section.

3 Experimental

The specimens investigated were produced from the commercialy available "Sika Carbo Dur S" epoxy/carbon sheets of thickness 1.3 mm. The initial crack was precut by a diamond saw of thickness 0.1 mm. The crack tip was sharpened by a thin blade to extend the initial crack to 25 mm. The width of the cracked specimen was $b = 11.1$ mm. Then the strips of the same material and the same width were glued on both sides of the precracked strip to produce specimens of different total thicknesses, namely 3.93, 6.56 and 9.15 mm corresponding to 3, 5, and 7 layers. The fibers were oriented along the specimen. The length of a specimen was 80 mm for 3- and 5- layer samples, and 200 mm for 7- layer ones.

The material is characterized by the following elastic constants: modulus in the fiber direction $E_1 = 155$ GPa, transverse modulus $E_2 = E_3 = 9$ GPa, shear modulus $G_{12} = 5$ GPa and Poisson ratio $\nu = 0.28$.

The specimens were loaded by a wedge load under displacement control with a constant speed of 1 mm/min. Six specimens of thicknesses 3.93 mm and 6.56 mm and three of thickness 9.15 mm were tested.

The load value was registered by the dynamometer of a MTS testing device, but the crack opening d at the edge of specimens was measured by a strain clip gauge as shown in Fig. 1. When testing the thick (9.15 mm) specimens, the crack opening δ^* at the precrack tip was also measured by second strain clip gauge attached to the top and bottom sides of the

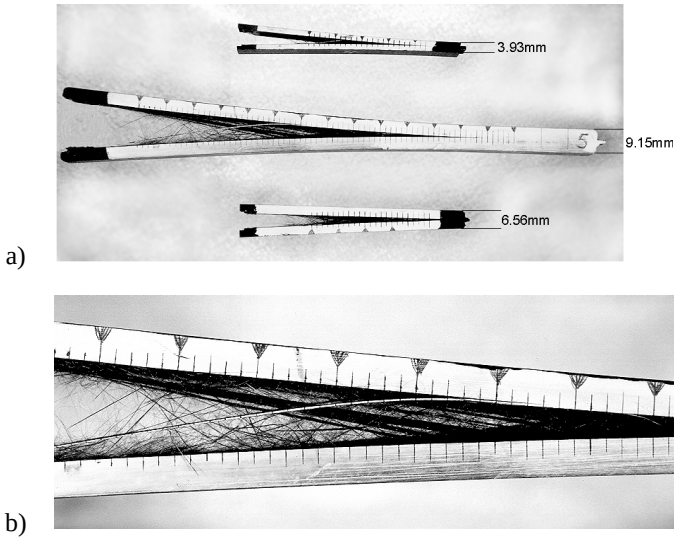

Figure 2: (a) Specimens of three different thicknesses after testing. (b) Enlarged bridging zone of a 7- layer specimen.

specimen. The accuracy of load and deflection measurements was 1%. The crack propagation was measured visualy. For this aim, the lateral sides of specimens were painted white with marks drawn in two millimeter intervals. So, the values of P, d, and δ were measured and stored for each crack increment Δa equal to 2mm. Extensive bridging was observed during the crack propagation. The specimens with extended and opened cracks are displayed in Fig. 2a, b.

The measured load-displacement curves for all specimens tested are shown in Fig. 3a, b, c. Each point on the curves corresponds to a crack increment $\Delta a = 2$ mm. These curves are used later for constructing R-curves $G(a)$.

4 Numerical simulation by FEM

In this section, we will describe a numerical procedure for the simulation of crack propagation taking into account fiber bridging. The procedure is based on the finite element method with nonlinear "interface elements" embedded along a potential delamination line, Fig. 4. The crack propagation is then modeled by introducing an appropriate stress-displacement relationship for the interface elements.

To model adequate the effect of fiber bridging, we will separate the total energy dissipation in a sample into two specific terms associated with the crack tip propagation and with fiber bridging, respectively. We need, therefore, to choose an appropriate stress-displacement relationship for the interface elements, Fig. 5, where σ is the traction across the element and δ is the opening of crack faces. This paper will concentrate on the Mode I fracture only, therefore, the stresses and displacements are both normal to the crack face.

The $\sigma(\delta)$ curve, Fig. 5, comprises three parts corresponding to the displacement intervals $(0, \delta_0)$, (δ_0, δ_1), and (δ_1, δ_2). The first and second part is responsible for the crack initiation and crack tip propagation. When the stress ahead of the crack tip reaches σ_t (the tensile strength of the material), the distance between the elements (interface thickness) is equal to δ_0, and the crack starts to propagate. Behind the crack tip, the stress decrease, and the distance between the crack faces increases up to δ_1. This region is called the "fracture process zone" (Fig. 6). The numerical tests have shown that the precise value of δ_0 has little effect on the solution, provided that δ_0 is sufficiently small to simulate an initially very stiff interface. The crack opening δ_1 depends on the initial critical fracture energy G_{0c}, which is supposed to be a characteristic of the material. So, the crack opening is

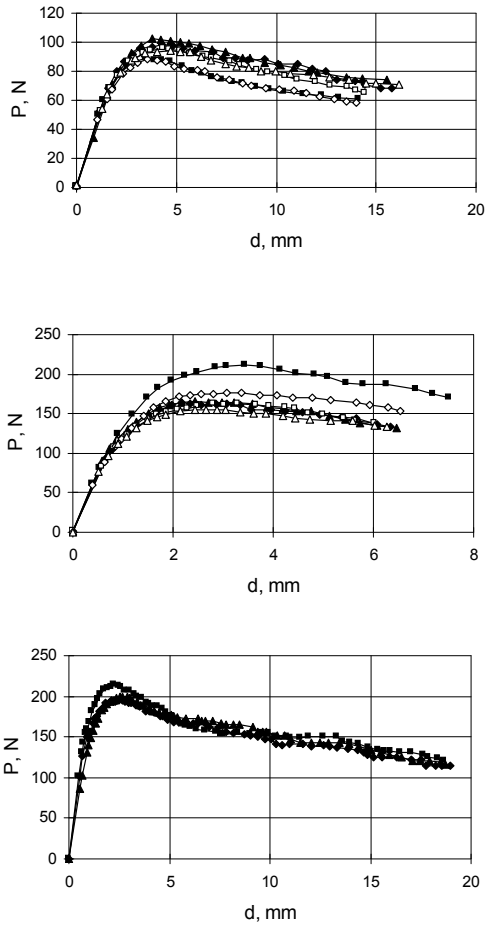

Figure 3: Experimental load-displacement curves: (a) $h = 3.93$, (b) $h = 6.55$, and (c) $h = 9.15$ mm.

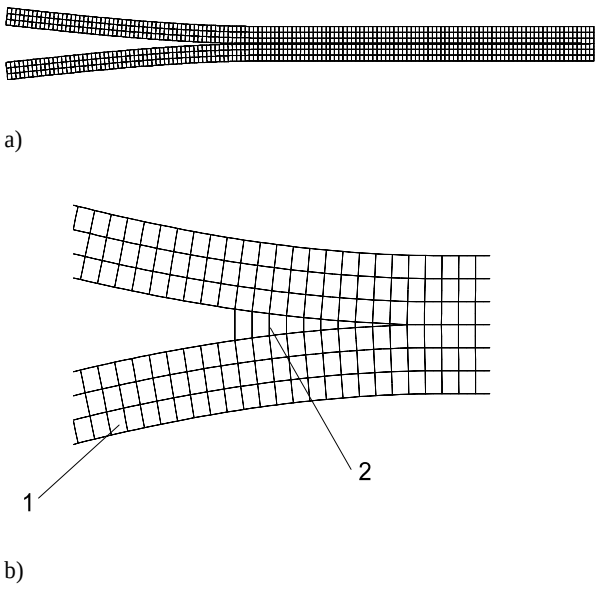

Figure 4: (a) The finite element mesh with interface elements inserted along the delamination path. (b) An enlarged area of the crack tip with a bridging zone: (1) normal finite elements; (2) open interfacial elements with a user-defined stress-displacement relationship.

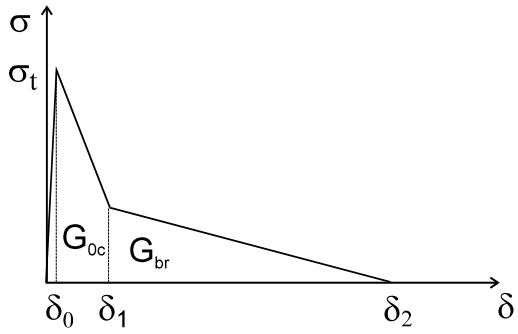

Figure 5: Stress-displacement relationship for interfacial elements.

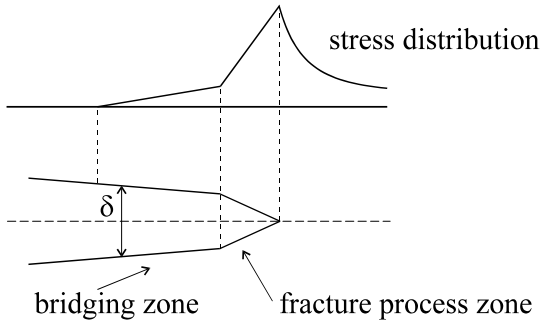

Figure 6: Stress distribution near the crack tip.

chosen such that the area under the curve to the point δ_1 is equal to G_{0c}. In practice, δ_0 is very small and $\delta_1 = 2G_{0c}/\sigma_t$.

The third part of the stress-displacement relationship (interval from δ_1 to δ_2) depends on the bridging law, which is initialy unknown, and the area under the curve represents the energy dissipation due to bridging, G_{br}.

Fig. 6 shows the stresses distributions ahead of the crack tip, in the fracture process zone and in the bridging zone. Ahead of the crack tip, we have a singular stress field. At the crack tip, the normal stress component is equal to the tensile strength of the material. Behind the crack tip, we have the fracture process zone, which should be quite small in real material, but, in the finite element analysis, its size depends on the size of elements in the model. As pointed out in Ref. [7], for good results, a fine mesh must be used. It was found there that the mesh must be fine enough to include at least two interface elements in the "fracture process zone" at the crack tip. As the crack opens, the stress level decreases being equal to zero at the end of the bridging zone. The finite element code FRANC2DL was used in this work.

Since, for the materials with extensive bridging, the energy release rate during steady state crack propagation, G_{ss}, is up to ten times higher then at the crack initiation, G_c, δ_2 will be many times greater then δ_1. A typical its value for carbon-fiber reinforced plastics is several millimeters. If the actual bridging law for a material is known, it must be utilized when defining the properties of the interface elements.

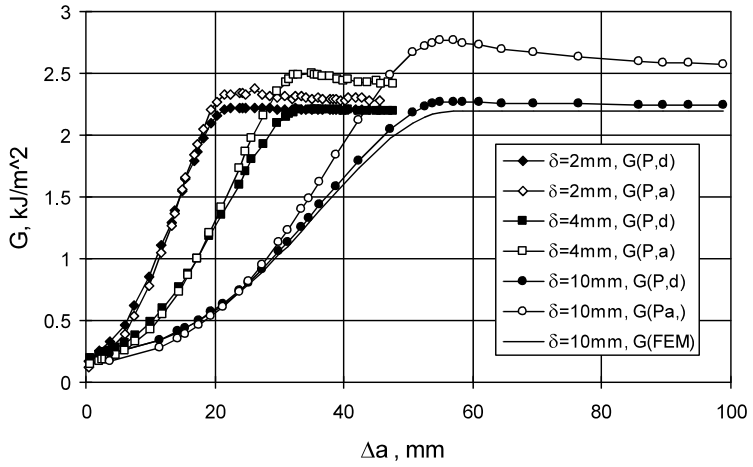

Figure 7: A comparison of the calculated energy release rates G for different linear bridging lengths and different approximated formulae and FEM.

5 Calculation of an R-curve with a linear bridging law

The energy release rate G as a function of crack propagation (R-curve) can be calculated using the above-discussed modified FEM taking into account the bridging stress-displacement relationship $\sigma(\delta)$. It is possible to get directly the value of G by calculating the J-integral along the contour around the crack tip and the bridging zone.

Another possibility consists in calculating the applied load $P(d)$ and crack opening $d(a)$ as functions of the crack length a, after which the energy release rate is obtained from Eq. (4) or Eqs. (7) – (10). A comparison of the results obtained will reveal the degree of accuracy of Eqs. (7) – (10), which, strictly speaking, are invalid for any bridging law.

The calculations were performed at $G_{0c} = 0.2$ kJ/m^2 and $G_{ss} = 2.2$ kJ/m^2, but the length of the bridging zone was varied from 2 to 10 mm. Two formulae were used for G calculation namely Eq. (7) for $G(P, a)$ and Eq. (9) for $G(P, d)$. The results obtained were compared with those, calculated by the J-integral using the FEM and are shown in Fig. 7. It is seen that the difference between Eqs. (7) and (9) increases as the length of the bridging zone increases. For extended bridging zones, the formula (7) leads to the so

called "overshoot" of G above the asymptotic value of G_{ss}. In contrary, Eq. (9) gives a good agreement with the directly calculated values of G even for the largest bridging length.

Thus, we conclude, that Eq. (9) gives a good approximation for G, and therefore we used it for calculating G from the experimentaly measured $P(a)$ and $d(a)$ (Fig. 3a–c).

The results are shown in Fig. 8a–c. It is seen that the shape of R-curves depend on the thickness of specimens, while the G_{0c} and the asymptotic value of G_{ss}, within the accuracy of the data scatter, are independent of the geometry. The crack length at which G_{ss} is achieved depends on the specimen thickness, as predicted by Spearing and Evans [3], – it increases with the thickness of specimens. We note that the specimen length $L = 80$ at $h = 6.56$ mm was unsufficient to reach the asymptotic value of G_{ss}.

In Fig. 9, an attempt to simulate the experimentally obtained R-curves by a linear bridging law is made. The thin lines are the experimental ones for $h = 3.93$ mm (these are the same as in Figs. 3a and 8a), which are compared with the best possible prediction for two linear bridging laws. It can be noted that the linear bridging law simulates the real crack propagation poorly.

6 A nonlinear bridging law

Calculating the J-integral (Rice 1968 [8]) around the crack tip and along the crack faces with a bridging zone, the following result for the energy release rate is obtained:

$$G = J = \int\limits_S w(\epsilon_{ij})dy - \int\limits_S P_i \frac{\partial u_i}{\partial x} dS = 2\int\limits_a^{a_0} \sigma(x)\frac{\partial u_y}{\partial x}dx + G_0 = \int\limits_0^{\delta^*} \sigma(\delta)d\delta + G_0 \tag{11}$$

from which it follows [9,10] that

$$\sigma(\delta) = \frac{\partial G}{\partial \delta^*} \tag{12}$$

And the problem is solved as follows. For a specimen having a thickness h, the dependences $P(a)$, $d(a)$ and $\delta^*(a)$ are measured, where δ^* is the crack opening at the point where the tip of the initial precrack has been located.

Then, the R-curve $G(a)$ is calculated from Eq. (9) and the experimental data $P(a)$ and $d(a)$ for the investigated specimen. With $G(a)$ and $\delta^*(a)$ known, the bridging law $\sigma(\delta)$ is obtained from Eq. (12). Applying the bridging law obtained as a characteristic of the interface element in FEM

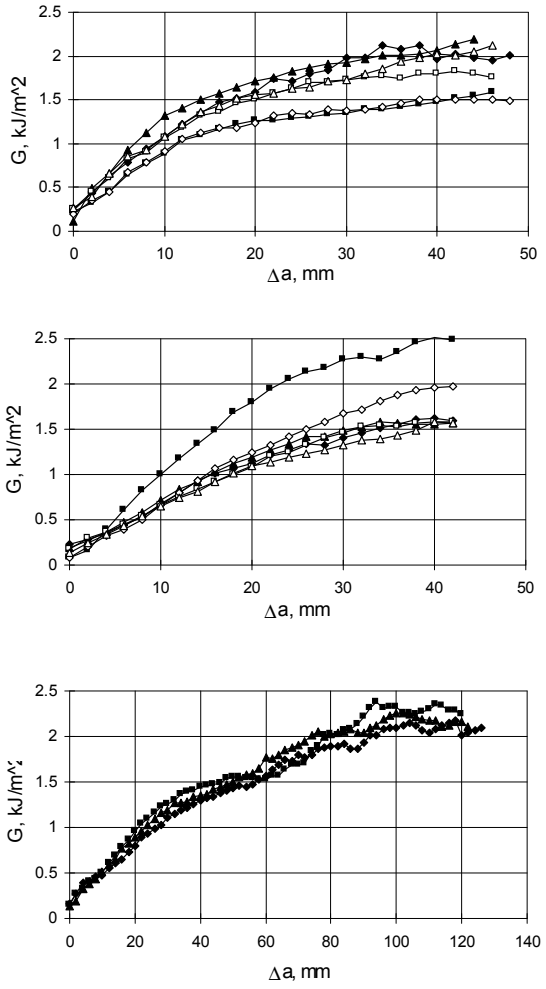

Figure 8: Experimental R-curves as functions of the specimen thickness. (a) $h = 3.93$, (b) $h = 6.55$ and (c) $h = 9.15$ mm.

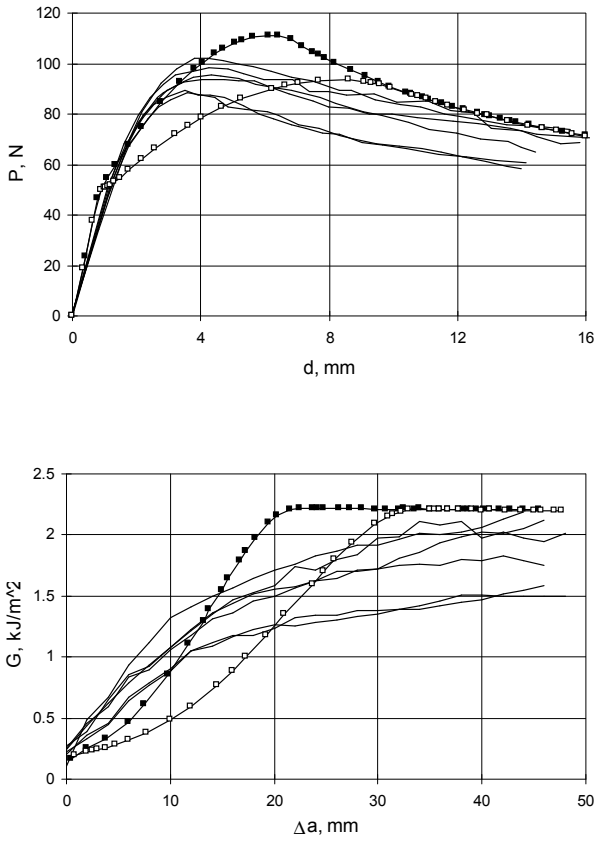

Figure 9: Description of the R-curve by a linear bridging law: (a) experimental and predicted load-displacement curves. (b) experimental and predicted R-curves. The curves ■-■-■ correspond to the bridging vanishing at $\delta_2 = 2$ mm, ⊡-⊡-⊡ - the same at $\delta_2 = 4$ mm.

the load-displacement curve $P(d)$ and R-curve $G(a)$ are predicted for any thickness of the DCB specimen.

7 Comparison with the experimental data

In Fig. 10a the experimental dependence $G(\delta^*)$ is plotted for a 9.15 mm thick specimen. In Fig. 10b, the bridging law $\sigma(\delta)$ obtained is shown using the averaged data from Fig. 10a and Eq. (12). It is seen that the bridging law is highly nonlinear and similar to that obtained by Sorensen and Jacobsen [5].

Using this law as a characteristic of the interface elements in FEM, the load-displacement curves and R-curves are calculated for all investigated specimens. The results are summarized in Fig. 11a and b, and a sufficiently good agreement with the experimental data for all specimen geometries is observed.

8 Conclusions

1. The results obtained confirm that the initial energy release rate G_{0c} and the steady-state value G_{ss} are material characteristics even at extended bridging between the delamination crack faces, whereas the shape of R-curves depend on the specimen geometry.
2. The simultaneous measurements of the wedge load, crack opening under the load, and crack opening at the tip of the initial precrack are necessary for determining the bridging law and predicting R-curves for different geometries of DCB specimens.
3. The linear bridging law doesn't allow one to predict the behavior of R-curves.
4. The use of the simple energy release rate formula $G(a, P)$ (7) which is valid for an ideal cantilever beam, leads to a significant error in the case of bridging and can lead to an apparent "overshoot" of the R-curve. In the contrary the formula $G(d, P)$ (9) reveals a rather sufficient agreement with the accurate R-curve even for extended bridging zones.
5. The numerical procedure proposed, with the interface finite elements inserted along the line of the expected crack propagation, reveals a good agreement between the numerical and experimental load-displacement curves and R-curves obtained for different DCB specimen thicknesses using the initial data from only one specimen geometry. This procedure allows one to simulate the crack growth in fiber-reinforced composites taking into account

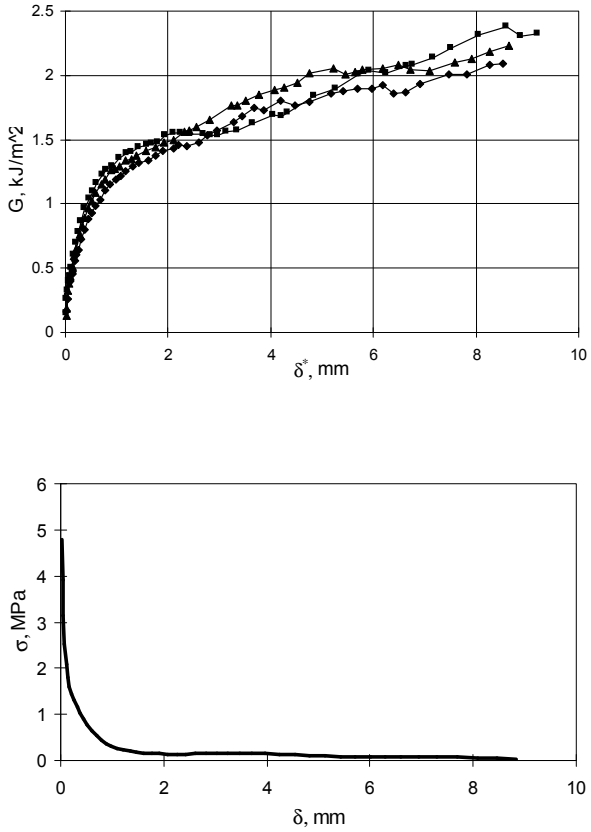

Figure 10: (a) The energy release rate G as a function of the crack opening δ^* at the tip of the initial notch, (b) the nonlinear bridging law obtained as a derivative of the averaged $G(\delta^*)$ curves.

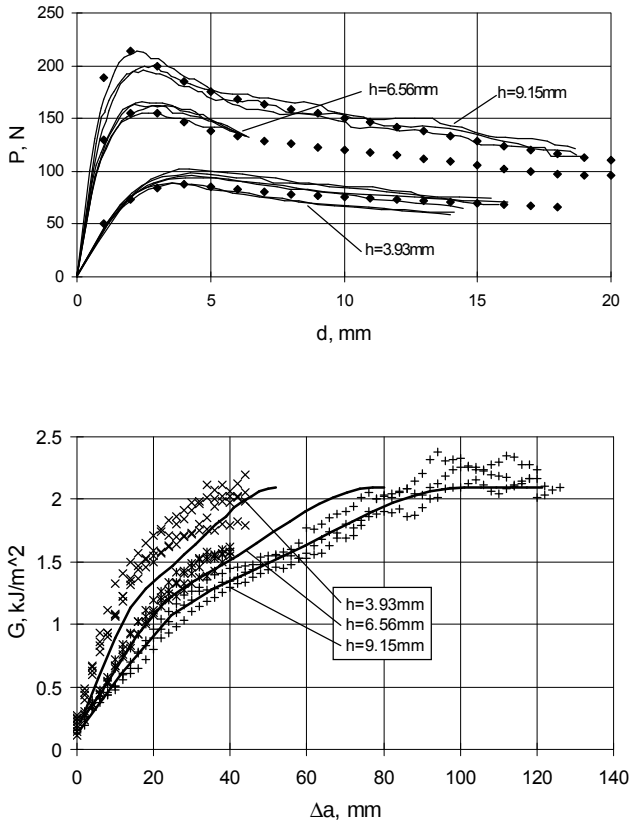

Figure 11: Comparison of the predicted and measured load-displacement and R-curves for different specimen geometries: (a) thin lines - experimental curves, dots - prediction; (b) predicted R-curves (continuous lines) and a set of experimental R-curves calculated from the data in Fig. 11a.

the fiber bridging.

6. The obtained result show, that the bridging law is a material property, at least within the accuracy of performed experiments, which allow to predict delamination process in composites with different thickness.

References

[1] ASTM D 5528-94a. Standard test method for mode I interlaminar fracture toughness of unidirectional fiber-reinforced polymer matrix composites. Annual Book of ASTM Standards, American Society for Testing and Materials, Philadelphia.

[2] Zok F.W., Hom C.L.(1990) Large scale bridging in brittle matrix composites. Acta Metall.Mater. 38, 1895–1904.

[3] Spearing S.M. and Evans A.G. (1992) The role of fiber bridging in the delamination resistance of fiber-reinforced composites. Acta Metall.Mater. 40, 2191.

[4] Suo Z., Bao G. and Fan B. (1992) Delamination R-curve phenomena due to damage. J.Mech.Phys.Solids. 40,1.

[5] Sorensen B.F., Jacobsen T.K. (1998) Large-scale bridging in composites: R-curves and bridging laws. Composites Part A, 29A, 1443–1451.

[6] Daridon L., Cochelin B. and Potier Ferry M. (1997) Delamination and Fiber Bridging Modeling in Composite Samples. Journal of Composite Materials, 31, 9, 874–888.

[7] Mi Y., Crisfield M.A., Davies A.O., Hellweg H.-B. (1998) Progressive delamination using interface elements. Journal of Composite Materials, 32, 14, 1246–1272.

[8] Rice J.R. (1968) A path independent integral and the approximate analysis of strain concentrations by notches and cracks. J. Appl. Mech., 35, 379–386.

[9] Li V.C., Chan C.M., Leung K.Y. (1987) Experimental determination of the tension-softening relations for cementitious composites. Cement and Concrete Research, 17, 441–452.

[10] Bao G., Suo Z. (1992) Remarks on crack-bridging concepts. Applied Mech. Rev., 45, 355–366.

Paper II

Delamination and fiber bridging phenomenon experimental and numerical investigation

V. Tamuzs, S. Tarasovs, U. Vilks

Institute of Polymer Mechanics, 23 Aizkraukles St., Riga, LV 1006, LATVIA

Abstract

In this work the dependence of R-curve and bridging law on the geometry of DCB specimen was investigated for a unidirectional epoxy-carbon composite. Three types of specimens, with thickness 3.93, 6.56 and 9.15 mm, were used.

In order to obtain bridging law experimentally, the crack opening at the initial crack tip position was measured. This data then have been implemented in finite element analyses. The non-linear interface elements, embedded along a potential delamination line, were used to model the crack propagation. The appropriate stress-displacement relationship for the interface elements, which can adequately model both the crack tip movement and fiber bridging creation and transport, was used.

The R-curves and bridging laws for specimens with different thickness are found experimentally and compared. The proposed finite element procedure reveals a good agreement between numerical and experimental load-displacement curves and R-curves for specimens with different thickness using the initial data from only one specimen geometry. The obtained results show, that the bridging law is a material property, at least within the accuracy of performed experiments, which allow to predict delamination process in composites with different thickness.

Keywords: unidirectional composite, bridging, double cantilever beam, R-curve.

1 Introduction

The resistance to delamination is one of the most important characteristics of laminate and unidirectional composites. One of the interesting features of crack propagation in laminates is extensive fiber bridging which often can be observed during delamination. This phenomenon can increase the fracture toughness of composites in Mode I up to ten times and therefore it is very important to know how this material property should be measured and how implement it in numerical calculations.

The most popular method of determining the interlaminar fracture toughness in composites is the test of double cantilever beam (DCB) specimens [1]. One of the standard methods to express the ability of material to increase the fracture toughness during crack propagation is so called R-curves - fracture resistance as a function of crack extension. However, as long as 10 years ago [2], it was noted that R-curves for double cantilever beam specimens, due to large scale bridging, depend not only on the material properties but also on the geometry of the specimen. Various papers on the problem were published during this decade. In 1992 [3], it was noticed that the DCB specimens with a higher bending stiffness required a longer crack extension before the steady-state crack growth resistance was attained.

The concept of a bridging law, traction on a crack faces as a function of crack opening, was introduced in 1991 [4] to characterize the crack growth resistance of a material.

Among the last papers on the subject, the publications [5] should be mentioned, where the DCB specimens with different geometries loaded by pure bending moments were investigated. An appropriate bridging law was found by measuring the crack opening at the beginning of the bridging zone.

In the present paper, we investigate the peculiarities of R-curves obtained on traditional DCB specimens loaded by wedge forces, the influence of specimen geometry on R-curves and propose a scheme of measurements and calculations to predict the resistance of crack propagation in specimens of different thicknesses.

2 Energy release rate in DCB specimens

The geometry of a DCB specimen is shown in Fig. 1, where h is the thickness of the specimen, which was varied, a_0 is an initial notch, a is the length of a propagated crack, d is the crack opening under the applied wedge forces P, and δ^* is the crack opening at the tip of the initial notch. The description

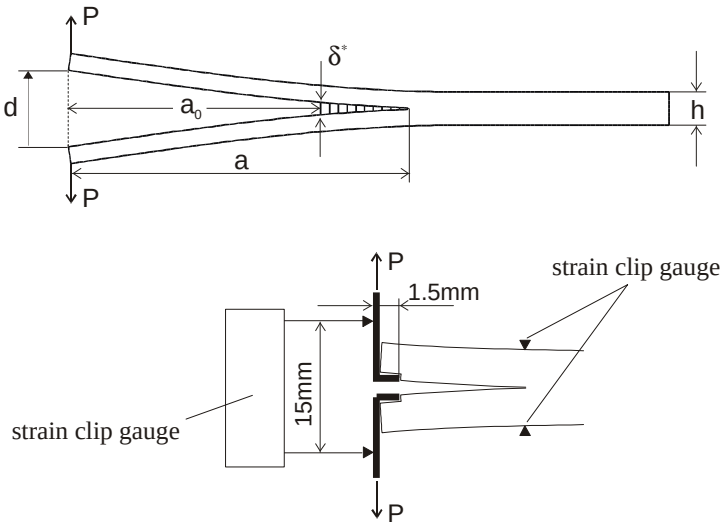

Figure 1: The specimen geometry, loading scheme and parameters measured.

of the loading and measurement method is given later, in the experimental part.

The energy release rate in a DCB specimen is defined in a usual way:

$$G = -\frac{\partial \Pi}{b \partial a} \tag{1}$$

where b is the width of a specimen, a is the crack length, Π is the potential energy accumulated in the system. For linear elastic system it can be written as:

$$G = \frac{P^2}{2b}\frac{\partial c}{\partial a} \tag{2}$$

where $c = d/P$ is the compliance of the system. The Eq. (2) is well-known and widely used. No assumptions about the type of the crack tip structure was made in this formula, therefore it should be valid for any bridging law and specimen shape. But the G values obtained can be functions of the specimen shape, not only of the characteristics of the material. G depends on the compliance $c = d/P$, which is measured experimentally or calculated theoretically by using some assumptions about bridging law [6].

Neglecting the bridging effect, the deflection of an ideal console, with length a and bending stiffness $EI = Ebh^3/12$, under a load P is equal to

$a^3P/3EI$. The full opening of the DCB equals the doubled deflection,

$$d = \frac{2a^3P}{3EI} \tag{3}$$

and the compliance is

$$c = \frac{2a^3}{3EI} \tag{4}$$

Using Eqs. (2) and (4), the most popular formula for the DCB is obtained:

$$G(P,a) = \frac{P^2a^2}{EIb} \tag{5}$$

Combining Eqs. (5) and (3), we get another modified formulae for G

$$G(P,d) = \frac{P^2}{EIb}\left(\frac{3EId}{2P}\right)^{2/3} \tag{6}$$

Applying Eqs. (5) and (6) to an ideal isotropic cantilever beam, equal results will be obtained. But, strictly speaking, they are all invalid for DCB specimens, since boundary conditions at the end of cracked part of specimen are not the same as at the clamped end of cantilever beam. As result, the deflection of real specimen for given load and crack extension always will be greater, then it is predicted by beam theory (Eq. 3). The deflection is even higher for unidirectional composites, since in Eq. (3) we neglect the interlaminar shear. The error is very big for short crack and diminishes when the crack propagates. Therefore, obtained above formulas will give different results and it is expedient to compare the predictions obtained by Eqs. (5) and (6) and by general formula (2). For this aim the finite element model of DCB specimen without and with bridging was used. Comparing G calculated directly from finite element analyses with Eqs. (5) and (6), we can conclude [7], that Eq. (6) performs better even for very short cracks and in presence of large scale bridging.

3 Experimental part

The specimens investigated were produced from the commercially available "Sika Carbo Dur S" epoxy/carbon sheets of thickness 1.3 mm. The initial crack was precut by a diamond saw of thickness 0.1 mm. The crack tip was sharpened by a thin blade to extend the initial crack to 25 mm. The width of the cracked specimen b was 11.1 mm. Then the strips of the same material and the same width were glued on both sides of the precracked

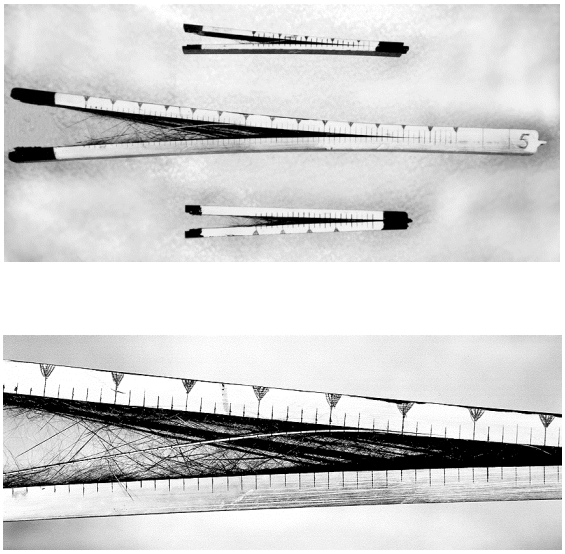

Figure 2: Specimens of three different thicknesses after testing and enlarged bridging zone of a 7-layer specimen.

strip to produce specimens of different total thicknesses, namely 3.93, 6.56 and 9.15 mm corresponding to 3, 5, and 7 layers. The fibers were oriented along the specimen. The length of a specimen was 80 mm for 3- and 5- layer samples, and 200 mm for 7- layer ones. The specimen length 80 mm was insufficient to reach the asymptotic value of energy release rate and these tests were repeated with specimen length 200 mm.

The material is characterized by the following elastic constants: modulus in the fiber direction $E_1 = 155$ GPa, transverse modulus $E_2 = E_3 = 9$ GPa, shear modulus $G_{12} = 5$ GPa and Poisson ratio $\nu = 0.28$.

The specimens were loaded by a wedge load under displacement control with a constant speed of 1 mm/min. Seven specimens of thickness 3.93 mm, eight specimens of thickness 6.56 mm and three of thickness 9.15 mm were tested.

The load value was registered by the dynamometer of a MTS testing device, but the crack opening d at the edge of specimens was measured by a strain clip gauge as shown in Fig. 1. When testing the thick (9.15 mm) specimens and long specimens from 3 and 5 layers, the crack opening δ^* at the precrack tip was also measured by second strain clip gauge attached to the top and bottom sides of the specimen. The accuracy of load and

deflection measurements was 1%. The crack propagation was measured visually. For this aim, the lateral sides of specimens were painted white with marks drawn in two millimeter intervals. So, the values of P, d, and δ were measured and stored for each crack increment Δa equal to 2 mm.

Extensive bridging was observed during the crack propagation. The specimens with extended and opened cracks are displayed in Fig. 2.

The measured load-displacement curves for all tested specimens are shown in Fig. 3. Each point on the curves corresponds to a crack increment $\Delta a = 2$ mm. These values are used later in R-curves calculations (Fig. 4). Energy release rate in all cases was calculated using Eq. (6).

4 Bridging law

Calculating the J-integral [8] around the crack tip and along the crack faces with a bridging zone, the following result for the energy release rate is obtained:

$$G = J = \int\limits_S w(\epsilon_{ij})dy - \int\limits_S P_i \frac{\partial u_i}{\partial x} dS = 2\int\limits_a^{a_0} \sigma(x)\frac{\partial u_y}{\partial x}dx + G_0 = \int\limits_0^{\delta^*} \sigma(\delta)d\delta + G_0 \tag{7}$$

from which follows [9,10] that

$$\sigma(\delta) = \frac{\partial G}{\partial \delta^*} \tag{8}$$

where $\sigma(\delta)$ is traction on a crack faces as a function of crack opening.

For a specimen having a thickness h, the dependences $P(a)$, $d(a)$ and $\delta^*(a)$ are measured, where δ^* is the crack opening at the point where the tip of the initial precrack has been located. With $G(a)$ and $\delta^*(a)$ known, the bridging law $\sigma(\delta)$ is obtained from Eq. (8) and later can be used for numerical simulation of crack propagation in DCB specimens with any thickness.

In Fig. 5a the energy release rate G as a function of the crack opening is plotted for all investigated specimens. The curves for specimens of different thickness almost coincide, taking into account typical scatter of fracture tests. Calculated bridging laws for these specimens are plotted in Fig. 5b.

5 Numerical simulation by FEM

In this section, we will describe a numerical procedure for the simulation of crack propagation taking into account fiber bridging.

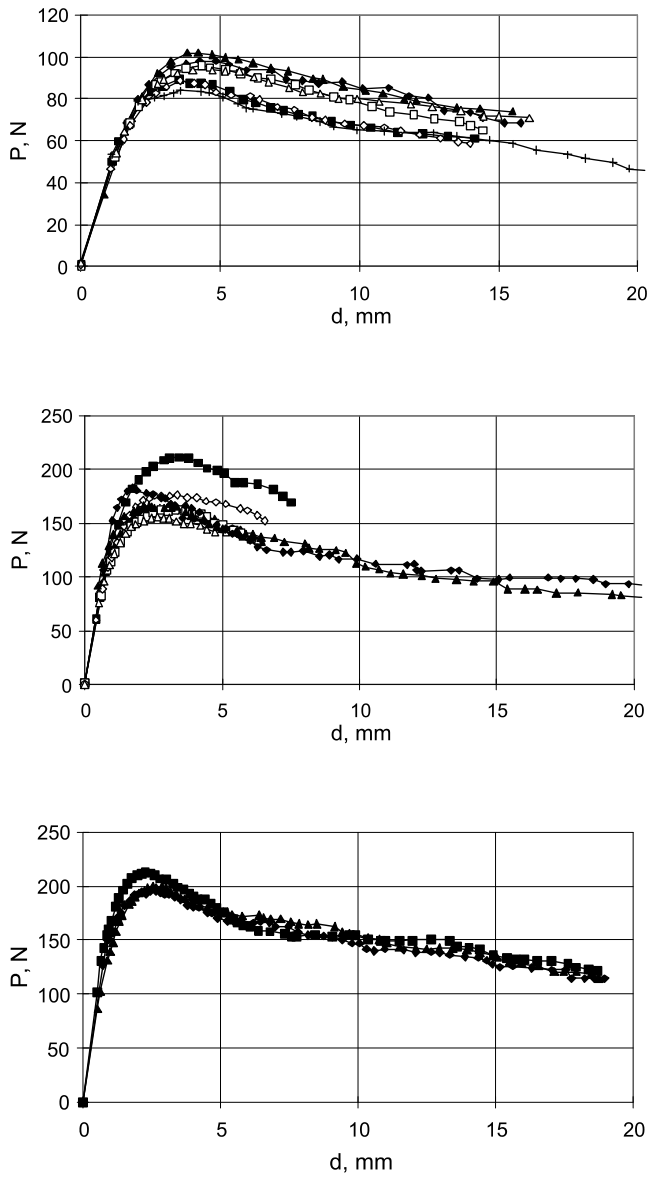

Figure 3: Experimental load-displacement curves: $h = 3.93$ mm, $h = 6.55$ mm and $h = 9.15$ mm respectively.

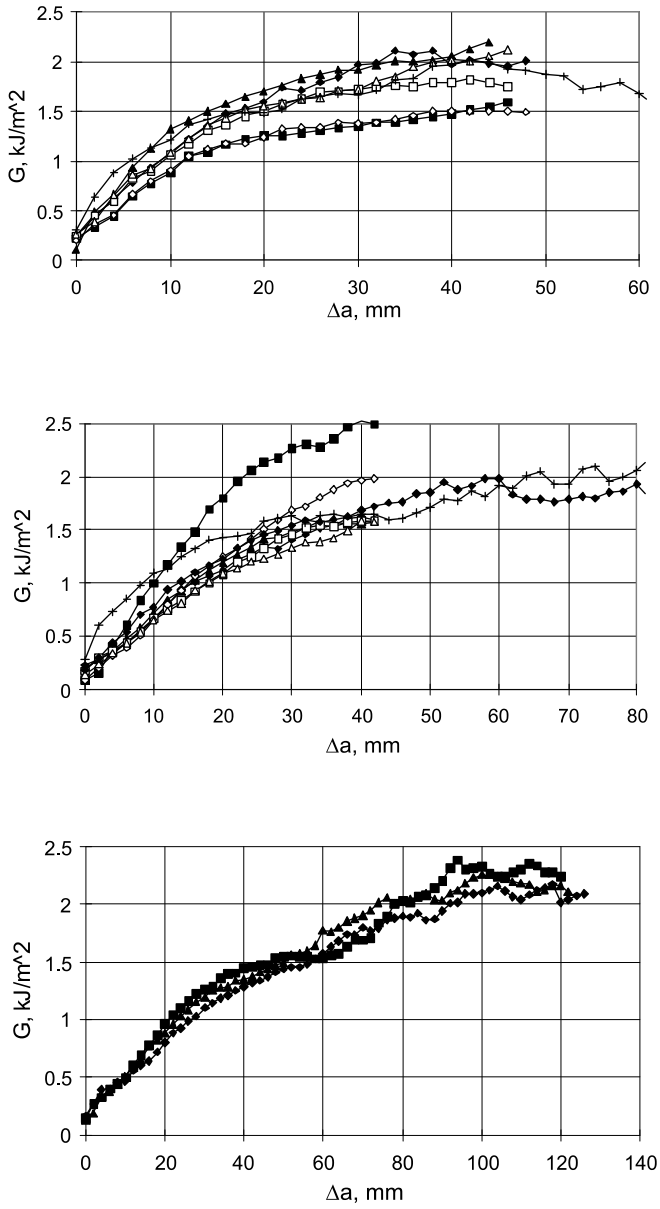

Figure 4: Experimental R-curves for specimens with different thickness: $h = 3.93$ mm, $h = 6.55$ mm and $h = 9.15$ mm respectively.

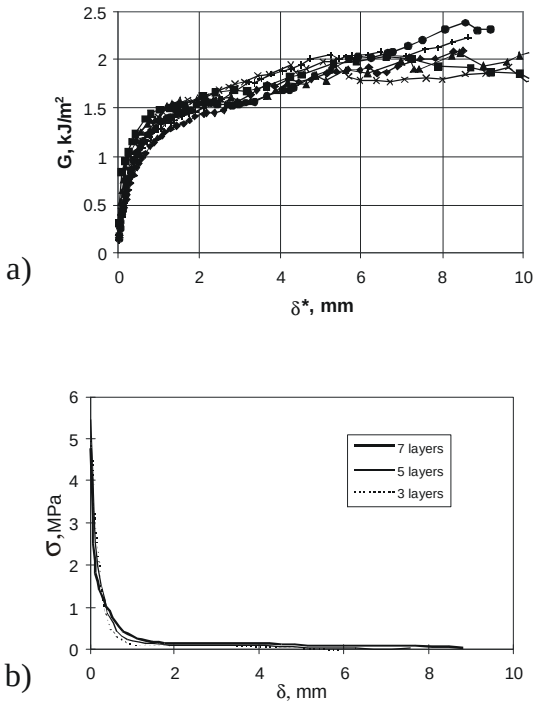

Figure 5: (a) The energy release rate G as a function of the crack opening δ^* at the tip of the initial notch, (b) the experimentally obtained bridging law.

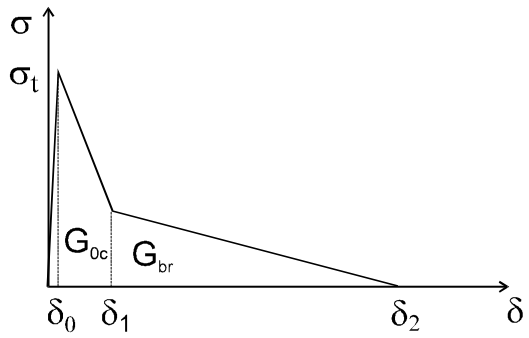

Figure 6: Stress-displacement relationship for interface elements.

The procedure is based on the finite element method with nonlinear "interface elements" embedded along a potential delamination line. The crack propagation is then modeled by introducing an appropriate stress-displacement relationship for the interface elements.

To model the effect of fiber bridging, we will separate the total energy dissipation in a sample into two specific terms associated with the crack tip propagation and with fiber bridging, respectively. We need, therefore, to choose an appropriate stress-displacement relationship for the interface elements, Fig. 6, where σ is the traction across the element and δ is the opening of crack faces. This work will concentrate on the Mode I fracture only; therefore, the stresses and displacements are both normal to the crack face.

The $\sigma(\delta)$ curve, Fig. 6, comprises three parts corresponding to the displacement intervals $(0, \delta_0)$, (δ_0, δ_1), and (δ_1, δ_2). The first and second part is responsible for the crack initiation and crack tip propagation. When the stress ahead of the crack tip reaches σ_t (the tensile strength of the material) the distance between the elements (interface thickness) is equal to δ_0, and the crack starts to propagate. Behind the crack tip, the stress decrease, and the distance between the crack faces increases up to δ_1. This region is called the "fracture process zone". The numerical tests have shown that the precise value of δ_0 has little effect on the solution, provided that δ_0 is sufficiently small to simulate an initially very stiff interface. The crack opening δ_1 depends on the initial critical fracture energy G_{0c}, which is supposed to be a characteristic of the material. So, the crack opening is chosen such that the area under the curve to the point δ_1 is equal to G_{0c}. In practice, δ_0 is very small and $\delta_1 = 2G_{0c}/\sigma_t$. The size of fracture process zone, which should be

quite small in real materials, in the finite element analysis depends on the size of elements in the model. As pointed out in [11], for good results, a sufficiently fine mesh must be used. It was found there that the mesh must be fine enough to include at least two interface elements in the "fracture process zone" at the crack tip.

The third part of the stress-displacement relationship (interval from δ_1 to δ_2) depends on the bridging law and the area under the curve represents the energy dissipation due to bridging, G_{br}. As the crack opens, the stress level decreases, being equal to zero at the end of the bridging zone.

Since, for the materials with extensive bridging, the energy release rate during steady state crack propagation, G_{ss}, is up to ten times higher then at the crack initiation, G_c, δ_2 will be many times greater then δ_1. A typical its value for carbon-fiber reinforced plastics is several millimeters. If the actual bridging law for a material is known, it must be utilized when defining the properties of the interface elements.

Using calculated in previous section bridging law of specimen with thickness 9.15 mm as a stress-displacement relationship for the interface elements in FEM, the load-displacement curves and R-curves are calculated for all specimens investigated. The results are summarized in Fig. 7, and a sufficiently good agreement with the experimental data for all specimen geometries is observed.

The finite element code FRANC2DL was used in this work.

6 Conclusions

The obtained results confirm that the initial energy release rate G_{0c} and the steady-state value G_{ss} are material characteristics even at extended bridging between the delamination crack faces, whereas the shape of R-curves depend on the specimen geometry.

The simultaneous measurements of the wedge load, crack opening under the load, and crack opening at the tip of the initial precrack are necessary for determining the bridging law and predicting R-curves for different geometries of DCB specimens.

The obtained result show that the bridging laws for specimens with different thicknesses are in good agreement with each other, at least within the accuracy of performed experiments, and can be considered as a material property. This fact allows to predict delamination process in composites with different thickness using experimental data from experiments with specimens of only one thickness.

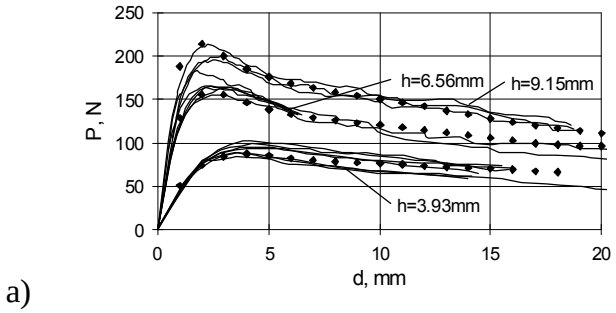

a)

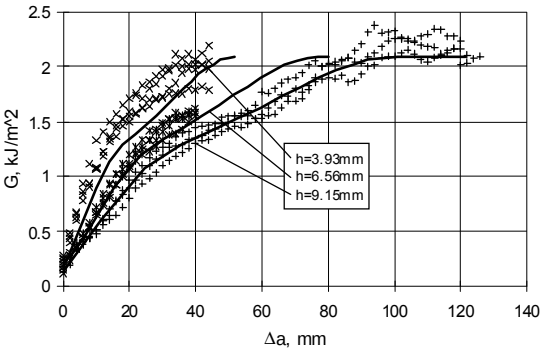

b)

Figure 7: Comparison of the predicted and measured load-displacement and R-curves for different specimen geometries: a) thin lines - experimental curves, dots - prediction; b) predicted R-curves (continuous lines) and a set of experimental R-curves.

The numerical procedure proposed, with the interface finite elements inserted along the line of the expected crack propagation, reveals a good agreement between the numerical and experimental load-displacement curves and R-curves obtained for different DCB specimen thicknesses using the initial data from only one specimen geometry. This procedure allows one to simulate the crack growth in fiber-reinforced composites taking into account the fiber bridging.

References

[1] ASTM D 5528–94a. Standard test method for mode I interlaminar fracture toughness of unidirectional fiber-reinforced polymer matrix composites. Annual Book of ASTM Standards, American Society for Testing and Materials, Philadelphia.

[2] Zok, F.W., Hom, C.L., (1990), *Acta Metall.Mater.*, 38, pp. 1895.

[3] Spearing, S.M., Evans, A.G., (1992), *Acta Metall.Mater.*, 40, No.9, pp. 2191.

[4] Suo, Z., Bao, G., Fan, B., (1992), *J.Mech.Phys.Solids.*, 40, No.1., pp. 1.

[5] Sorensen, B.F., Jacobsen, T.K., (1998), *Composites Part A*, 29A, pp. 1443.

[6] Daridon, L., Cochelin, B., Potier Ferry, M., (1997), *Journal of Composite Materials*, 31, No.9, pp. 874.

[7] Tamuzs, V., Tarasovs, S., Vilks, U., (2001), *Eng. Frac. Mech.*, 68, pp. 513.

[8] Rice, J.R., (1968), *J. Appl. Mech.*, 35, pp. 379.

[9] Li, V.C., Chan, C.M., Leung, K.Y., (1987), *Cement and Concrete Research*, 17, pp. 441.

[10] Bao, G., Suo, Z., (1992), *Applied Mech.* Rev., 45, pp. 355.

[11] Mi, Y., Crisfield, M.A., Davies, A.O., Hellweg, H.-B., (1998), *Journal of Composite Materials*, 32, No.14, pp. 1246.

Paper III

Delamination properties of translaminar-reinforced composites

V. Tamuzs[1], S. Tarasovs, U. Vilks

Institute of Polymer Mechanics, 23 Aizkraukles St., Riga, LV 1006, LATVIA

Abstract

In the paper the delamination crack propagation is investigated in 3D woven carbon and glass fiber composites. Composites were produced in 3TEX company and had volume fraction of transverse fibers equal 2-5 percents of total volume of fibers. The reinforcement acts as crack bridging, greatly improving material resistance to delamination. In this paper investigation of this material has been performed using double cantilever beam technique and models elaborated for large scale bridging in UD composites. The following alterations and novelties are introduced: 1) The appropriate form and shape of specimens with glued additional metallic tabs was elaborated allowing to avoid the premature break of specimen arms; 2) Original loading device was designed to transfer high load directly to crack faces, and additional measurement of crack opening was proposed (as in the case of UD composite) to find the bridging law; 3) The convenient analytical formula for G_{Ic} calculation was proposed and used; 4) Instead of traditional R-curve which is geometry dependent it was proposed to characterize the delamination resistance as function of crack opening displacement. The quantitative delamination characteristics for materials investigated are presented.

Keywords: 3D composites; C. Delamination; C. Fibre bridging beam.

[1]Corresponding author: Tel.: +371-2525705; fax: +371-7820467, e-mail - tamuzs@pmi.lv

1 Introduction

Delamination properties of laminated composites are very important material characteristics. Fracture toughness of regular laminated composites has rather low values (usualy the critical delamination energy release rate in mode I – G_{IC} does not exceed 0.2 – 0.4 kJ/m^2). One of the way to improve the delamination toughness consists in introducing the small amount of fibers in transverse direction of plate.

Comprehensive review in different aspects of stitched composites was published by Dickinson *et all.* [1]. In work [2] finite element analysis was used to investigate failure initiation in translaminar reinforced composites. It was found that translaminar reinforcement does not delay damage initiation, even tough it restricts damage progression.

The theoretical modelling of fracture of stitched composites was elaborated by Cox and Massaba [3], where fracture behaviour in mode II of stitched composite was analyzed. However the reliable experimental methods and fracture characteristics of stitched composites are still rather few [4] because of very high delamination resistance and corresponding difficulties of testing.

In contrast the delamination properties of regular UD and laminate composites are investigated rather well. Fore mode I the most popular method is the double cantilever beam test, for which the corresponding standard is elaborated [5]. It should be noted that even for regular (non stitched) composites the delamination usually is accompanied by bridging phenomena, resulted in the dependence of delamination resistance upon crack propagation i.e. the distinct R-curve appearance.

It was found that the crack bridging, requires new concepts and methods to be used for fracture resistance calculation [6,7]. The linear elastic fracture mechanics cannot correctly describe delamination in laminates in presence of large scale bridging. Crack growth cannot be described by a single parameter, such as fracture toughness, which is not a material constant in this case but depends on crack size, geometry of specimen and loading conditions.

One of the results of [6,7] consists in the statement that using the double cantilever beam (DCB) and an additional strain slip gauge at precrack tip it is possible to obtain from experimental data not only R-curves, but also stresses at crack faces as function of crack opening displacement in the presence of large scale bridging. This bridging law is the property of material (in contrast to R-curve, which shape depends on the stiffness of specimen). The elaborated methodology can be adapted for investigation of delamination of

3D composites with some alterations caused by significantly higher fracture toughness values. It is the actual aim of the present paper.

2 The materials and specimens investigated

High performance fibrous composites usually consist of stacked layers in which the fibers can have any in-plane orientation. The main disadvantage of these composites is low resistance to interlaminar crack propagation. Interlaminar stresses generated during impacts or near the edge are often sufficient to initiate damage in the form of delamination. Several types of 3D composites have been recently developed to improve interlaminar properties: 3D woven and braided structures, orthogonal and angle stitched laminates. The orthogonal 3D woven laminate used in this work was elaborated and produced by 3TEX Inc (USA). These laminates consists of unidirectional in-plane layers oriented in 0° and 90° directions. The transversal reinforcements are yarns oriented along normal to mid-plane. These yarns bind the material and hold the in-plane fibers together. This is achieved without interweaving the in-plane fibers, and hence avoids reduction of in-plane stiffness caused by fiber waviness. The mechanical properties of materials are described in details in [8].

Four types of composites were studied: fracture toughness of glass and carbon fiber composites with transverse fibers and two similar materials without fibers in transverse direction were tested and the increase of the fracture toughness caused by the reinforcement in transverse direction was estimated.

The specimens for measurement of the fracture toughness of material without transverse fibers were cut from the plates having initial precrack which was introduced by insert of 1 inch wide 0.05 mm thick teflon film between two 3D mats before the moulding of composite plates. So the specimens had classic DCB shape of thickness 10 mm for carbon composite and 6.1 mm for glass-fiber specimens, width equal 15 mm length 250 mm and initial precrack equal 25 mm.

The specimens for measurement of the fracture toughness of material with transverse fibers having the same size were cut from 3D woven panels having thickness 6.9 mm for glassfiber composite and 7 mm for carbon fiber composite. The width of specimen was the same – 15 mm. Initial notches having length 25 mm and opening equal to 0.3 mm for 3D glass fiber composite and 0.5 mm for 3D carbon specimens were introduced by a thin saw. The crack tip was sharpened with a thin blade.

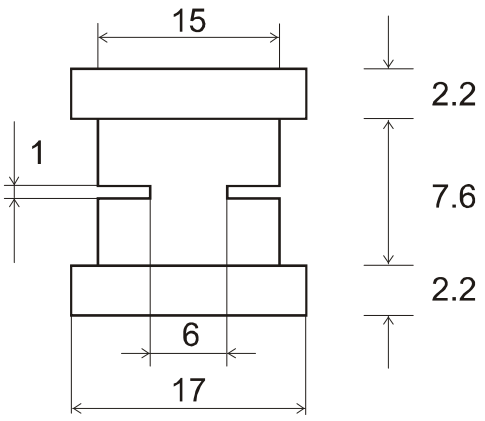

Figure 1: Cross-section of side-grooved specimen (all dimensions in plot are millimetres).

In order to monitor the position of the crack front the edges of the specimens were painted with a white brittle paint (typewriter erasing fluid) and fine lines were drawn at 2mm intervals on the white surface. The operator measured the crack length visually with a magnifying glass.

Materials with through-the-thickness fibers have much higher fracture toughness then usual layered composites, therefore specimen's arms break before the crack propagation. In order to prevent this, metal tabs were glued to bottom and upper sides of specimen. Steel tabs with thickness of 2.0, 2.2 and 2.5 mm and width 17 mm were used. The most suitable adhesive has been found to be Polyurethane power adhesive "Bison".

When testing the tabbed 3D carbon-fiber specimens, delamination of metal tabs from surface of specimen before crack initiation was observed in all initial experiments. In order to prevent tabs delamination, side-grooved specimens were used. The corresponding drawing of crossection is shown on Fig. 1.

3 Procedure of experimental loading and measurements

The MTS testing rig (model 309) with the 20 kN load cell was used. Because of rather high load level, the force was applied not through glued metallic blocks (as recommended in [5]), but by specially designed test device. By

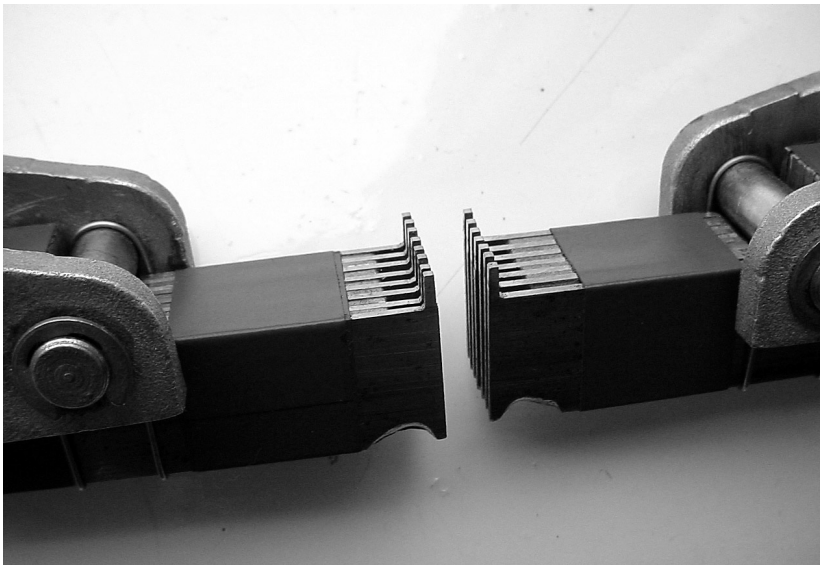

Figure 2: The loading device in separated position.

means of "comb tooth" of the device the load was applied directly to the faces of the initial precrack as wedgeforces (see Figs. 2 and 3). The loading was performed under the displacement control at a constant rate of 2 mm/min.

The geometry of a DCB specimen, where the places of attached extensometers are shown, is displayed in Fig. 4. The total thickness of the specimen is marked as $2h$, a_0 is the size of initial notch, a is the length of a propagated crack, d is the crack opening under the applied wedge forces P, and δ^* is the crack opening at the tip of the initial notch.

The picture of glass fiber 3D specimen with attached extensometers under load is shown on Fig. 5. Two extensometers, one attached to the loading device test jig for measuring of crack opening along the load line and second attached to the top and bottom sides of the specimen at the end of initial crack, were used (Fig. 4). The displacement of actuator of the testing machine was recorded too.

The load–displacement curve was monitored throughout the test and length of the crack on one side of the specimen was also noted on the load–displacement trace at regular intervals. The specimens were unloaded after crack propagation equal to 10 mm, and then loading was continued.

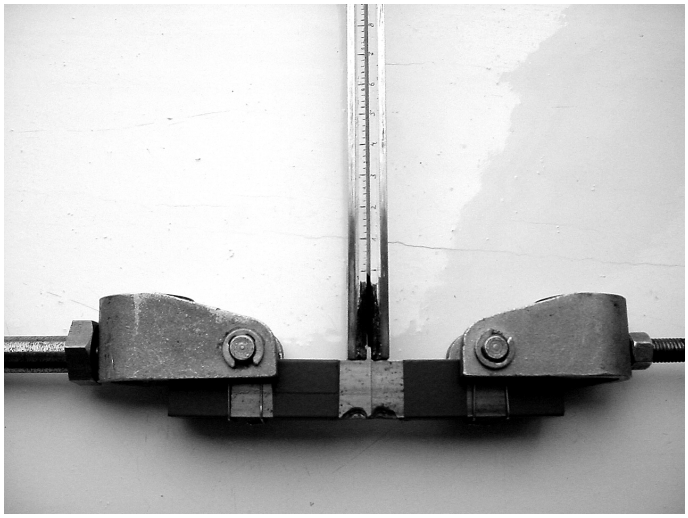

Figure 3: The specimen and loading device before testing.

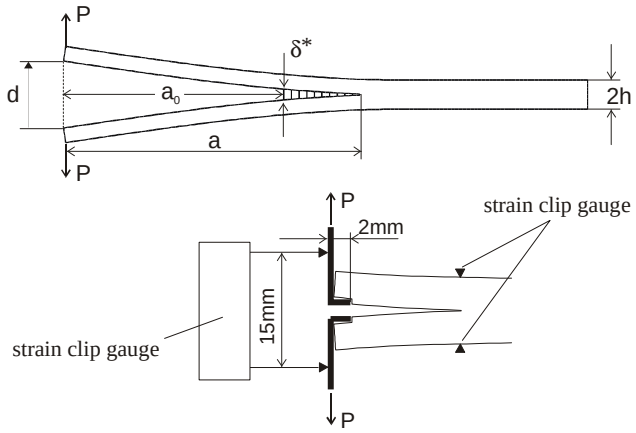

Figure 4: Geometry of the specimen and parameters measured.

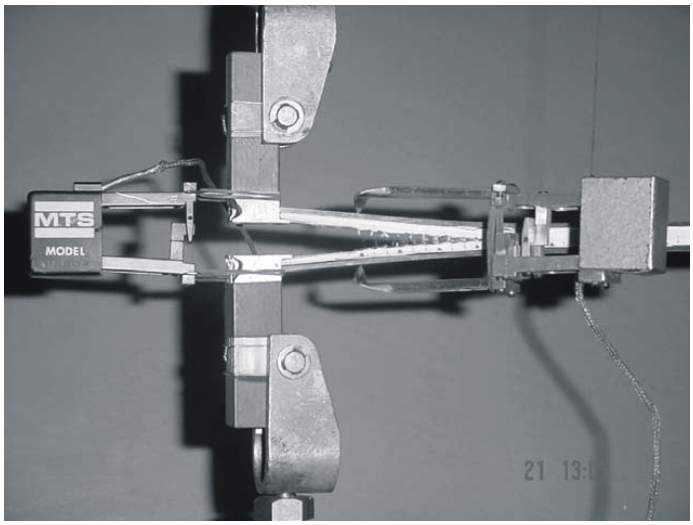

Figure 5: 3D glass-fiber specimen installed in MTS machine under load.

4 Energy release rate calculation

The energy release rate in a DCB specimen is defined in a common way:

$$G = -\frac{\partial \Pi}{b \partial a} \tag{1}$$

where $c = d/P$ is the compliance of the system. The formula (1) is well-known and widely used.

Neglecting the bridging effect, the deflection of an ideal cantilever beam, with length a, width b and bending stiffness $EI = Ebh^3/12$, under load P is equal to $a^3P/3EI$. The full opening of the DCB equals the doubled deflection,

$$d = \frac{2a^3P}{3EI} \tag{2}$$

and the compliance is

$$c = \frac{2a^3}{3EI} \tag{3}$$

Using Eqs. (1) and (3), the most popular formula for the DCB specimen is obtained:

$$G(P, a) = \frac{P^2a^2}{EIb} \tag{4}$$

Combining Eqs. (4) and (2), we get three another modified formulae for G

$$G(d,P,a) = \frac{3Pd}{2ba} \tag{5}$$

$$G(d,P) = \frac{P^2}{EIb}\left(\frac{3EId}{2P}\right)^{2/3} \tag{6}$$

$$G(a,d) = \frac{9EId^2}{4ba^4} \tag{7}$$

Applying Eqs. (4)–(7) to an ideal isotropic cantilever beam, equal results will be obtained. But, strictly speaking, they are all invalid for real DCB specimens since boundary conditions at the end of cracked part of specimen are not the same as at the clamped end of cantilever beam. In results of interlaminar shear deformation and crack tip rotation the deflection of real specimen for given load neglecting the bridging always will be greater, then it is predicted by beam theory (Eq. (2)). It is especially important for unidirectional composites, because they have low interlaminar shear modulus. The error is very big for short crack and diminishes when the crack propagates. Therefore, formulas (4)–(7) will give different results and it is expedient to compare the predictions obtained by Eqs. (4)–(7) and by general formula (1). For this aim the finite element model of DCB specimen without and with bridging was used [7]. Comparing G calculated directly from finite element analyses with formulas (4)–(7), as shown in Fig. 6, it was concluded, that formula (6) performs better even for very short cracks. In this comparative theoretical analysis the deflection d in formulas (5)–(7) is taken from finite element calculations.

Applying these formulas to experimental results the deflection is taken from experimental graphs and therefore reflects real compliance of specimen including the influence of bridging effect as well.

The ASTM standard [5] recommends to use for calculation the formula (5) – $G(d,P,a)$, which overestimates the value of G as it is seen in Fig. 6. For correction of results, it is recommended to use some fictitious crack size $a+\Delta a$, and correction Δa is determined by generating a least square plot of the cube root compliance $c^{1/3}$ as a function of crack length a. The method is called "Modified Beam Theory (MBT)" [5]. It is clear that introduction of artificially enlarged crack size will improve the results of formula (5) and (4) as well. By this method the similar accuracy to Eq. (6), where crack length is excluded and substituted by experimentally measured compliance, can be achieved. However, the method has two disadvantages. First, MBT technique assumes that $c^{1/3}$ is a linear function of crack length a, but only in

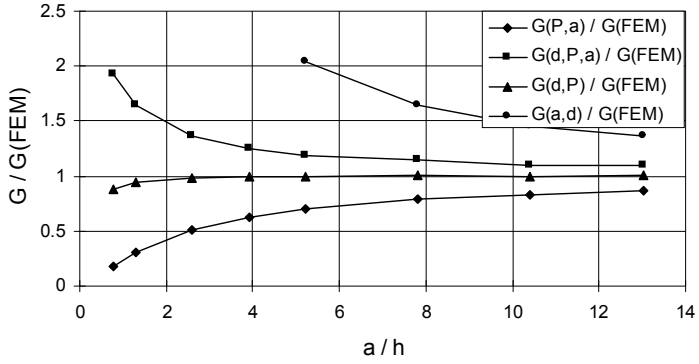

Figure 6: The comparison of energy release rate values calculated using Eq. (4)-(7) with G obtained directly from finite element model for different crack length to thickness ratio.

case when fracture toughness has a constant value during crack propagation the experimental points can be fitted by a straight line. In case of large scale bridging the experimental ponts in these coordinates will form curved line and therefore we can not use fitting procedure to fing correction. Second, fitting procedure requires many experimental points in order to increase accuracy. Applying this method in situation, where only few experimental points available, could lead to large error. In the so-called Modified Compliance Calibration Method (MCC) [5] the formula (6) is actually used. Below the all mentioned calculation methods are compared.

Finally the consumption of energy at crack propagation can be measured directly by area method, using the unloading of specimen after some crack advance

$$G_{IC} = \frac{S}{b\Delta a} \tag{8}$$

where S is the area of one loading-unloading cycle, b is the specimen's width and Δa is crack increment. The area method was used for comparison with calculated G_{IC} values where possible.

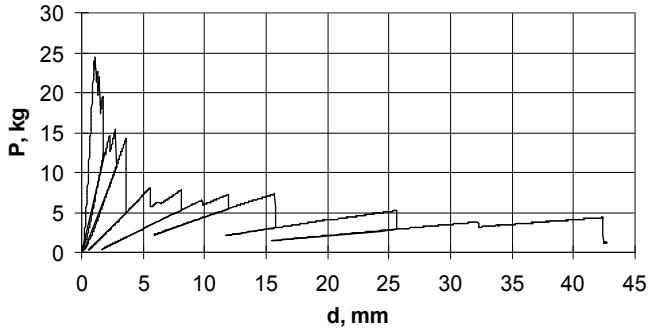

Figure 7: Load deflection curve of carbon-fiber specimen without transverse fibers.

5 Results and analysis

5.1 Fracture toughness of carbon-fiber specimens without fibers in transverse direction.

Four specimens were tested. The thickness of the specimen is 10 mm, width – 15 mm. A typical load–deflection curve is presented in Fig. 7. Crack propagation for all specimens was unstable. The cause of such behaviour is rough structure of crack surface. Crack tip was arrested at some points, until enough elastic energy was accumulated in specimen's arms and then crack propagated dynamically till next stable position. This behaviour is responsible for sharp peaks in load-deflection curves and large scatter in calculated fracture toughness.

Six formulas for fracture toughness calculation were used (Eqs. (4)–(6) and three data reduction techniques from ASTM standard). The results for one specimen are shown in Fig. 8. Results for other specimens are very similar. Values of fracture toughness for all four specimens calculated using Eq. (6) (Fig. 9) lie between 0.4–0.8 kJ/m^2. However, since for energy release rate calculation peak values of load were used, these results should be slightly overestimated. Area method was used for comparison and results are presented in Fig. 10. Results of area method lie between $G_{IC} = 0.4$ – 0.6 kJ/m^2, which coincides rather satisfactory with data in Fig. 9. It should be noted that G_{IC} does not increase with the crack propagation.

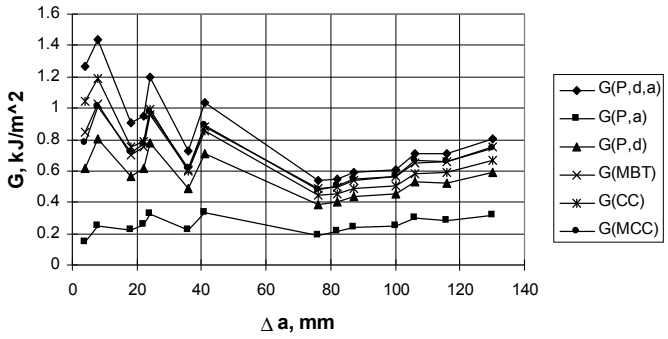

Figure 8: Fracture toughness of carbon-fiber specimen. Six different formulas for G_{IC} calculation were used.

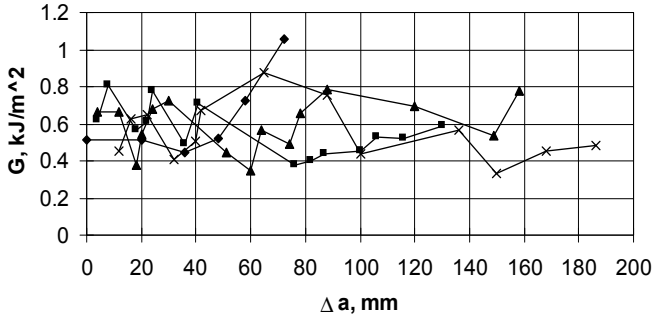

Figure 9: Fracture toughness of carbon-fiber specimens without transverse fibers. Results for all four specimens are obtained using Eq. (6).

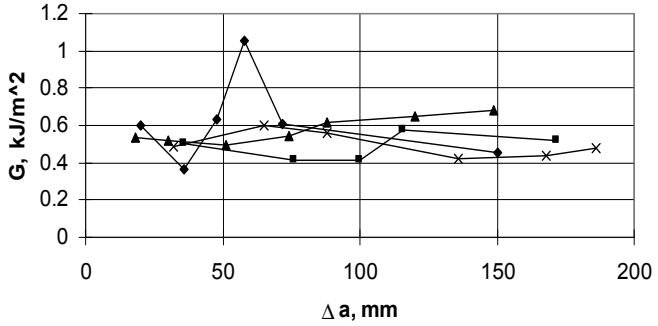

Figure 10: Fracture toughness of carbon-fiber specimens. Results for all four specimens are obtained using area method.

5.2 Fracture toughness of glass-fiber specimens without fibers in transverse direction.

Four specimens were tested. Typical load-deflection curve is shown in Fig. 11. Fiber bridging was observed during loading of all specimens, resulting in R-curve effect. The values of fracture toughness calculated by different formulas are very similar and only results obtained by formula (6) are presented for this material. R-curves for all four specimens calculated using Eq. (6) and area method are presented in Figs. 12 and 13 respectively. The fracture toughness at the crack growth initiation is about 0.3 kJ/m^2 and increases up to 2 kJ/m^2 after crack propagation equal 30 mm. Such R-curve behavior is caused by fiber cross-over during the delamination. The crack opening δ^* at the position of the tip of initial precrack was also measured for these and all following specimens, allowing to calculate bridging laws for these materials. Bridging law, traction at the crack faces versus crack opening, could be calculated using Eq. (9) [6,7].

$$\sigma(\delta) = \frac{\partial G}{\partial \delta^*} \tag{9}$$

The plot of fracture toughness versus crack opening at the initial precrack position and corresponding bridging law are presented in Figs. 14 and 15 respectively.

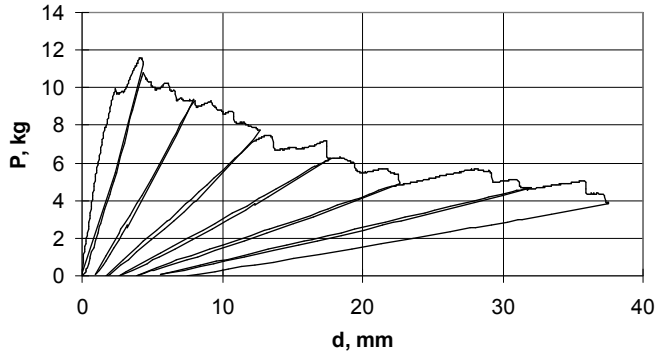

Figure 11: Load-deflection curve of glass-fiber specimen without transverse fibers.

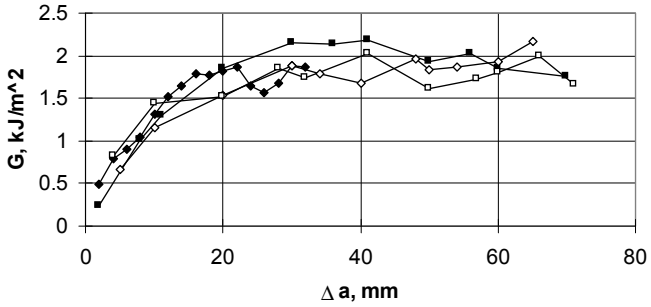

Figure 12: R-curves for glass-fiber specimens without transverse fibers, calculated by Eq. 6.

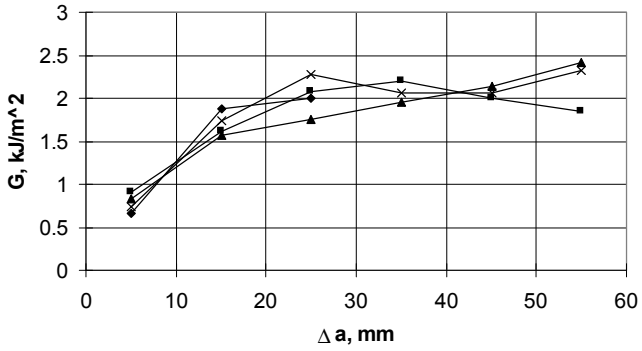

Figure 13: R-curves for glass-fiber specimens without transverse fibers, calculated by area method.

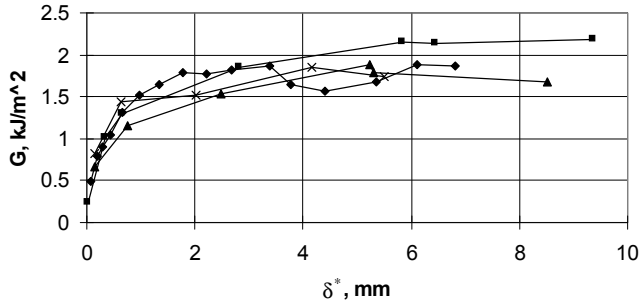

Figure 14: Fracture toughness versus crack opening at the initial precrack position.

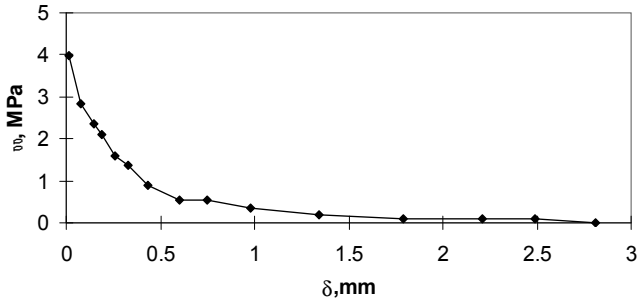

Figure 15: Bridging law for glass-fiber specimens without transverse fibers.

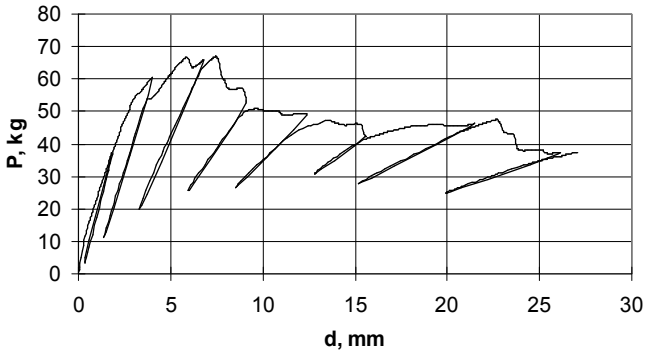

Figure 16: Load-deflection curve of 3D glass-fiber specimen.

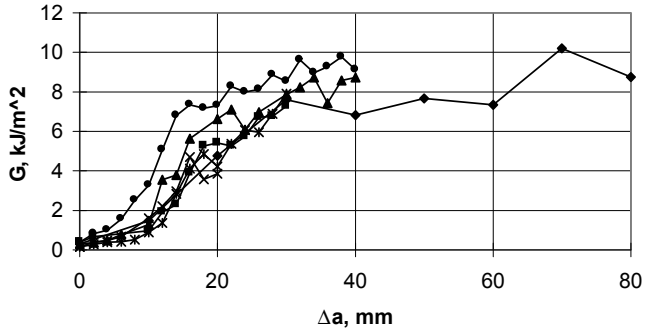

Figure 17: R-curves for six 3D glass-fiber specimens, calculated by Eq. 6.

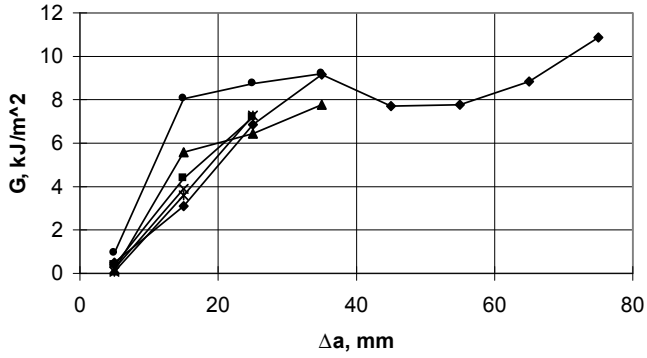

Figure 18: R-curves for six 3D glass-fiber specimens, calculated by area method.

5.3 Fracture toughness of 3D glass-fiber composite.

The load–deflection curve for one specimen is presented in Fig. 16. Corresponded R-curves are presented in Figs. 17 and 18. It is seen that the fracture toughness values directly measured by area method (Fig. 18) practically coincide with data calculated by Eq. (6) (Fig. 17). But using area method much smaller number of points in R-curves can be obtained and details of shape of R-curves are not clear. Therefore the use of Eq. (6) and data on Fig. 17 is preferable for analysis, leaving the data of area method only for control. The initial value of fracture toughness is 0.3 kJ/m^2, and fracture toughness during steady-state crack propagation is about 8 kJ/m^2. Crack growth is initiated by cracking of matrix, at typical G value for regular composite, then it increases. R-curves show (Fig. 17) that G value increases significantly after crack propagation on 10 mm. But it is not the characteristic of the material, because it is known [6,7] that slope of R-curve depends on the geometry of specimen, i.e. on the thickness of composite and glued tabs. More informative and geometry independent parameter is the ICOD (crack opening displacement at the initial precrack tip) in Fig. 19. It is seen that at the initial crack opening equal to 0.2mm the fracture resistance increases 10 times (till 3 kJ/m^2) and reaches 7 kJ/m^2 at ICOD equal to 1 mm. Bridging law, which also can be considered as characteristic of material, is presented according to Eq. (9) in Fig. 20.

In Fig. 20 the bridging law for glass fiber composite without transverse fibers is also shown (from Fig. 15) for comparison. The difference is clearly seen. The bridging law of regular laminate composite is nonlinear monotonously decreasing function, and bridging traction almost disappears at crack opening equaling 2mm. In contrary the bridging law for 3D composite has a nonmonotonous character. Initial value of traction is close to the same for regular composite, then significantly increases till crack opening equal 0.5 mm then monotonously drops till the opening of 4 mm. Apparently the high value of bridging traction is caused by resistance of through the thickness fibers which break at opening equal 0.5 mm, and following by the pull out process up to full separation of crack faces.

5.4 Fracture toughness of 3D carbon-fiber composite.

Load–displacement curve for one specimen is presented in Fig. 21. Corresponded R-curves, fracture toughness vs. crack opening and bridging law are presented in Figs. 22–24 respectively. Values of critical fracture toughness in plots are calculated using formula (6). The initial fracture toughness

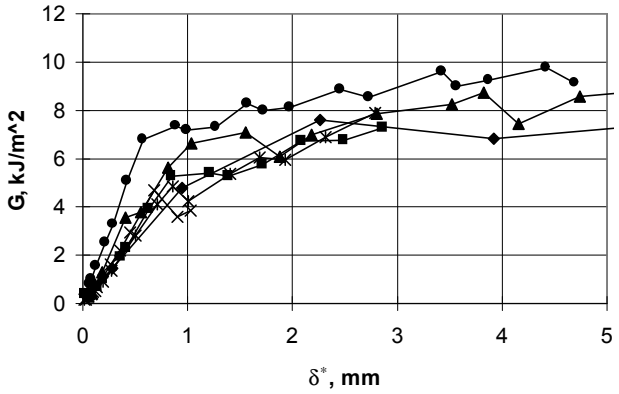

Figure 19: Fracture toughness versus crack opening at initial precrack tip.

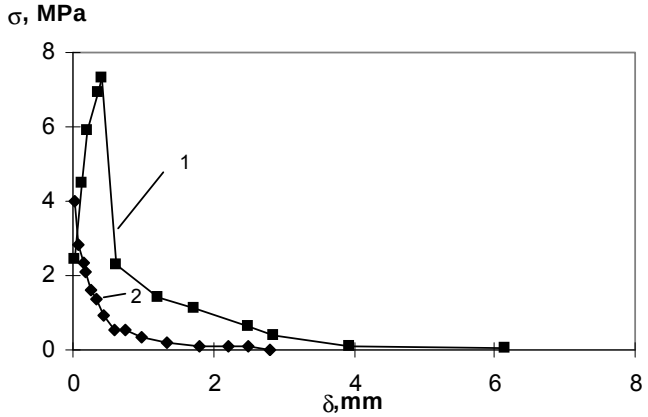

Figure 20: Traction at crack faces versus crack opening for 3D glass fiber composite.

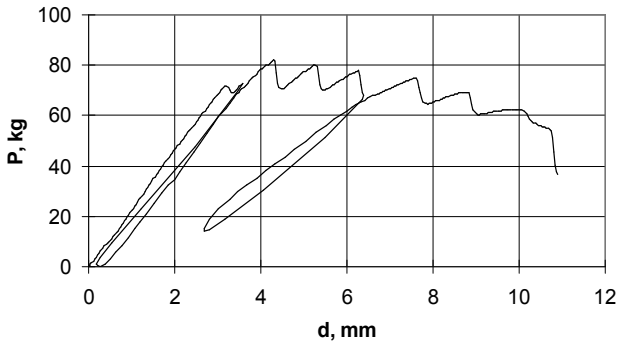

Figure 21: Load-displacement curve of 3D carbon-fiber specimen.

is 0.6 kJ/m^2 and fracture toughness of steady state propagation is about 20 kJ/m^2. It is seen from Fig. 23 that at ICOD equal to 0.25 mm the value of G increases to 6 - 10 kJ/m^2, reaching the steady state propagation value above 20 kJ/m^2 at ICOD equal 0.5 - 1 mm. Looking at the shape of bridging law for specimens with 3D reinforcement, (Figs. 20 and 24), we see one distinct feature of 3D composites—the value of traction at the crack faces is low at the beginning of delamination and reaches its maximum when ICOD equals 0.2–0.5 mm. During this period of crack propagation vertical yarns of through-thickness reinforcement are still not broken and crack propagates due to debonding process between yarns and in-plane layers of composite. After this point the vertical yarns are broken and remaining bridging traction is caused by friction of pull-out of transverse yarns. In Fig. 25 the magnified view of 3D carbon specimen after testing is shown. It is seen that vertical yarns have been pulled out approximately 2mm in length.

It can be concluded that knowledge of bridging law allows to predict critical load for this type of composites much more accurate, then it is possible using linear fracture mechanics. This behavior of bridging law in through-thickness reinforced composites explains the fact, that fracture initiations occurs at low fracture toughness values, but much more energy is required for fracture propagation.

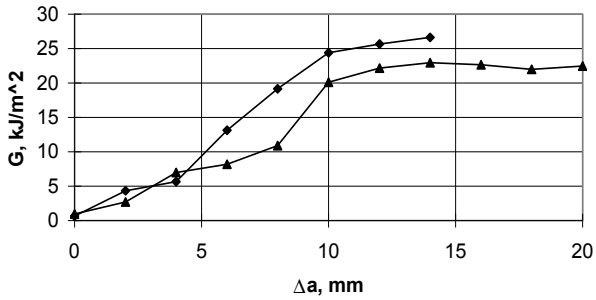

Figure 22: R-curves for 3D carbon-fiber specimens.

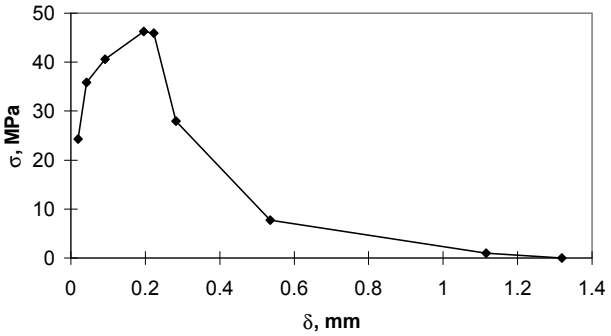

Figure 23: Bridging law (traction at the crack faces versus crack opening).

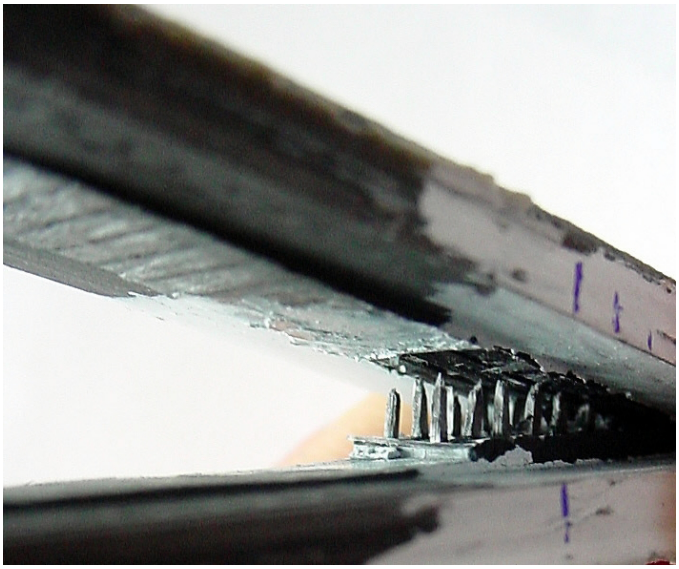

Figure 24: Carbon-fiber 3D specimen after testing (magnified view).

6 Conclusion

1. In order to perform delamination experiments with 3D composite material, modified DCB specimens were designed. The usual composite plates are comparably thin and the arms of DCB specimen break before the crack propagation. The specimen arms should be stiffened by additional tabs glued at both sides of specimen.

2. The comb-like loading device was used and can be recommended for applying high stretching load directly to the crack faces.

3. Different formulas for G_{IC} calculation from experimental data obtained on DCB specimen are verified and analytical formula $G(P, d)$ is found to give the best results, which well coincide with G_{IC} measurements by area method.

4. The additional parameter crack opening displacement at the initial precrack tip (ICOD) is measured to obtain the bridging law, which is characteristic of material, independent on the geometry of specimen. It is recommended to use the graphs G_{IC} vs. ICOD, instead of traditional R-curves (G_{IC} vs. Δa) for characterization of delamination fracture

resistance of composite with extensive bridging.

5. The elaborated methodology is used to estimate the influence of transverse fibers to fracture resistance of laminate glass and carbon fiber composites. For investigated material it is found that the fracture toughness of glass and carbon fiber composite without transverse fibers is close to known fracture toughness data for laminated composites: 0.4–0.5 kJ/m^2 for carbon and 0.2 kJ/m^2 at crack initiation and 2 kJ/m^2 at steady state propagation for glass fiber composite. The microcracking at the tip of crack in 3D woven material starts at the same G_{IC} values as matrix cracking: 0.3–0.6 kJ/m^2. These results correspond to the numerical analysis in [2], where was found that translaminar reinforcement does not delay damage initiation. At crack opening equal to 0.2 mm, the crack propagation resistance increases up to 10 times and for steady state propagation at crack opening 0.5 mm reaches very high values (till 20 kJ/m^2).

Acknowledgment

The authors express a gratitude to 3TEX Inc. and personally to Dr. A.Bogdanovich for rendering the investigated composite plates.

References

[1] Dickinson LC, Farley GL, Hinders MK. Translaminar Reinforsed Composites: A Review. Journal of Composites Technology & Research 1999;21(1):3–5.

[2] Dickinson LC, Farley GL, Hinders MK. Failure Initiation in Translaminar Reinforced Composites. Journal of Composites Technology & Research 2000;22(1):23–32.

[3] Massabo R, Cox BN. Concepts for bridged mode II delamination cracks. Journal of the Mechanics and Physics of Solids 1999;47:1265–1300.

[4] Tanzawa Y, Watanabe N, Ishikawa T. FEM simulation of a modified DCB test for 3-D orthogonal interlocked fabric composites. Composites Science and Technology 2001;61:1097–1107.

[5] ASTM D 5528–94a. Standard test method for mode I interlaminar fracture toughness of unidirectional fiber-reinforced polymer matrix compos-

ites. Annual Book of ASTM Standards, American Society for Testing and Materials, Philadelphia.

[6] Sorensen BF, Jacobsen TK. Large-scale bridging in composites: R-curves and bridging laws. Composites Part A 1998;29:1443–1451.

[7] Tamuzs V, Tarasovs S, Vilks U. Progressive delamination and fiber bridging modeling in double cantilever beam composite specimens. Engineering Fracture Mechanics 2001;68:513–525.

[8] Mohamed MH, Bogdanovich AE, Dickinson LC, Singletary JN, Lienhart RB. A New Generation of 3D Woven Fabric Preforms and Composites. Sampe Journal 2001, May/June.

Paper IV

An integral equation solution for three-dimensional heat extraction from planar fracture in hot dry rock

A. Ghassemi[a], S. Tarasovs[a] and A.H.-D. Cheng[1b]

[a] *Department of Geology and Geological Engineering, University of North Dakota, Grand Forks, ND 58202, USA*
[b] *Department of Civil Engineering, University of Mississippi, University, MS 38677, USA*

Abstract

In the numerical simulation of heat extraction by circulating water in a fracture embedded in geothermal reservoir, the heat conduction in the reservoir is typically assumed to be one-dimensional and perpendicular to the fracture in order to avoid the discretization of the three-dimensional reservoir geometry. In this paper we demonstrate that by utilizing the integral equation formulation with a Green's function, the three-dimensional heat flow in the reservoir can be modelled without the need of discretizing the reservoir. Numerical results show that the three-dimensional heat conduction effect can significantly alter the prediction of heat extraction temperature and the reservoir life as compared to its one-dimensional simplification.

Keywords: hot dry rock; integral equation method; point heat source; geothermal reservoir

[1] Correspondence to: A.H.-D. Cheng, Department of Civil Engineering, University of Mississippi, University, MS 38677, U.S.A. E-mail: acheng@olemiss.edu

1 Introduction

Hot rocks and fluids in the subsurface can be an economical source of energy. The temperature in the subsurface can rise to 350°C at a depth of 5 km; and further to $500 - 1200$°C at 40 km. The hot dry rock (HDR) concept of geothermal energy production involves drilling two or more wells into the reservoir to intersect permeable fractures of natural or man-made origin, injecting cold water into one part of the well system, and recovering hot water from the other (Figure 1). A comprehensive review of the concept of HDR systems may be found in Hayashi *et al.* [1].

Physical and mathematical models play an important role in the planning and development of geothermal reservoirs. A number of analytical and numerical solutions exist for the prediction of heat extraction from fracture systems in geothermal reservoirs. See, for example, Reference [2] for a review. The physical mechanisms modelled are sometimes complicated and include mechanical, hydraulic, thermal, and chemical effects and their coupling. The geometry, however, is often simplified. Particularly, with only a few exceptions such as the finite element solution by Kolditz [3], Kolditz and Clauser [4], and Kohl *et al.* [5] and the boundary element model by Cheng *et al.* [6], the heat conduction in the reservoir is typically modelled as one-dimensional heat flow perpendicular to the fracture surface [7–10]. The primary reason for such simplification is the inefficiency in modelling an unbounded three-dimensional domain by numerical discretization.

In this work, we emphasize the three-dimensional heat conduction effect in hot dry rock. The physical mechanisms considered are limited to the advective heat transport in the fracture by fluid flow and the heat exchange with the reservoir. The numerical difficulty of modelling a three dimensional, unbounded domain is overcome by utilizing the integral equation formulation and the three-dimensional Green's function of heat conduction. The need for discretizing the reservoir is entirely eliminated, and the final numerical solution system involves only the twodimensional fracture plane, resulting in a much more efficient numerical scheme. The three-dimensional heat conduction effect is investigated against its one-dimensional simplification. It is demonstrated that the simplification of reservoir heat flow to one dimension can significantly underestimate the extraction temperature and reservoir life.

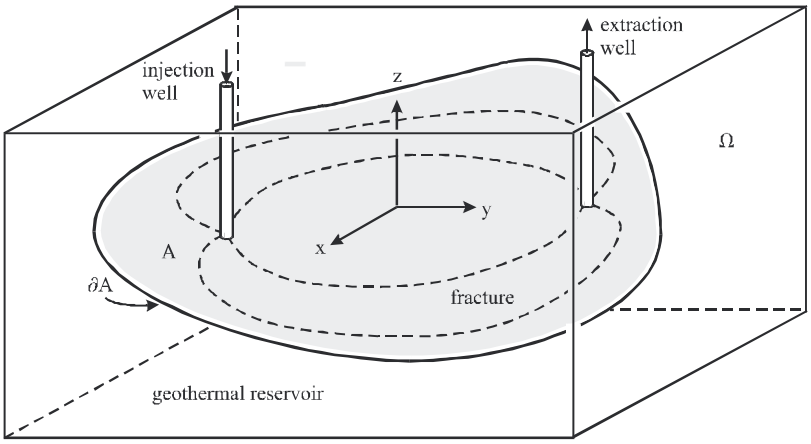

Figure 1: Heat extraction from a planar fracture.

2 Governing Equations

2.1 Fluid flow

Figure 1 gives a schematic view of heat extraction from a hot dry rock system by circulating water through a natural or man-made fracture. The fracture is assumed to be flat, of finite size and with arbitrary shape. The geothermal reservoir, on the other hand, is of infinite extent. Other physical assumptions are similar to these postulated in Reference [6]. Specifically, it is assumed that the geothermal reservoir is impermeable to water and is non-deformable. It has constant heat conduction properties. The heat storage and dispersion effects in the fracture fluid flow are negligible. We further postulate that the fracture width is small such that the flow in the fracture is laminar and governed by the lubrication flow equation:

$$\nabla_2 p(x,y) = -\frac{\pi^2 \mu}{w^3(x,y)}\,\mathbf{q}(x,y); \qquad x,y \in A \tag{2}$$

where ∇_2 is the gradient operator in two spatial dimensions (x and y), p is the fluid pressure, μ the fluid viscosity, w the fracture width, and A the fracture surface (see Figure 1). We note that:

$$\mathbf{q} = w\,\overline{\mathbf{v}} \tag{3}$$

is the discharge per unit width, and $\overline{\mathbf{v}}$ is the average flow velocity given by

$$\overline{\mathbf{v}}(x,y) = \frac{1}{w(x,y)} \int_0^{w(x,y)} \mathbf{v}(x,y,z)\, dz \tag{4}$$

where $\mathbf{v}$ is the flow velocity.

Assuming that the fluid is incompressible, the reservoir is impermeable to fluid flow, and the fracture width does not change with time, we can write the fluid continuity equation as

$$\nabla_2 \cdot \mathbf{q}(x,y) = Q\,\delta(x-x_e, y-y_e) - Q\,\delta(x-x_i, y-y_i) \tag{5}$$

where $\nabla_2 \cdot$ is the divergence operator in two dimension. In the above we have considered an injection well located at (x_i, y_i), and an extraction well at (x_e, y_e), both with discharge Q, and δ is the Dirac delta function.

Combining (1) and (4), we obtain the following second order partial differential equation

$$\nabla_2 \cdot \left[w^3(x,y)\, \nabla_2\, p(x,y)\right] = \pi^2 \mu\, Q\, [\delta(x-x_i, y-y_i) - \delta(x-x_e, y-y_e)] \tag{6}$$

which is subject to the boundary condition

$$\frac{\partial p}{\partial n} = 0 \qquad \text{on } \partial A \tag{7}$$

where ∂A is the rim of the planar fracture (Figure 1), and n is the outward normal of ∂A. With known fracture width, the above equation can be solved for the pressure distribution in the fracture. The discharge $\mathbf{q}$ and average velocity $\overline{\mathbf{v}}$ are then obtained from (1) and (2).

2.2 Heat transport

The heat transport takes place both in the geothermal reservoir and the fracture. For the geothermal reservoir, the heat conduction is governed by the three-dimensional diffusion equation:

$$K_r \nabla_3^2\, T(x,y,z,t) = \rho_r c_r \frac{\partial T(x,y,z,t)}{\partial t}, \qquad x,y,z \in \Omega \tag{8}$$

where T is the temperature, ρ_r is the rock density, c_r is the specific heat of rock, ∇_3^2 is the Laplacian operator in three dimensions, and Ω represents the infinite domain that is the geothermal reservoir (Figure 1).

For heat transport in the fracture, in addition to the heat storage and diffusion terms as found in (7), we also need to consider advection by fluid

flow and the heat source effects. However, under the conditions of relatively large advection velocity and the continuous injection of cooling water, it can be demonstrated that the heat storage and diffusion effects are negligible [6,11]. Dropping these terms, the governing equation becomes

$$\begin{aligned}\rho_w c_w \nabla_2 \cdot [\mathbf{q}(x,y) T(x,y,0,t)] &= 2K_r \left.\frac{\partial T(x,y,z,t)}{\partial z}\right|_{z=0^+} \\ &\quad +\rho_w c_w Q \left[T\left(x_e,y_e,0,t\right)\delta\left(x-x_e,y-y_e\right)\right. \\ &\quad \left.-T_{\text{inj}}\delta\left(x-x_i,y-y_i\right)\right], \qquad x,y \in A\end{aligned} \tag{9}$$

where ρ_w is the water density, c_w is the specific heat of water, K_r is the rock thermal conductivity, and T_{inj} is the injection water temperature. In the above, the term on the left hand side of (8) represents the heat advection by fracture fluid flow, the first term on the right-hand side gives the heat supply through the fracture walls (two sides) by conduction, and the last two terms correspond to a heat sink and a heat source, respectively, caused by the extraction and injection of water. We note that in (8) a single notation $T(x,y,z,t)$ is used to denote the temperature of the rock and the fracture fluid, because temperature is continuous across the two media. The water temperature T_w is equal to the rock temperature on the fracture plane $z=0$, i.e., $T_w(x,y,t) = T(x,y,0,t), \quad x,y \in A$.

Equation (8) can be simplified by expanding the quantities under the divergence operator and utilizing the flow equation (4). It becomes

$$\rho_w c_w \, \mathbf{q}(x,y) \cdot \nabla_2 \, T(x,y,0,t) - 2K_r \left.\frac{\partial T(x,y,z,t)}{\partial z}\right|_{z=0^+} = 0 \tag{10}$$

We notice that the Dirac delta functions are removed from the equation.

The governing equations (7) and (9) are subject to initial and boundary conditions. Before the heat extraction operation, the temperature of the rock and the fracture fluid is assumed to be at a constant,

$$T(x,y,z,0) = T_0, \quad x,y,z \in \Omega \tag{11}$$

At the injection point $(x_i, y_i, 0)$, the temperature is equal to that of the injected water:

$$T(x_i,y_i,0,t) = T_{\text{inj}}, \quad t > 0 \tag{12}$$

The extraction temperature $T(x_e,y_e,0,t)$ is unknown. It is of interest to note that there is no explicit boundary or interfacial condition for the geothermal reservoir. The heat flux and temperature continuity at the interface with the fracture is automatically contained in the coupling term

in (9) and the inherent assumption of a single temperature for the entire system. The only boundary value introduced to the system is the injection temperature shown in (11).

2.3 Normalized solution system

It is desirable to normalize the solution field to become dimensionless with value between zero and one. Therefore, we introduce the normalized temperature deficit given by

$$T_d = \frac{T_0 - T}{T_0 - T_{\text{inj}}} \tag{13}$$

Equations (7) and (9) retain their original forms under this new variable,

$$K_r \nabla_3^2 T_d(x, y, z, t) = \rho_r c_r \frac{\partial T_d(x, y, z, t)}{\partial t} \tag{14}$$

$$\rho_w c_w \, \mathbf{q}(x, y) \cdot \nabla_2 T_d(x, y, 0, t) - 2K_r \left. \frac{\partial T_d(x, y, z, t)}{\partial z} \right|_{z=0^+} = 0 \tag{15}$$

The initial condition is then

$$T_d(x, y, z, 0) = 0 \tag{16}$$

and the boundary condition becomes

$$T_d(x_i, y_i, 0, t) = 1 \tag{17}$$

2.4 Laplace transform

To facilitate the treatment of time variable, we apply Laplace transform to the above equations and obtain:

$$K_r \nabla_3^2 \widetilde{T}_d(x, y, z, s) = s \rho_r c_r \widetilde{T}_d(x, y, z, s) \tag{18}$$

$$\rho_w c_w \, \mathbf{q}(x, y) \cdot \nabla_2 \widetilde{T}_d(x, y, 0, s) - 2K_r \left. \frac{\partial \widetilde{T}_d(x, y, z, s)}{\partial z} \right|_{z=0^+} = 0 \tag{19}$$

$$\widetilde{T}_d(x_i, y_i, 0, s) = \frac{1}{s} \tag{20}$$

where the wiggle overbar denotes the Laplace transform and s is the transform parameter. We note that the initial condition (15) has been absorbed into (17). Equations (17)–(19) hence form a complete solution system.

For later reference, we also introduce the alternative form of (18), based on (8), as follows

$$\rho_w c_w \nabla_2 \cdot \left[\mathbf{q}(x,y)\widetilde{T}_d(x,y,0,s)\right] - 2K_r \left.\frac{\partial \widetilde{T}_d(x,y,z,s)}{\partial z}\right|_{z=0^+} \tag{21}$$
$$= \rho_w c_w Q \left[\widetilde{T}_d(x_e,y_e,0,s)\,\delta(x-x_e,\,y-y_e) - \frac{1}{s}\,\delta(x-x_i,\,y-y_i)\right]$$

3 Integral Equation Formulation

The system of equations (17)–(19) is defined in three spatial dimensions. We shall demonstrate that by utilizing Green's function of three-dimensional diffusion equation, the solution system can be reduced to a two-dimensional integral equation. The numerical discretization is performed on the fracture surface only, significantly reducing the computational cost.

The Laplace transform of temperature deficit in the reservoir due to a continuous point heat source of unit magnitude and located at (x', y', z') is given by the fundamental solution of the modified Helmholtz equation (17) as

$$\widetilde{G} = \frac{1}{4\pi K_r}\frac{1}{R}\exp\left(-\sqrt{\frac{\rho_r c_r s}{K_r}}\,R\right) \tag{22}$$

where

$$R = \sqrt{(x-x')^2 + (y-y')^2 + (z-z')^2} \tag{23}$$

is the Euclidean distance. The temperature in the reservoir due to a distribution of sources on the fracture surface A is then written as

$$\widetilde{T}_d(x,y,z,s) = \frac{1}{4\pi K_r}\int_A \widetilde{\mu}\left(x',y',s\right)\,\frac{1}{R_1}\exp\left(-\sqrt{\frac{\rho_r c_r s}{K_r}}\,R_1\right)\,dx'dy' \tag{24}$$

where $\widetilde{\mu}$ is the source intensity, and

$$R_1 = \sqrt{(x-x')^2 + (y-y')^2 + z^2} \tag{25}$$

We realize that the heat lost in the reservoir is just the heat gained by the fracture fluid through the wall; hence the source strength is

$$\widetilde{\mu}\left(x,y,s\right) = -2K_r \left.\frac{\partial \widetilde{T}_d(x,y,z,s)}{\partial z}\right|_{z=0^+} \tag{26}$$

According to (18), the heat source can also be expressed as

$$\widetilde{\mu}\left(x,y,s\right) = -\rho_w c_w\,\mathbf{q}(x,y)\cdot\nabla_2\,\widetilde{T}_d(x,y,0,s) \tag{27}$$

Substituting (26) into (23), we obtain:

$$\begin{aligned}\widetilde{T}_d(x,y,z,s) &= \frac{-\rho_w c_w}{4\pi K_r}\int_A \left[\mathbf{q}(x',y')\cdot\nabla_2\,\widetilde{T}_d(x',y',0,s)\right] \\ &\quad \frac{1}{R_1}\exp\left(-\sqrt{\frac{\rho_r c_r s}{K_r}}\,R_1\right)\,dx'dy'\end{aligned} \tag{28}$$

Equation (27) is the integral equation representation of the solution of temperature at any point (x,y,z) in the reservoir, provided that the temperature on the fracture surface $\widetilde{T}_d(x,y,0,s)$ is known.

To solve the temperature on the fracture surface, we restrict (27) to only points on the fracture surface A, and it becomes

$$\begin{aligned}\widetilde{T}_d(x,y,0,s) &= \frac{-\rho_w c_w}{4\pi K_r}\int_A \left[\mathbf{q}(x',y')\cdot\nabla_2\,\widetilde{T}_d(x',y',0,s)\right] \\ &\quad \frac{1}{r}\exp\left(-\sqrt{\frac{\rho_r c_r s}{K_r}}\,r\right)\,dx'dy'\end{aligned} \tag{29}$$

where

$$r=\sqrt{(x-x')^2+(y-y')^2} \tag{30}$$

Equation (28) is entirely defined on the two-dimensional plane A. Together with the boundary condition (19), it forms a complete solution system for fluid temperature in the fracture.

Equation (28) contains the temperature gradient as an unknown, which requires a finite difference approximation in the numerical solution. Sometimes it is desirable to directly model temperature for better accuracy. An alternative formula of (28) hence can be derived as follows. Utilizing (20) instead of (18) in (26) and (27), we obtain

$$\begin{aligned}\widetilde{T}_d(x,y,z,s) &= \frac{-\rho_w c_w}{4\pi K_r}\int_A \nabla_2\cdot\left[\widetilde{T}_d(x',y',0,s)\mathbf{q}(x',y')\right] \\ &\quad \frac{1}{R_1}\exp\left(-\sqrt{\frac{\rho_r c_r s}{K_r}}\,R_1\right)\,dx'dy' \\ &\quad +\frac{\rho_w c_w Q}{4\pi K_r}\left[\widetilde{T}_d(x_e,y_e,0,s)\frac{1}{R_e}\exp\left(-\sqrt{\frac{\rho_r c_r s}{K_r}}\,R_e\right)\right. \\ &\quad \left.-\frac{1}{s}\frac{1}{R_i}\exp\left(-\sqrt{\frac{\rho_r c_r s}{K_r}}\,R_i\right)\right]\end{aligned} \tag{31}$$

where

$$\begin{aligned}R_e &= \sqrt{(x-x_e)^2+(y-y_e)^2+z^2} \\ R_i &= \sqrt{(x-x_i)^2+(y-y_i)^2+z^2}\end{aligned} \tag{32}$$

The divergence operator in (30) can be relaxed by the divergence theorem

$$\begin{aligned}
& \int_A \nabla_2 \cdot \left[\widetilde{T}_d(x',y',0,s)\mathbf{q}(x',y')\right] \frac{1}{R_1} \exp\left(-\sqrt{\frac{\rho_r c_r s}{K_r}}\, R_1\right)\, dx'dy' \quad (33)\\
= & \int_A \nabla_2 \cdot \left[\widetilde{T}_d(x',y',0,s)\mathbf{q}(x',y') \frac{1}{R_1} \exp\left(-\sqrt{\frac{\rho_r c_r s}{K_r}}\, R_1\right)\right]\, dx'dy' \\
& - \int_A \widetilde{T}_d(x',y',0,s)\mathbf{q}(x',y') \cdot \nabla_2 \left[\frac{1}{R_1} \exp\left(-\sqrt{\frac{\rho_r c_r s}{K_r}}\, R_1\right)\right]\, dx'dy' \\
= & \int_{\partial A} \widetilde{T}_d(x',y',0,s) q_n(x',y') \frac{1}{R_1} \exp\left(-\sqrt{\frac{\rho_r c_r s}{K_r}}\, R_1\right)\, dx'dy' \\
& - \int_A \widetilde{T}_d(x',y',0,s)\mathbf{q}(x',y') \cdot \nabla_2 \left[\frac{1}{R_1} \exp\left(-\sqrt{\frac{\rho_r c_r s}{K_r}}\, R_1\right)\right]\, dx'dy'
\end{aligned}$$

where q_n is the normal component of $\mathbf{q}$ on ∂A. We further note that in (32) the line integral performed over the fracture boundary ∂A vanishes by virtue of the no flux condition $q_n = 0$ as indicated in (6). Substituting (32) into (30) and applying the equation to the fracture surface only, we obtain the alternative solution system to (28) as

$$\begin{aligned}
\widetilde{T}_d(x,y,z,s) = & \frac{-\rho_w c_w}{4\pi K_r} \int_A \widetilde{T}_d(x',y',0,s)\mathbf{q}(x',y') \\
& \cdot\nabla_2 \left[\frac{1}{r} \exp\left(-\sqrt{\frac{\rho_r c_r s}{K_r}}\, r\right)\right]\, dx'dy' \quad (34)\\
& + \frac{\rho_w c_w Q}{4\pi K_r} \left[\widetilde{T}_d(x_e,y_e,0,s) \frac{1}{r_e} \exp\left(-\sqrt{\frac{\rho_r c_r s}{K_r}}\, r_e\right)\right. \\
& \left. \frac{1}{s}\frac{1}{r_i} \exp\left(-\sqrt{\frac{\rho_r c_r s}{K_r}}\, r_i\right)\right]
\end{aligned}$$

where

$$\begin{aligned}
r_e &= \sqrt{(x-x_e)^2 + (y-y_e)^2} \quad (35)\\
r_i &= \sqrt{(x-x_i)^2 + (y-y_i)^2}
\end{aligned}$$

We note that in this formulation the gradient operator is transferred to the known fundamental solution, which can be exactly executed.

4 Numerical Implementation

The general scheme for solving the system represented by (28) or (33) involves discretizing an arbitrary shaped fracture surface into a number of

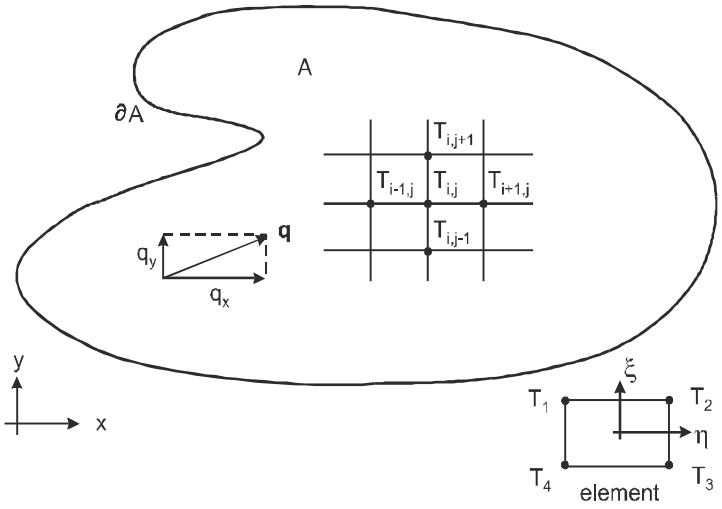

Figure 2: Computational mesh.

elements defined by a total of $n+1$ nodes. An unknown temperature deficit $\widetilde{T}_{\rm d}^{i}$ is associated with each node, with the exception of the injection point, where $\widetilde{T}_{\rm d} = 1/s$ is the imposed boundary condition. As a result, there are n unknown discrete temperatures. Equation (28) or (33) is then applied to the n nodes by selecting in turn their nodal locations as the base point. This produces n equations to solve for the n unknowns. Some detail of the numerical implementation is given below.

In the present work, we choose formulation (28) instead of (33) for the convenience of implementing an upwind scheme similar to the finite difference method. First, we subdivide the domain A into n_e rectangular elements using a finite difference mesh as shown in Figure 2. The area integration in (28) is performed element by element with reference to local co-ordinates (η, ξ) (see Figure 2):

$$\begin{aligned} \widetilde{T}_d(x,y,s) &= \frac{-\rho_w c_w}{4\pi K_r} \sum_{m=1}^{n_e} \int_{A_m} \left[q_x(\eta,\xi) \frac{\partial \widetilde{T}_d(\eta,\xi,s)}{\partial \eta} + q_y(\eta,\xi) \frac{\partial \widetilde{T}_d(\eta,\xi,s)}{\partial \xi} \right] \\ &\quad \frac{1}{r} \exp\left(-\sqrt{\frac{\rho_r c_r s}{K_r}}\, r \right) \, d\eta d\xi \end{aligned} \tag{36}$$

The values of q_x, q_y, $\partial \widetilde{T}_d/\partial \eta$, and $\partial \widetilde{T}_d/\partial \xi$ within the element are interpolated

from their nodal values based on bilinear shape functions; for example

$$\frac{\partial \widetilde{T}_d}{\partial \eta} = \left(\frac{\partial \widetilde{T}_d}{\partial \eta}\right)_1 N_1 + \left(\frac{\partial \widetilde{T}_d}{\partial \eta}\right)_2 N_2 + \left(\frac{\partial \widetilde{T}_d}{\partial \eta}\right)_3 N_3 + \left(\frac{\partial \widetilde{T}_d}{\partial \eta}\right)_4 N_4 \qquad (37)$$

where the subscripts $(\ )_i$ denote the discrete nodal values; and

$$\begin{aligned} N_1 &= \frac{1}{4}(1-\eta)(1-\xi) \qquad (38)\\ N_2 &= \frac{1}{4}(1+\eta)(1-\xi)\\ N_3 &= \frac{1}{4}(1+\eta)(1+\xi)\\ N_4 &= \frac{1}{4}(1-\eta)(1+\xi) \end{aligned}$$

are the shape functions. Values of q_x and q_y are directly specified on the nodes; $\partial \widetilde{T}_d/\partial \eta$, and $\partial \widetilde{T}_d/\partial \xi$ on the other hand, need to be approximated using finite difference formula based on nodal temperature values. Due to the presence of strong advection, an upwind differencing scheme is needed to maintain solution stability. At a grid point (i, j) (see Figure 2), the temperature derivatives are expressed as the backward or the forward differences according to the direction of the flow:

$$\begin{aligned} \left(\frac{\partial \widetilde{T}_d}{\partial \eta}\right)_{i,j} &= \frac{\widetilde{T}_{i,j} - \widetilde{T}_{i-1,j}}{\Delta x}; \quad \text{if } q_x > 0 \qquad (39)\\ \left(\frac{\partial \widetilde{T}_d}{\partial \eta}\right)_{i,j} &= \frac{\widetilde{T}_{i+1,j} - \widetilde{T}_{i,j}}{\Delta x}; \quad \text{if } q_x < 0 \end{aligned}$$

and similarly for $\partial \widetilde{T}_d/\partial \xi$. Substitution of (38) into (36) gives the temperature derivative within an element, which is represented by discrete temperatures not only on the current element, but also on its neighbouring elements. Green's function in (35) is exactly calculated within the elements. An adaptive Gaussian quadrature is used for integration. On each element, 4-point and 9-point rules are applied and the results are compared for convergence. If the accuracy is not satisfactory, the element is continuously subdivided into smaller ones for integration until a specified accuracy is reached. The resulting linear system contains the nodal values of temperature as unknowns. An LU decomposition scheme is then employed to solve the matrix.

The solution obtained above is in the Laplace transform domain. It is necessary to transform the solution back into the time domain. This is

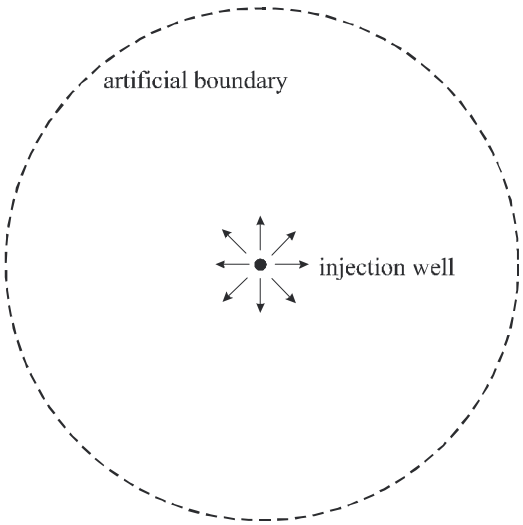

Figure 3: An infinite fracture with an injection well.

achieved by using an approximate Laplace inversion method. The widely used Stehfest method [12,13] is adopted for this purpose.

5 Numerical Examples

5.1 Infinite fracture

We first solve the problem of an infinite planar fracture with a single injection well located at the origin (Figure 3). The initial reservoir temperature is at a constant $T = T_0$. At $t = 0^+$, water is injected at temperature T_{inj} with flow rate Q. Due to axial symmetry, the fluid flow in the infinite fracture is easily resolved as

$$q_r = \frac{Q}{2\pi r} \tag{40}$$

For the numerical solution, the infinite region is truncated using a circle that is large enough to enclose the temperature deficit front to ensure that the boundary effect is small (Figure 3). The following data are used in the simulation [14]

$$\begin{array}{lll} Q = 1 \times 10^{-2}\ \text{m}^3/\text{s}, & \rho_w = 1000\ \text{kg/m}^3, & \rho_r = 2700\ \text{kg/m}^3 \\ K_r = 2.0\ \text{W/m K}, & c_w = 4.2 \times 10^3\ \text{J/kg K}, & c_r = 1.0 \times 10^3\ \text{J/kg K} \end{array}$$

In Figure 4 we plot the normalized temperature deficit, T_{d}, on the fracture ($z = 0$) along the radial direction r, at times $t = 1\times10^7,\ 1\times10^8$, and 1×10^9 s, using symbols connected by dash lines.

To validate the solution, it is desirable to compare the numerical result with known analytical solution. Unfortunately, it is not to our knowledge that any analytical solution simulating threedimensional heat flow exists. Hence, only an indirect comparison can be made using a onedimensional reservoir heat flow model, which is briefly presented below.

The temperature in the fracture varies in the radial direction only, hence (14) simplifies to

$$\frac{Q\rho_w c_w}{2\pi r}\frac{\partial T_d(r,0,t)}{\partial r} - 2K_r\frac{\partial T_d(r,z,t)}{\partial z}\bigg|_{z=0^+} = 0 \tag{41}$$

Assuming that the heat conduction in the reservoir is one-dimensional and perpendicular to the fracture surface, (13) becomes

$$K_r\frac{\partial^2 T_d(r,z,t)}{\partial z^2} = \rho_r c_r\frac{\partial T_d(r,z,t)}{\partial t} \tag{42}$$

The normalized temperature deficit solved from the above set of equations is

$$T_d(r,z,t) = \mathrm{erfc}\left[\left(\frac{\pi K_r r^2}{Q\rho_w c_w} + \frac{z}{2}\right)\sqrt{\frac{\rho_r c_r}{K_r t}}\right] \tag{43}$$

where erfc is the complementary error function. In Figure 4, the analytical solution is shown in solid curves. We observe that the two solutions are very close to each other at early times. As time increases, the difference between them becomes more noticeable, but is still small. Hence the three-dimensional heat flow effect is insignificant in this infinite fracture case.

5.2 Circular fracture

In the second example, heat extraction from a circular fracture is studied. In this case, the fluid flow is no longer simple. Nevertheless, the fluid flow in the fracture induced by multiple injection/extraction wells can still be presented in an exact solution, which is constructed using the method of images [15]. For a fracture of radius R centred at the origin and containing any number of injection and extraction wells, the discharge per unit width

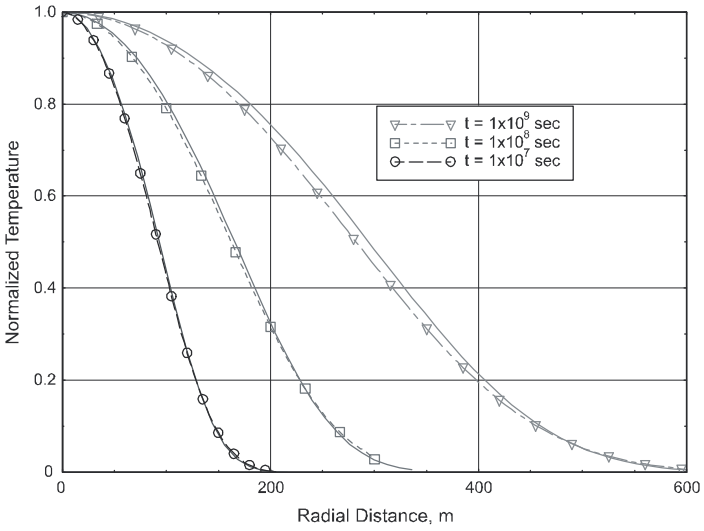

Figure 4: Normalized temperature distribution in the infinite fracture at various times.

is given by

$$q_x = \frac{1}{2\pi}\sum_{i=1}^{n_w} Q_i \left(\frac{x - x_i}{(x-x_i)^2 + (y-y_i)^2} + \frac{r_i^2(xr_i^2 - x_i R^2)}{(xr_i^2 - x_i R^2)^2 + (yr_i^2 - y_i R^2)^2} \right) \tag{44}$$

$$q_y = \frac{1}{2\pi}\sum_{i=1}^{n_w} Q_i \left(\frac{y - y_i}{(x-x_i)^2 + (y-y_i)^2} + \frac{r_i^2(yr_i^2 - y_i R^2)}{(xr_i^2 - x_i R^2)^2 + (yr_i^2 - y_i R^2)^2} \right) \tag{45}$$

where Q_i is the fluid extraction rate of the ith well, x_i and y_i denote the well location, n_w is the number of wells, and

$$r_i = \sqrt{x_i^2 + y_i^2} \tag{46}$$

Due to the condition of mass balance of incompressible fluid, it is necessary that the extraction/injection rates sum to zero

$$\sum_{i=1}^{n_w} Q_i = 0 \tag{47}$$

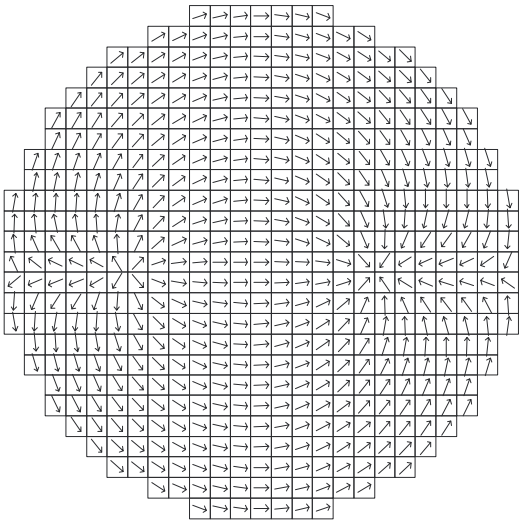

Figure 5: Computational mesh for heat extraction in a circular crack. Flow vectors are shown in arrows.

It is easy to check that the above solution (43) and (44) satisfies the continuity equation (4), and also the boundary condition that normal flux vanishes at the edge of the fracture, $q_n = 0$ at $r = R$.

In this example, we solve the problem of a pair of injection and extraction wells located at $(-a, 0)$ and $(+a, 0)$ with equal but opposite discharge rate ($-Q$ and $+Q$). The resultant flow field is illustrated in Figure 5 for the fracture radius of 50 m and the spacing between two wells that equals 62.5 m.

For the solution of temperature, the fracture surface is discretized into 5024 four-noded bilinear elements similar to those shown in Figure 5. The following data set used in Rodemann [16] is adopted for the numerical solution:

$$\begin{array}{ll} Q = 5 \times 10^{-3}\ \mathrm{m^3/s}, & K_r = 2.58\ \mathrm{W/m\ K}, \\ \rho_w = 1000\ \mathrm{kg/m^3}, & \rho_r = 2650\ \mathrm{kg/m^3} \\ c_w = 4.05 \times 10^3\ \mathrm{J/kg\ K}, & c_r = 1.1 \times 10^3\ \mathrm{J/kg\ K} \end{array}$$

The initial reservoir temperature is 140°C, and the injected water temperature is 60°C. In Figure 6, we plot the water temperature in the fracture in isothermal lines at the time $t = 3$ days. Note that the isolines correspond to 85, 108, 125, 134 and 139°C.

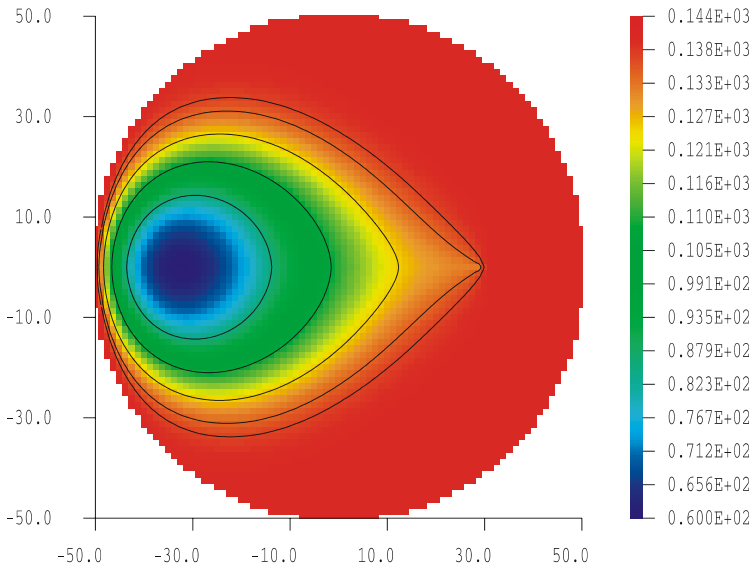

Figure 6: Temperature distribution in a circular fracture at $t = 3$ days based on integral equation solution.

Next, we examine the effect of fracture size on the extraction temperature. In Figure 7, we present the time history of normalized extraction temperature $(T_{\text{extr}} - T_{\text{inj}})/(T_0 - T_{\text{inj}})$ for different fracture sizes, $R =$ 100, 150, 200, 250 and 300 m. The injection and extraction wells are located at $\pm R/2$ on the x-axis. The integral equation solution is presented in dash lines. We clearly observe the trend that the larger the fracture size, the higher the extraction temperature, due to longer residence time.

To compare the effect of three-dimensional versus one-dimensional reservoir heat flow model, we have separately written a Finite Volume Method (FVM) program using the one-dimensional heat flow assumption. The numerical results based on the FVM are plotted in solid lines in Figure 7. We observe that the 1-D model always under-predicts the extraction temperature. This is a consequence of the fact that the part of the reservoir beyond the fracture footprint is effectively cut off from heat supply in the one-dimensional model. The difference between the two models is more significant for smaller fracture sizes. This observation is consistent with the infinite fracture case. The result demonstrates that the use of correct reservoir geometry is important in predicting the life of HDR reservoir with a finite fracture size.

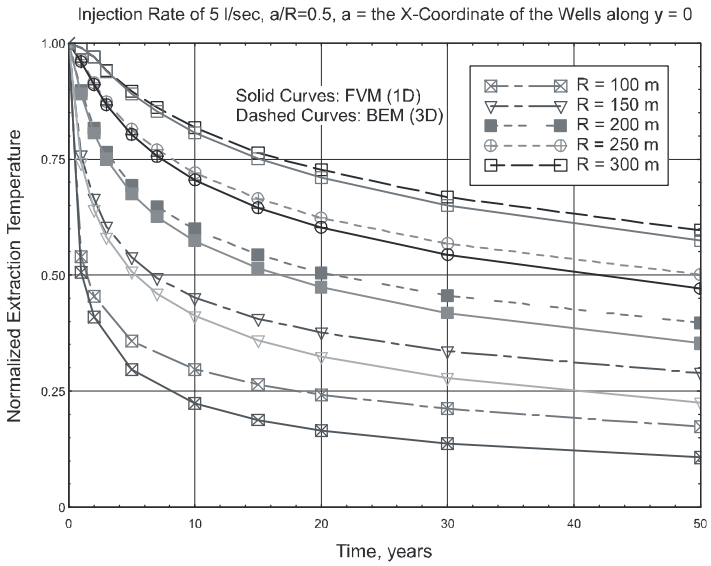

Figure 7: Extraction temperature for various fracture sizes.

5.3 Arbitrary shape fracture

In a last example, we consider a fracture with arbitrary geometry. Figure 8 shows the fracture and its discretization into surface elements. The heat extraction operation involves 3 wells: one injection well with a flow rate of 10 l/s, and two extraction wells each with a flow rate of 5 l/s. All other reservoir parameters are the same as the preceding example.

In this case, the fluid flow can no longer be calculated by an analytical solution. The Finite Element Method is utilized to solve the potential flow in the two-dimensional fracture geometry. The flow singularities were treated using a singularity extraction and superposition procedure [17]. The resultant flow field is plotted in velocity vectors in Figure 9. The normalized temperature deficit in the fracture after 6 months of operation is shown in contour lines in Figure 10.

6 Summary and Conclusion

In this paper we have presented an integral equation formulation for heat extraction from a planar fracture in an infinite hot dry rock reservoir. Most of the existing work, analytical and numerical, treats the heat conduction in

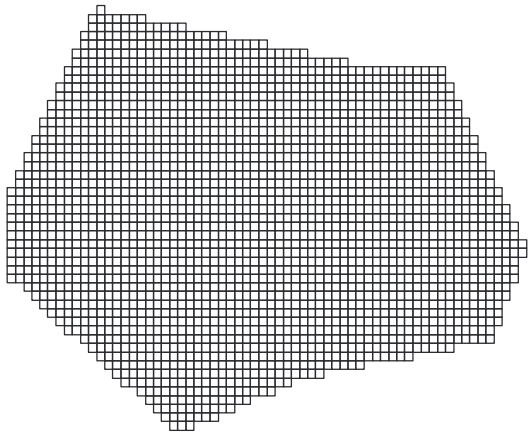

Figure 8: A fracture with arbitrary geometry.

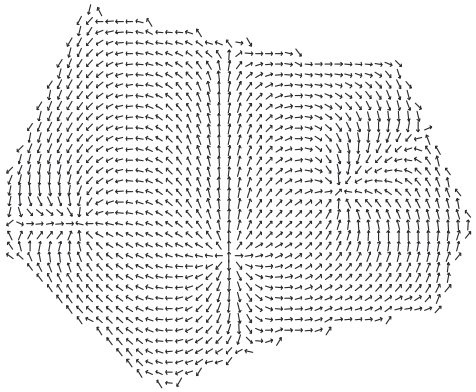

Figure 9: Fluid flow in an arbitrarily shaped fracture with one injection well and two extraction wells.

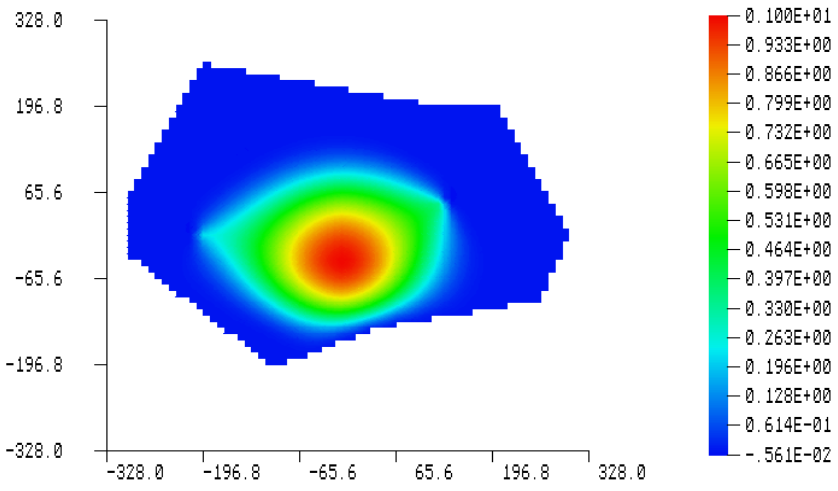

Figure 10: Normalized temperature deficit in a fracture with an injection well and two extraction wells.

the geothermal reservoir as one-dimensional and perpendicular to the fracture. This assumption significantly restricts the heat supply to the HDR system, hence under-predicts the system's performance. One of the reasons that the threedimensional nature of heat conduction is ignored is the difficulty in treating the infinite geothermal reservoir geometry by numerical discretization.

In the present work, we demonstrate that by the use of three-dimensional Green's function for heat conduction and the integral equation formulation, the need for discretizing the three-dimensional reservoir is completely eliminated. The resultant discretization involves the fracture surface only.

To demonstrate the solution algorithm, three examples, an infinite fracture with a single injection well, a circular fracture with a pair of injection and extraction wells, and an arbitrarily shaped fracture with one injection and two extraction wells, are solved. Unfortunately, due to the lack of analytical solution that models the three-dimensional heat conduction, comparisons are made only with an analytical solution and a FVM solution, both with the one-dimensional heat conduction assumption. Partial validation is achieved by observing the consistency in asymptotic behaviour as the fracture size becomes large. The proposed methodology is then used to solve an HDR heat extraction system involving an arbitrarily shaped fracture with multiple injection and extraction wells. Numerical investigation shows that the threedimensional heat conduction can significantly alter the prediction of heat extract temperature and the reservoir life, particularly for smaller fractures.

Although the present integral equation solution has been applied to a single fracture, the same concept can be applied to a reservoirs with a number of fractures. Other improvements that can be implemented in the model include the modelling of reservoir elasticity and thermoelasticity. Work in these directions are under development and will be reported in the future.

Acknowledgments

The financial support of the US Department of Energy under the Grant DE-FG07-99ID13855 is gratefully acknowledged.

References

[1] Hayashi K, Willis-Richards J, Hopkirk RJ, Niibori Y. Numerical models of HDR geothermal reservoirs}a review of current thinking and progress. *Geothermics* 1999; **28**:507–518.

[2] Willis-Richards J, Wallroth T. Approaches to the modeling of HDR reservoirs: a review. *Geothermics*, 1995; **24**: 307–332.

[3] Kolditz O. Modelling flow and heat transfer in fractured rocks: Dimensional effect of matrix heat diffusion. *Geothermics*, 1995; **24**:421–437.

[4] Kolditz O, Clauser C. Numerical simulation of flow and heat transfer in fractured crystalline rocks: Application to the hot dry rock site in Rosemanowes (U.K.). *Geothermics* 1998; **27**:1–23.

[5] Kohl T, Evans KF, Hopkirk RJ, Ryback L. Coupled hydraulic, thermal, and mechanical considerations for the simulation of hot dry rock reservoirs. *Geothermics* 1995; **24**:345–359.

[6] Cheng A-D, Ghassemi A, Detournay E. A two-dimensional solution for heat extraction from a fracture in hot dry rock. *International Journal for Numerical and Analytical Methods in Geomechanics* 2001; **25**:1327–1338.

[7] Abe H, Mura T, Keer LM. Heat extraction from a hydraulically fractured penny-shaped crack in hot dry rock. *Proceedings of the 2nd Workshop Geothermal Reservoir Engineering*, Stanford University, CA, 1976; 200–212.

[8] Bodvarsson G, Tsang CF. Injection and thermal breakthrough in fractured geothermal reservoirs. *Journal of Geophysical Research* 1982; **87**:1031–1048.

[9] Heuer N, Kupper T, Windelberg D. Mathematical model of a hot dry rock system. *Geophysical Journal International* 1991; **105**:659–664.

[10] Kruger P, Dyadkin YD, Gendler S, Artemieva E, Smirnova N. Comparison of thermal cooldown estimates in the Russkie Komarovtsy petrogeothermal reservoir. *Proceedings of the 16th Workshop Geothermal Reservoir Engineering*, Stanford University, CA, 1991; 159–164.

[11] Lowell RP. Comments on 'Theory of heat extraction from fracture hot dry rock' by AC Gringarten, PA Witherspoon, Y Ohnishi. *Journal of Geophysical Research* 1976; **81**:359–360.

[12] Stehfest H. Numerical inversion of Laplace transforms. *Communication ACM* 1970; **13**: 47–49 and 624.

[13] Cheng AH-D, Sidauruk P, Abousleiman Y. Approximate inversion of the Laplace transform. *Mathematica Journal* 1994; **4**:76–82.

[14] Mossop A, Segall P. Injection induces stresses in geothermal fields. *Journal of Geophysical Research*, in press.

[15] Strack ODL. Groundwater Mechanics. Prentice Hall: Englewood Cliffs, NJ, 1989.

[16] Rodemann H. Analytical model calculations on heat exchange in a fracture. In *Urach Geothermal Project*, Haenel R (ed.). Stuttgart, 1982; 351–353.

[17] Liggett JA, Liu PL-F. *The Boundary Integral Equation Methods for Porous Media Flow*. George Allen & Unwin, 1983.

Paper V

Integral Equation Solution of Heat Extraction Induced Thermal Stress in Enhanced Geothermal Reservoirs

A. Ghassemi[a], S. Tarasovs[a] and A.H.-D. Cheng[1b]

[a] *Department of Geology and Geological Engineering, University of North Dakota, Grand Forks, ND 58202, USA*
[b] *Department of Civil Engineering, University of Mississippi, University, MS 38677, USA*

Abstract

During fluid injection in enhanced geothermal systems the thermo-mechanical processes can play an important role. In fact, the phenomena of reservoir seismicity and the variation of injectivity with respect to injection water temperature can be attributed to the induced thermal stresses. In this paper, a three-dimensional integral equation formulation is presented for calculating thermally induced stresses associated with the cooling of a fracture in a geothermal reservoir. By utilizing Green's function in the integral equation, the three-dimensional heat flow and stresses in the reservoir are modeled without discretizing the reservoir. The formulation is implemented in a computer program for the solution of injection into an infinite fracture as well as for the injection/extraction in an arbitrarily shaped fracture.

Keywords: enhanced geothermal system; hot dry rock; geothermal reservoir; integral equation method; Green's function; thermal stress

[1] Correspondence to: A.H.-D. Cheng, Department of Civil Engineering, University of Mississippi, University, MS 38677, U.S.A. E-mail: acheng@olemiss.edu

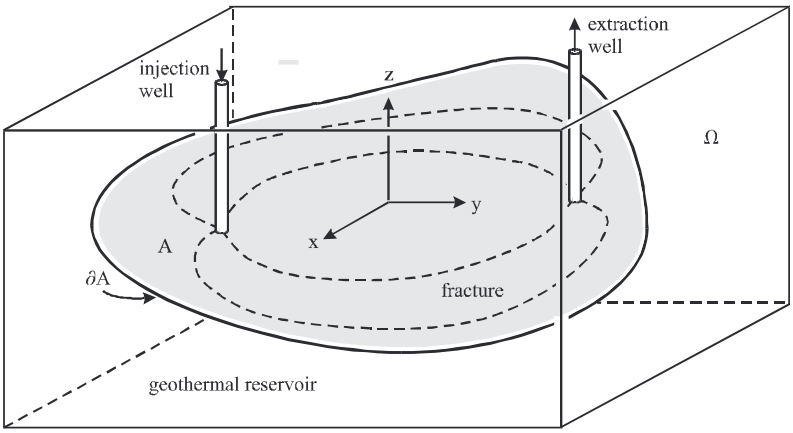

Figure 1: Heat extraction from a planar fracture.

1 Introduction

Hot rocks and geothermal fluids in the subsurface can be an economical source of energy. The temperature in the subsurface rock can rise to 350°C at a depth of 5 km (at less than 3 km in Coso Geothermal Field, central eastern California), and further to 500—1200°C at 40 km. These conditions generally occur in rock masses consisting of igneous and metamorphic rocks with low matrix permeability. Therefore, cracks and fractures are the major pathways for fluid flow and provide the necessary heat exchange surfaces for the extraction of geothermal energy. The production of geothermal energy from this type of reservoir is achieved by water circulation in natural and/or man-made fractures, and is often referred to as enhanced or engineered geothermal systems (EGS). The concept involves drilling two or more wells into the reservoir to intersect permeable fractures, injecting cold water into one part of the well system and recovering hot water from the other (Figure 1). A comprehensive review of this concept, alternatively called the Hot Dry Rock, may be found in Reference [1].

Poromechanical, thermal, and chemical processes can play a significant role in enhanced geothermal systems [2]. These processes occur on various time scales and the significance of their interaction varies with the problem of interest. Of particular importance is the thermo-mechanical coupling during injection operations (time scale of weeks to years). In fact, the variation of injectivity with injection water temperature can be attributed to thermal stresses. Also, thermally induced stresses significantly contribute to seismic-

ity in petroleum and geothermal fields [3, 4]. Stark [4] found that half the earthquakes in the Geysers geothermal field (northern California) seemed to be associated with cold water injection. The mechanism by which seismicity occurs is believed to be mostly shear slip on natural fractures resulting from a reduction of normal stress across the fracture.

The magnitude of the three-dimensional thermal stresses associated with advective cooling has been estimated semi-analytically [5] using an axisymmetric model of injection into a planar reservoir. However, the temperature field in the rock mass is modelled as onedimensional heat flow perpendicular to the fracture surface. A reason for ignoring the threedimensional nature of heat conduction in the reservoir in the above study [5] and in most of the previous studies [6–8] is the difficulty in treating the infinite geothermal reservoir geometry by numerical discretization. However, it has been shown that one- and two-dimensional heat flow models underestimate heat transfer to the fluid from the crack [9]. Thus, rock cooling and the associated thermal stresses should be studied using the coupling of a three-dimensional heat flow model and a three-dimensional elasticity model. It is not to our knowledge that this has been accomplished.

In two of our previous papers [9, 10] we have demonstrated that the use of Green's function in an integral equation formulation can exactly model the heat conduction in infinite reservoir, which is accomplished without the need of discretizing the reservoir. By coupling the integral equation with the heat transport in the fracture, the effect of three-dimensional heat conduction in the reservoir has been properly modelled.

In this paper, we shall extend the above studies to consider the thermal stress induced by water injection into enhanced geothermal reservoirs. Key to the approach is the utilization of Green's function to model not only the three-dimensional heat conduction but also the three-dimensional thermal stress problem, all done without the discretization of the reservoir. The numerical discretization is needed only on the fracture surface. The technique is first applied to the solution of water injection into an infinite fracture for the comparison with a semi-analytical solution for verification purpose. It is then applied to an injection/extraction problem in an arbitrarily shaped fracture.

2 Heat transport and conduction

Before the thermal stress problem can be solved, the fluid flow and heat transport in the fracture and heat conduction in the reservoir must first

be examined. Investigation and treatment of these types of problems have been carried out by Ghassemi *et al.* [9]. A brief presentation of the fluid flow/heat transport model is provided below for the sake of completeness.

A schematic view of the heat extraction by circulating water in a natural or man-made fracture or a fracture zone in rock is illustrated in Figure 1. With only a few exceptions such as the finite element solution by Kolditz [11], Kolditz and Clauser [12], and Kohl *et al.* [13], and the boundary element model by Cheng *et al.* [10] the heat conduction in the reservoir is typically modelled as a one-dimensional heat flow perpendicular to the fracture surface [6–8]. The primary reason for such simplification is the inefficiency in modelling an unbounded threedimensional domain by numerical discretization. The numerical difficulty can be overcome by utilizing the integral equation formulation [10] and the three-dimensional Green's function of heat conduction, allowing three-dimensional problems to be solved in two-dimensional geometry [9].

In this work, the fracture is assumed to be flat, of finite size and with arbitrary shape. The geothermal reservoir, on the other hand, consists of a homogeneous, isotropic rock of infinite extent. Although mineral elasticity and thermal conductivity are anisotropic, a granite that is composed of a random distribution of these minerals tends to have isotropic properties [14]. The presence of cracks and other discontinuities with preferred orientation can cause the rock mass to become thermally and elastically inhomogeneous and anisotropic. However, in the absence of data regarding these properties in *in situ* conditions, the simpler homogeneity and isotropy assumptions are used.

Other physical assumptions are similar to those postulated by Cheng *et al.* [10]. Specifically, it is assumed that the geothermal reservoir is impermeable to water and has constant heat conduction properties. The heat storage and dispersion effects in the fracture fluid flow are negligible, and production rate of hot water is equal to the injection rate in the fracture. It is further postulated that the fracture width does not change during the production, and it is small such that the flow in the fracture is laminar and governed by the lubrication flow equation. Some of these assumptions appear to be idealistic. Nevertheless, in the absence of the detailed knowledge of the fracture and the reservoir in practical cases, these assumptions can provide guidelines for assessment of operational plans and the understanding of phenomena in the field.

The heat transport occurs both in the geothermal reservoir and the fracture. For the geothermal reservoir, the heat conduction is governed by the

three-dimensional diffusion equation:

$$K_r \nabla^2 T_{\rm d}(x,y,z,t) = \rho_r c_r \frac{\partial T_{\rm d}(x,y,z,t)}{\partial t}, \qquad x,y,z \in \Omega \tag{2}$$

where ρ_r is the rock density, c_r is the specific heat of rock, K_r is the rock thermal conductivity, Ω represents the infinite geothermal reservoir (Figure 1), and $T_{\rm d}$ is the normalized temperature deficit with a value between zero and one:

$$T_{\rm d} = \frac{T_0 - T}{T_0 - T_{\rm inj}} \tag{3}$$

in which T is the temperature, T_0 is the initial rock temperature, and $T_{\rm inj}$ is the temperature of injected water.

For heat transport in the fracture the governing equation is

$$\mathbf{q}(x,y) \cdot \nabla T_{\rm d}(x,y,0,t) = \frac{2K_r}{\rho_w c_w} \left. \frac{\partial T_{\rm d}(x,y,z,t)}{\partial z} \right|_{z=0^+} \tag{4}$$

where ρ_w is the water density, c_w is the specific heat of water, and

$$\mathbf{q}(x,y) = \int_0^{w(x,y)} \mathbf{v}(x,y,z)\, dz \tag{5}$$

is the discharge per unit width in the transverse direction of the flow, with $\mathbf{v}$ the flow velocity in the fracture and w the fracture width. In (3), the term on the left-hand side represents the heat advection by fracture fluid flow, and the term on the right gives the heat supply through the fracture walls (two sides) by conduction. We note that in (3) a single notation $T(x,y,z,t)$ is used to denote the temperature of the rock and the fracture fluid, because temperature is continuous across the two media. The water temperature T_w is equal to the rock temperature on the fracture plane $z = 0$, i.e. $T_w(x,y,t) = T(x,y,0,t), \quad x,y \in A$.

These governing equations are subject to initial and boundary conditions. Prior to the heat extraction operation, the temperature of the rock and the fracture fluid is assumed to be a constant, $T(x,y,z,0) = T_0$, and at the injection point $(x_i, y_i, 0)$ the temperature equals that of the injected water: $T(x_i, y_i, 0, t) = T_{\rm inj}$. The extraction temperature $T(x_e, y_e, 0, t)$ is unknown. The initial and the boundary condition can be expressed in terms of $T_{\rm d}$:

$$T_{\rm d}(x,y,z,0) = 0; \qquad T_{\rm d}(x_i,y_i,0,t) = 1 \tag{6}$$

To facilitate the treatment of the time variable, we apply Laplace transform to the above equations and obtain

$$K_r \nabla^2 \widetilde{T}_{\rm d}(x,y,z,s) = s\rho_r c_r \widetilde{T}_{\rm d}(x,y,z,s) \tag{7}$$

$$\mathbf{q}(x,y)\cdot\nabla\widetilde{T}_{\mathrm{d}}(x,y,0,s)=\frac{2K_r}{\rho_w c_w}\left.\frac{\partial\widetilde{T}_{\mathrm{d}}(x,y,z,s)}{\partial z}\right|_{z=0^+} \tag{8}$$

$$\widetilde{T}_{\mathrm{d}}(x_i,y_i,0,s)=\frac{1}{s} \tag{9}$$

where the wiggle overbar denotes the Laplace transform, and s is the transform parameter. Equations (6)–(8) form a complete solution system.

The solution obtained from the above system is in the Laplace transform domain. It is necessary to transform the solution back into the time domain. This is accomplished by solving the above system for a number of different values of s to produce data in the Laplace transform space. An approximate inversion method is then employed to find the solution in time. Particularly, the Stehfest method [15, 16] is chosen for the task.

The system of Equations (6)–(7) is defined in three spatial dimensions. It has been demonstrated that by utilizing Green's function of three-dimensional diffusion equation, the solution system can be reduced to a two-dimensional integral equation [9]. For the temperature on the fracture surface ($z=0$) we obtain

$$\widetilde{T}_d(x,y,0,s)=-\frac{\rho_w c_w}{4\pi K_r}\int_A\left[\mathbf{q}(x',y')\cdot\nabla\widetilde{T}_d(x',y',0,s)\right]\frac{1}{r}\exp\left(-\sqrt{\frac{\rho_r c_r s}{K_r}}\,r\right)dx'dy';\qquad x,y\in A \tag{10}$$

where $r=\sqrt{(x-x')^2+(y-y')^2}$. Equation (9) is entirely defined on the two-dimensional fracture plane A. Together with the boundary condition (8), it forms a complete solution system for fluid temperature in the fracture $\widetilde{T}_d(x,y,0,s)$.

In the numerical implementation, a rectilinear grid like that in Figure 2 is imposed. A finite difference formula (upwind scheme) is used to approximate the temperature gradient in (9). We note that Green's function in (9) has a weak (integrable) singularity $1/r$. Although special quadrature rules can be applied, the regular 9-point Gaussian quadrature produces quite an accurate result. These and other numerical details of solving the integral equation (9) can be found in Reference [9] and are not repeated here. Once the temperature distribution in the fracture is found, the temperature at any point in the reservoir can be evaluated by carrying out the integration over

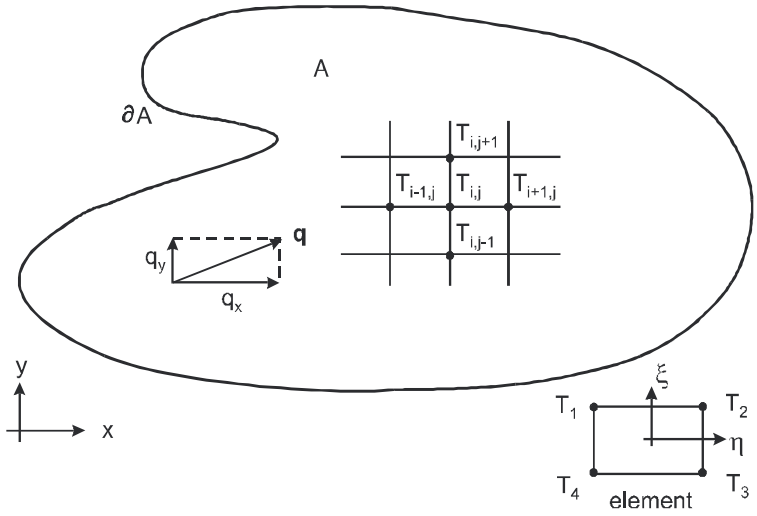

Figure 2: Computational mesh.

the fracture surface A:

$$\widetilde{T}_d(x,y,z,s) = -\frac{\rho_w c_w}{4\pi K_r}\int_A \left[\mathbf{q}(x,y)\cdot\nabla_2\,\widetilde{T}_d(x,y,0,s)\right] \frac{1}{R_1}\exp\left(-\sqrt{\frac{\rho_r c_r s}{K_r}}\,R_1\right)\,dx'dy'; \qquad x,y,z\in\Omega \quad (11)$$

where $R_1 = \sqrt{(x-x')^2+(y-y')^2+z^2}$.

3 Thermal stress

Solving the above system of equations yields the temperature distribution in the geothermal reservoir at any location and any time as the consequence of the injected cooling water. It is the purpose of this paper to evaluate the transient thermal stress induced by the temperature field.

Let us assume that the reservoir rock is isotropic, homogeneous and elastic. The change in temperature $\Delta T = T - T_0$ can be related to the Goodier thermoelastic displacement potential Φ through this Poisson equation:

$$\nabla^2\Phi = m\,\Delta T \quad (12)$$

where

$$m = \frac{(1+\nu)\alpha_T}{(1-\nu)} \quad (13)$$

is the thermoelastic constant, α_T is the coefficient of linear thermal expansion and ν is the Poisson ratio. Here we recall the definition

$$\mathbf{u} = \nabla\Phi \tag{14}$$

where $\mathbf{u}$ is the displacement vector. Expressing the displacements in terms of a potential is possible because thermally generated displacement field is irrotational.

Given a distribution of temperature at any given time, the potential Φ can be calculated from the Poisson integral [17]:

$$\Phi(x,y,z,t) = -\frac{m}{4\pi}\int_{\Omega}\frac{\Delta T(x',y',z',t)}{R}\,dx'\,dy'\,dz' \tag{15}$$

where $R = \sqrt{(x-x')^2+(y-y')^2+(z-z')^2}$. Although (14) can fulfil our purpose for evaluating thermal stresses, we note that it is inefficient to integrate – the integration is in three dimensions and the domain is infinite. Also, to generate data for integration, the value of ΔT needs to be evaluated from (10), which itself is a two-dimensional integration. We hence seek an alternative to (14). This is accomplished by utilizing Green's function of three-dimensional diffusion.

Consider an instantaneous heat source of unit intensity located at (x', y', z') and at time t'. The transient temperature distribution is given by [18]

$$T^*(x-x',y-y',z-z',t-t') = \frac{1}{(\pi\vartheta)^{3/2}\,\rho_r c_r}\exp\left(-\frac{R^2}{\vartheta}\right) \tag{16}$$

where

$$\vartheta = 4\kappa(t-t') \tag{17}$$

and

$$\kappa = \frac{K_r}{\rho_r c_r} \tag{18}$$

is the thermal diffusivity. Solving for the displacement potential defined in (11), we obtain Green's function

$$\Phi^*(x-x',y-y',z-z',t-t') = -\frac{m}{4\pi\rho_r c_r R}\,\mathrm{erf}\left(\frac{R}{\sqrt{\vartheta}}\right) \tag{19}$$

Now, for a distribution of heat sources with the intensity $\mu(x,y,t)$ over the fracture surface A, the resultant displacement potential at any given location and time can be obtained from the Duhamel's principle of superposition:

$$\Phi(x,y,z,t) = \int_0^t\int_A \mu(x',y',t')\;\Phi^*(x-x',y-y',z,t-t')\;dx'dy'dt' \tag{20}$$

Similar to (10), the above equation involves the integration over the finite fracture surface only. To facilitate the treatment of time, we apply Laplace transform to (19) and obtain

$$\widetilde{\Phi}(x,y,z,s) = \int_A \widetilde{\mu}(x',y',s)\ \widetilde{\Phi}^*(x-x',y-y',z,s)\ dx'dy' \tag{21}$$

where

$$\widetilde{\Phi}^*(x-x',y-y',z,s) = -\frac{m}{4\pi s\rho_r c_r R}\left[1-\exp\left(-\sqrt{\frac{s}{\kappa}}R\right)\right] \tag{22}$$

We realize that the source intensity $\widetilde{\mu}$ is just the cooling fluid-induced temperature flux on the fracture surfaces, and

$$\widetilde{\mu} = -2K_r\left.\frac{\partial\widetilde{T}}{\partial z}\right|_{z=0^+} \tag{23}$$

Utilizing the heat transport equation (7) in the above and substituting it into (20), we obtain

$$\begin{aligned}\widetilde{\Phi}(x,y,z,s) &= \frac{m\,\rho_w\,c_w}{4\pi s\rho_r c_r}\int_A\left[\mathbf{q}(x',y')\cdot\nabla\widetilde{T}(x',y',0,s)\right] \\ &\quad \left[\frac{1}{R_1}-\frac{1}{R_1}\exp\left(-\sqrt{\frac{s}{\kappa}}R_1\right)\right]\ dx'\,dy'\end{aligned} \tag{24}$$

The right-hand side of the above equation consists entirely of known quantities, because the fluid flow and the temperature in the fracture has been obtained from the previous stage of solution based on (9). In fact, the same grid system as shown schematically in Figure 2 can be used in the evaluation. So, the problem of finding thermal stresses induced by the injection of cooling fluid is reduced to integration on only the fracture surface, not the entire domain. For finding the displacement potential on the fracture surface, (23) is reduced to

$$\begin{aligned}\widetilde{\Phi}(x,y,0,s) &= \frac{m\,\rho_w\,c_w}{4\pi s\rho_r c_r}\int_A\left[\mathbf{q}(x',y')\cdot\nabla\widetilde{T}(x',y',0,s)\right] \\ &\quad \left[\frac{1}{r}-\frac{1}{r}\exp\left(-\sqrt{\frac{s}{\kappa}}r\right)\right]\ dx'\,dy'\end{aligned} \tag{25}$$

As our interest lies in the stresses, not the displacement potential, (23) and (24) need to be further processed. The stresses are related to the displacement potential by the following formula

$$\widetilde{\sigma}_{ij} = 2G\left(\frac{\partial^2\widetilde{\Phi}}{\partial x_i\partial x_j}-\delta_{ij}\nabla^2\widetilde{\Phi}\right) \tag{26}$$

where δ_{ij} is the Kronecker delta. Similar to (20), it is possible to evaluate the stresses from the integral

$$\widetilde{\sigma}_{ij}(x,y,z,s) = \int_A \widetilde{\mu}(x',y',s)\ \widetilde{\sigma}^*_{ij}(x-x',y-y',z,s)\ dx'dy' \qquad (27)$$

where $\widetilde{\sigma}^*_{ij}$ the Green's function that can be obtained by substituting $\widetilde{\Phi}^*$ in (21) into (25). Equation (26) can be used to evaluate thermal stresses without the need of obtaining the displacement potential first. We note, however, that while the kernel $\widetilde{\Phi}^*$ in (24) is non-singular, $\widetilde{\sigma}^*_{ij}$ in (26) has a strong singularity for integration. Although the singularity can be regularized and removed, in the present work, we choose to avoid the strong singularity and use the nonsingular form (24) to find the displacement potential. The stresses are evaluated using a finite difference approximation of (25). For differentiation in the z-direction, the displacement potential is calculated at some distance (1 element size) above and below the fracture surface for the evaluation of stresses on the fracture surface.

4 Numerical examples

4.1 Injection into infinite fracture

A computer program is developed based on the above procedures. If we compare (23) and (24) with (9) and (10), which was solved in the previous work [9], we can see that the numerical procedure is similar.

As a first example, we solve a case with simple geometry in order to compare with a semianalytical solution. Consider the problem of injection into an infinite planar fracture with the injection well located at the origin (Figure 3). The initial reservoir rock temperature is at a constant $T = T_0$. At $t = 0^+$, water is injected at temperature T_{inj} with flow rate Q. The data for this problem are roughly based on the conditions in the Coso Geothermal Field during the stimulation of Well 86-13 [19], and are shown in Table 1.

Even for this simple geometry, the exact solution actually does not exist. However, if one assumes that the heat conduction in the reservoir is one-dimensional normal to the fracture plane, rather than three-dimensional as indicated in (1), then a closed form solution based on the set of governing

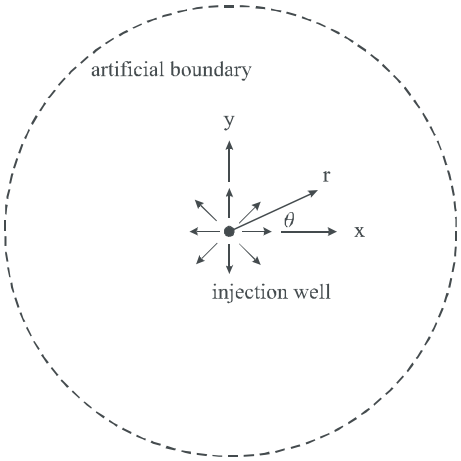

Figure 3: An infinite fracture with an injection well (plan view in the z-direction).

E	Young's modulus	3.75×10^4	MPa
ν	Poisson's ratio	0.25	
ρ_r	rock density	2650	kg/m^3
ρ_w	water density	1000	kg/m^3
c_r	rock heat capacity	790	J/(kg °K)
c_w	water heat capacity	4200	J/(kg °K)
κ	thermal diffusivity	5.1×10^{-6}	m^2/s
α_T	rock linear thermal expansion coefficient	8.0×10^{-6}	1/°K
Q	injection rate	25	ℓ/s
T_{R}	rock temperature	350	°F
T_{inj}	injection water temperature	86	°F
w	initial average fracture aperture for flow	10^{-3}	m

Table 1: Input parameter for infinite fracture problem.

equations

$$\frac{\partial T}{\partial t} + \frac{Q}{2\pi r}\frac{\partial T(r,0,t)}{\partial r} = \frac{2K_r}{\rho_w c_w}\frac{\partial T(r,z,t)}{\partial z} \tag{28}$$

$$K_r \frac{\partial^2 T(r,z,t)}{\partial z^2} = \rho_r c_r \frac{\partial T(r,z,t)}{\partial t} \tag{29}$$

is possible and has been found by Mossop [5] as

$$\begin{aligned} T &= T_0 - (T_0 - T_{\text{inj}})\ \text{erfc}\left[\frac{1/2((2\pi K_r/\rho_w c_w Q)r^2 + z}{\sqrt{\kappa\,(t - (\pi w/Q)r^2)}}\right];\quad \text{for } t - \frac{\pi w}{Q}r^2 \geqslant 0 \\ &= 0;\quad \text{for } t - \frac{\pi w}{Q}r^2 < 0 \end{aligned} \tag{30}$$

We note that (27) has a heat storage term that is not included in (3) as its effect is typically negligible [10]. This solution for T is then used in a singular volume integral to evaluate the thermoelastic stresses [5]. In contrast, the current methodology requires the integration only on the fracture surface.

To isolate the error in the numerical solution, we shall use the exact temperature given in (29) to find the thermal stresses. First, Laplace transform is applied to T and then the heat flux into the reservoir is found from (22) as

$$\widetilde{\mu} = -\frac{4K_r(T_0 - T_{\text{inj}})}{\sqrt{\kappa s}}\exp\left[-2\sqrt{\frac{s}{\kappa}}\left(\frac{\pi K_r}{\rho_w c_w Q}r^2 + z\right)\right] \tag{31}$$

This source intensity is substituted into (20) and the surface integral is performed to find the displacement potential. The numerical results in terms of cooling-induced stresses are presented in Figures 4–6.

For the numerical solution, the mesh pattern shown in Figure 2 is adopted. The results are shown in three different times, 7, 14, and 30 days, using symbols. For each of the solutions, an 80×80 square mesh is used. Although the planar fracture is of infinite horizontal extent, the mesh can cover only a finite region. The proper region to cover can be easily estimated by the speed of the injection fluid front. For the current simulations, the element sizes of 3.25, 3.5 and 4.25 m are, respectively, used for the three times. The 80×80 mesh was selected based on error convergence studies progressing up from a 40×40 and then a 60×60 mesh. The error was reduced and localized around the well. It was determined to be acceptable.

The cooling-induced normal stress σ_{zz} (perpendicular to the fracture) from the stimulation of Well 83-16 [19] is illustrated in Figure 4. The current solution is presented using plotting symbols while the solution by Mossop [5]

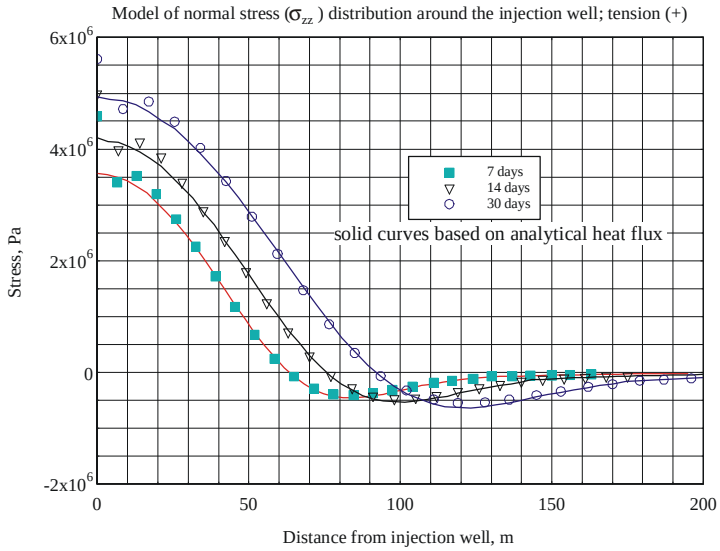

Figure 4: Normal stress (σ_{zz}) distribution on a fracture surface around an injection well.

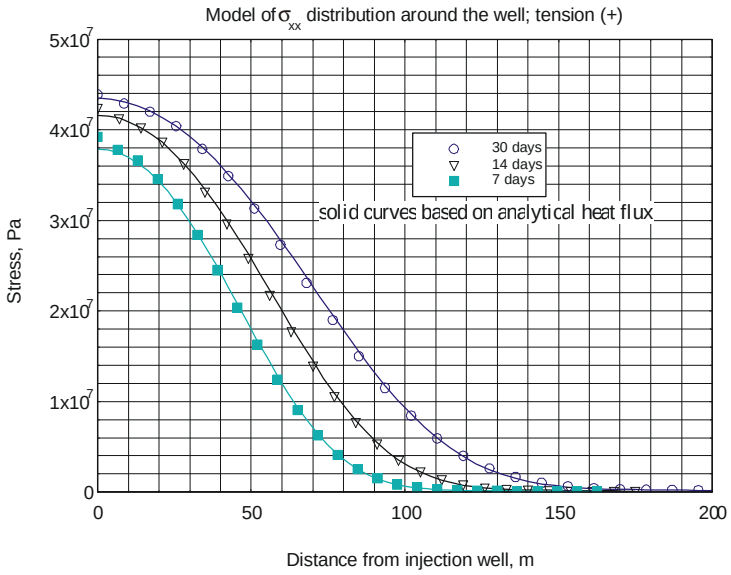

Figure 5: Radial stress (σ_{rr}) distribution around an injection well for various injection times.

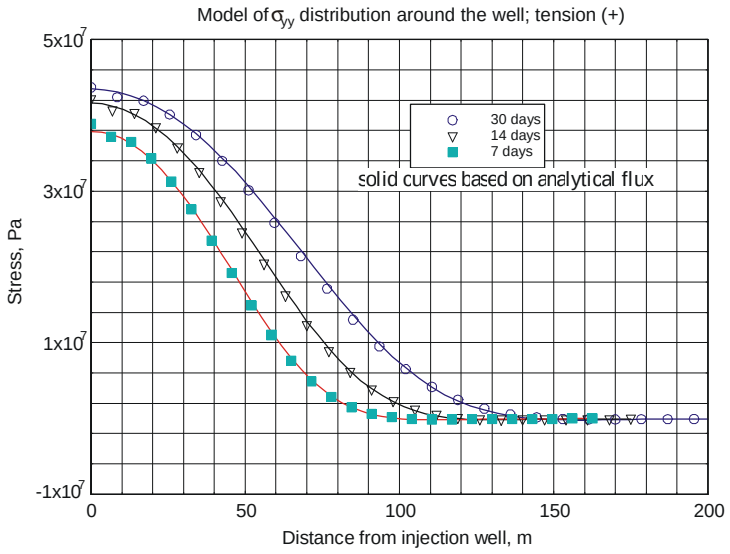

Figure 6: Tangential stress ($\sigma_{\theta\theta}$) distribution around an injection well for various injection times.

is shown in solid lines. We note that except for some error near the injection well, where a flow singularity exists, the current solution compares quite well with the semi-analytical solution. We identify that the main source of error in the stress calculations around the well is due to the relatively large size of the element near the injection well, where the fluid velocity drops sharply. Expressing various derivatives in terms of the finite difference approximation can further enhance the error. But as we commented, the overall accuracy is quite satisfactory.

A few features about the stress distribution in Figure 4 are worth noting. First, we note that the induced thermal stress near the injection well is tensile (meaning an reduction from the *in situ* compressive stress). It is largest near the well as it has the most time for cooling. Away from it, the tensile stress decreases and eventually turns into compressive. This is a result of strain compatibility requirement in three-dimensional elasticity – as rock contracts near the injection well due to cooling, it tends to pull on the exterior rock material inducing a compressive stress ahead of it.

In Figures 5 and 6, we plot σ_{xx} and σ_{yy} along the x-axis, which represent, respectively, the radial (σ_{rr}) and tangential ($\sigma_{\theta\theta}$) normal stresses. The agreement between the numerical and the semi-analytical solution is

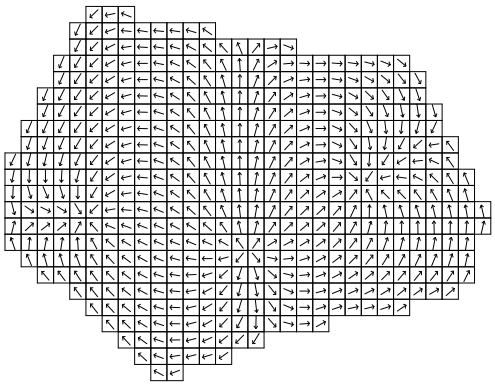

Figure 7: A fracture with arbitrary geometry, its computational mesh and fluid flow field due to one injection well and two extraction wells.

excellent. From the result, we observe that both of these stresses are an order of magnitude larger than the axial stress σ_{zz}. The tangential stress in Figure 6 has a similar pattern as the axial stress–it changes from tensile to compressive at a certain distance. The extent of the compressive stress, however, is much smaller. The radial stress in Figure 5, on the other hand, is tensile throughout. As expected, all induced stresses increase with the injection time.

It is of interest to note that the induced tensile stress near the injection well causes the rock to contract. This can cause the aperture to open wider. For a constant injection rate, the injection pressure will drop due to the increased conductivity. This is indeed observed in Well 83-16 of the Coso Geothermal Field [19]. This thermal stress-induced aperture change may have a effect on the flow pattern, which in turn affects the heat transport. This coupled effect is not contained in the current model. However, if the injection is controlled by a constant flow rate, not by pressure, and the flow pattern is radial as in the current case, then only the injection pressure will change and the heat transport pattern will not. The above prediction of heat extraction is correct in spite of the thermal stress-induced aperture change. The pressure field can be calculated at any given instant with the known aperture width.

4.2 Arbitrary shape fracture

The numerical procedures can also be applied to an injection/extraction operation involving an arbitrarily shaped fracture. Consider a fracture with arbitrary geometry. Figure 7 shows one such fracture and its discretization into surface elements. The fracture surface is divided into 3384 rectangular elements. The heat extraction operation involves 3 wells: one injection well with flow rate 10 l/s and two extraction wells each with flow rate 5 l/s. Assume that the rock and fluid properties are given by $c_w = 4.2 \times 10^3$ J/kg K, $c_r = 1.0 \times 10^3$ J/kg K, $\rho_w = 1000$ kg/m^3, $\rho_r = 2700$ kg/m^3 and $K_r = 2.0$ W/m K. The reservoir and the injection water temperature are, respectively, 200 and 20°C. Also, $E = 4.5$ GPa and $\alpha_T = 1.0 \times 10^{-5}$ K^{-1}. All other reservoir parameters are the same as the preceding example.

In the arbitrary shape fracture case, we first need to solve the incompressible fluid flow in the two-dimensional fracture geometry. Based on continuity, the governing equation for the fluid discharge is

$$\nabla \cdot \mathbf{q}(x, y) = -\sum_{i=1}^{n} Q_i \delta(x - x_i, y - y_i) \tag{32}$$

where $\nabla\cdot$ is the divergence operator in two dimensions, Q_i the injection rate at well i, which is negative for extraction, (x_i, y_i) the well location, and δ the Dirac delta function. As in lubrication theory, the flow in the fracture is driven by the pressure gradient

$$\nabla p(x, y) = -\frac{\pi^2 \mu}{w^3} \mathbf{q}(x, y) \tag{33}$$

where p is the fluid pressure, μ the fluid viscosity, and w the fracture width. Combining the above, we obtain

$$\nabla^2 p(x, y) = \frac{\pi^2 \mu}{w^3} \sum_{i=1}^{n} Q_i \delta(x - x_i, y - y_i) \tag{34}$$

which is subject to the boundary condition

$$\frac{\partial p}{\partial n} = 0 \qquad \text{on } \partial A \tag{35}$$

where ∂A is the rim of the planar fracture (Figure 1), and n is the outward normal of ∂A. With known fracture width, the above equation can be solved for the pressure distribution in the fracture.

The solution of (33) and (34) can be handled by many methods. The finite element method is utilized here. To obtain smooth solution, the flow singularities at the injection and extraction points are treated using a singularity extraction and superposition procedure [20]. In the presence of sources and sinks, we decompose the pressure field into a homogeneous solution and a particular solution:

$$p = p_h + p_p \tag{36}$$

The particular solution is

$$p_p = \frac{\pi\mu}{2w^3} \sum_{i=1}^{n} Q_i \ln r_i \tag{37}$$

where $r_i = \sqrt{(x - x_i)^2 + (y - y_i)^2}$. The homogeneous part satisfying

$$\nabla^2 p_h(x, y) = 0 \tag{38}$$

and the boundary condition

$$\frac{\partial p_h}{\partial n} = -\frac{\partial p_p}{\partial n} \qquad \text{on } \partial A \tag{39}$$

is without singularities. The p_h field treated by the FEM is then smooth and accurate. The flux values are then obtained as

$$\begin{aligned} q_x &= -\frac{w^3}{\pi^2\mu}\left(\frac{\partial p_h}{\partial x} + \frac{\partial p_p}{\partial x}\right) \\ q_y &= -\frac{w^3}{\pi^2\mu}\left(\frac{\partial p_h}{\partial y} + \frac{\partial p_p}{\partial y}\right) \end{aligned} \tag{40}$$

The resultant flow field is shown in Figure 7.

The temperature distributions on the fracture surface after 20 years of operation is shown in Figure 8. The large white region (about 20°C) around the injection well (see Figure 7 for injection well location) indicates that heat depletion has reached a large part of the reservoir at that time. Figure 9 plots the normal thermal stress σ_{zz} on the fracture surface. We observe that a large tensile region (dark shade) is developed around the injection well. Outside the fracture region, we find compression zones (in light shade) which is consistent with the preceding case of single injection well. We also note that compression zones are developed just behind the extraction wells. As before, we note some error at and near the injection/extraction wells, where a flow singularity exists. The sensitivity of the results to mesh size is similar to that described in the previous section, i.e. improved accuracy is achieved by using a finer mesh.

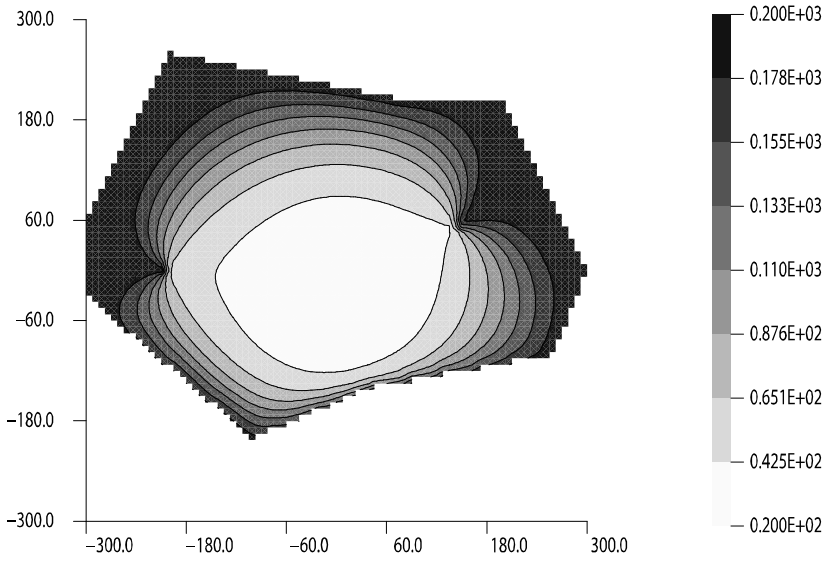

Figure 8: The temperature distribution (°C) on the fracture surface after 20 years of operation.

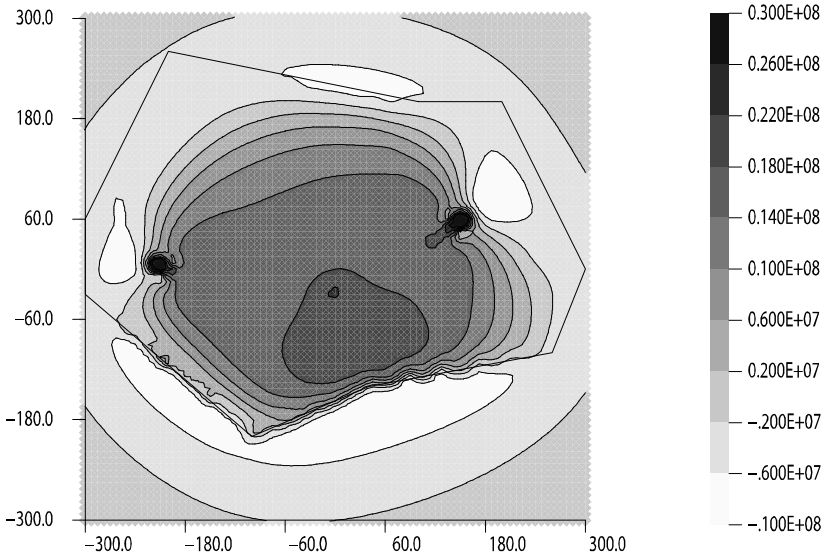

Figure 9: The normal stress (Pa) distribution on the fracture surface after 20 years of operation.

5 Summary and conclusion

An integral equation formulation for three-dimensional heat extraction from a planar fracture in an infinite hot rock reservoir has been used to calculate the temperature and heat flux distributions within the crack and the formation. The resulting transient temperature field is then employed in another integral scheme to determine the distribution of three-dimensional thermal stresses induced by the cooling. This is in contrast to most existing works, analytical and numerical, that treat the heat conduction in the geothermal reservoir as one-dimensional and perpendicular to the fracture. For several numerical works that treat three-dimensional heat flow and thermal stresses, the three-dimensional infinite reservoir needs to be discretized. In comparison, the present integral equation scheme only discretizes the planar fracture surface, which is a much reduced numerical solution system.

The mathematical formulation and numerical implementation were verified by solving a problem with simple geometry involving a single injection well in an infinite fracture. The comparison of the result with a semi-analytical solution was satisfactory. Next, the temperature history and the thermally induced stresses were calculated for an injection–extraction experiment in the field. It has been found that not only tensile stresses develop due to the cooling; compressive stresses are also found in the range just outside the fracture or the fluid front. Near the injection well, the tensile stress is expected to increase the fracture aperture width and reduce the injection pressure. This is consistent with the observation in the field.

Although the present integral equation solution is applied to only a single fracture, the same methodology can be applied to a reservoir with multiple fractures. One issue that is not addressed in this article is the thermal stress-induced fracture response in the reservoir, which leads to a change in aperture width. This width change may have the coupled effect of causing the flow pattern change. Works in these directions are under development and will be reported in the future.

Acknowledgments

The financial supports of the U.S. DOD (N-68936-02-C-0214) and University of North Dakota Faculty Seed Money Program are gratefully acknowledged.

References

[1] Hayashi K, Willis-Richards J, Hopkirk RJ, Niibori Y. Numerical models of HDR geothermal reservoirs – a review of current thinking and progress. *Geothermics* 1999; **28**:507–518.

[2] Ghassemi A, Zhang Q. Poro-thermoelastic mechanisms in wellbore stability and reservoir stimulation. *Proceedings of the 29th Stanford Geothermal Workshop*, February 2004; 295–301.

[3] Sherburn S. Seismic monitoring during a cold water injection experiment, Wairakei Geothermal Field: preliminary results. *Proceedings of the 6th New Zealand Geothermal Workshop*, vol. 6. 1984; 129–133.

[4] Stark MA. Imaging injected water in the Geysers reservoir using microearthquakes data. *Geothermal Resources Council Transactions* 1990; **14(II)**:1697–1704.

[5] Mossop A. Seismicity, subsidence and strain at the Geysers geothermal field. *Ph.D. Dissertation*, Stanford University, 2001.

[6] Bodvarsson G, Tsang CF. Injection and thermal breakthrough in fractured geothermal reservoirs. *Journal of Geophysical Research* 1982; **87**:1031–1048.

[7] Heuer N, Kupper T, Windelberg D. Mathematical model of a hot dry rock system. *Geophysical Journal International* 1991; **105**:659–664.

[8] Kruger P, Dyadkin YD, Gendler S, Artemieva E, Smirnova N. Comparison of thermal cooldown estimates in the Russkie Komarovtsy petrogeothermal reservoir. *Proceedings of the 16th Workshop Geothermal Reservoir Engineering*, Stanford University, CA, 1991; 159–164.

[9] Ghassemi A, Tarasovs A, Cheng AH-D. An Integral equation method for modelling three-dimensional heat extraction from a fracture in hot dry rock. *International Journal for Numerical and Analytical Methods in Geomechanics* 2003; **27**:989–1004.

[10] Cheng A-D, Ghassemi A, Detournay E. A two-dimensional solution for heat extraction from a fracture in hot dry rock. *International Journal for Numerical and Analytical Methods in Geomechanics* 2001; **25**:1327–1338.

[11] Kolditz O. Modelling flow and heat transfer in fractured rocks: Dimensional effect of matrix heat diffusion. *Geothermics*, 1995; **24**:421–437.

[12] Kolditz O, Clauser C. Numerical simulation of flow and heat transfer in fractured crystalline rocks: Application to the hot dry rock site in Rosemanowes (U.K.). *Geothermics* 1998; **27**:1–23.

[13] Kohl T, Evans KF, Hopkirk RJ, Ryback L. Coupled hydraulic, thermal, and mechanical considerations for the simulation of hot dry rock reservoirs. *Geothermics* 1995; **24**:345–359.

[14] Schon JH. Physical properties of rocks: fundamentals and principles of petro-physics. *Seismic Exploration*, vol. 18. Pergamon Press: Oxford, 1996.

[15] Cheng AH-D, Sidauruk P, Abousleiman Y. Approximate inversion of the Laplace transform. *Mathematica Journal* 1994; **4**(1):76–82.

[16] Stehfest H. Numerical inversion of Laplace transforms. *Communications of the ACM* 1970; **13**:47–49, 624.

[17] Nowacki W. *Thermoelasticity*. Pergamon Press: Oxford, New York, 1973.

[18] Carslaw HS, Jaeger JC. *Conduction of Heat in Solids*. Oxford University Press: New York, 1959.

[19] Petty S. Thermal stimulation of well 83-16. In *Creation of an Enhanced Geothermal System through Hydraulic and Thermal*, Rose PE *et al.* (eds). University of Utah Energy and Geoscience Institute, *Quarterly Report*, December 2002.

[20] Liggett JA, Liu PL-F. *The Boundary Integral Equation Methods for Porous Media Flow*. George Allen & Unwin: London, 1983.

[21] Ghassemi A, Zhang Q. A transient fictitious stress boundary element method for poro-thermoelastic media. *Journal of Engineering Analysis with Boundary Elements* 2004; **28**(11):1363–1373.

Paper VI

A 3-D Study of the Effects of Thermomechanical Loads on Fracture Slip in Enhanced Geothermal Reservoirs[1]

A. Ghassemi[a], S. Tarasovs[a] and A.H.-D. Cheng[b]

[a] *Department of Geology and Geological Engineering, University of North Dakota, Grand Forks, ND 58202, USA*
[b] *Department of Civil Engineering, University of Mississippi, University, MS 38677, USA*

Abstract

Heat extraction from enhanced geothermal systems (EGS) can greatly affect the behavior of joints and other discontinuities in the reservoir. Fracture permeability can change in response to fluid injection/extraction, rock cooling, variations of stress field, and mineral dissolution/precipitation. The reduction in effective stress caused by pore pressure increase can cause the slippage of discontinuities, thus inducing seismicity. Studies have shown that thermal stresses generated by cold water injection have a similar effect. In order to assess the influence of thermal stresses on fracture opening and slippage, a 3-D coupled heat extraction/thermal stress/elastic displacement discontinuity model is used in this study. The effects of each mechanism on fracture slip is estimated with particular reference to the Coso geothermal field. The results indicate that under typical field conditions, a substantial increase in fracture slip is observed when thermal stresses are taken into account. The temporal evolution of the thermal stresses suggests that the rock mass deformation will not cease upon stoppage of water injection, which can be a cause of delayed seismic activity.

[1] Revised and resubmitted to the International Journal of Rock Mechanics and Mining Sciences & Geomechanics Abstracts, September 2006.

Keywords: Coso geothermal field; Displacement discontinuity; Enhanced geothermal system; Fracture permeability; Fracture slip; Integral equation; Induced seismicity; Thermoelasticity.

1 Introduction

Hot subsurface rocks can be an economical source of renewable energy. The temperature in the subsurface can rise to 350°C at a depth of 5 km (at less than 3 km in the Coso Geothermal Field, central eastern California), and further to $500 - 1200$°C at 40 km. According to the United States Geological Survey (USGS) estimates, geothermal reservoirs at a depth of 3 km potentially can yield $100,000$ MWe for 30 years. The production of geothermal energy from these generally dry and low permeability reservoirs is achieved by water circulation in natural and/or man-made fractures, and is often referred to as enhanced or engineered geothermal systems (EGS). Two or more wells are drilled into the reservoir to intersect permeable fractures, and cold water is injected into one part of the well system and hot water/steam is recovered from the other (Fig. 1). The injection/extraction operation perturbs the in situ stress state in the reservoir, leading to fracture initiation and/or activation of discontinuities such as faults and joints. These events often manifest as microseismicity in the reservoir, which can be monitored. The information gathered can be used to interpret the geometry of the geological structures and the in situ stress state, and to predict stimulation outcome [1–3]. Slippage on preexisting discontinuities can enhance fracture permeability and thus is a positive outcome of fluid injection. To better understand these events, it is necessary to investigate the processes and mechanisms associated with fluid-induced changes in the reservoir to improve reservoir development and management [4].

It is generally believed that the stresses generated by poromechanical and thermal processes cause fracture opening and slip in EGS [5–7]. Poroelastic and thermoelastic effects on reservoir seismicity can be viewed from two related standpoints: (a) the impact on the reservoir's large scale, in situ stress state and (b) the influence on the local fracture and fracture zone behavior, with emphasis on fracture opening, slip, and/or propagation. Segall [8] and Rudnicki [9], among others, have considered the influence of poroelastic effects on reservoir seismicity, and have provided some quantitative and qualitative analyses of their importance on the state of stress and induced seismicity. Germanovich *et al.* [10] considered the influence of poroelastic-induced stress changes on fault slip in 2-D using semi-analytical solutions.

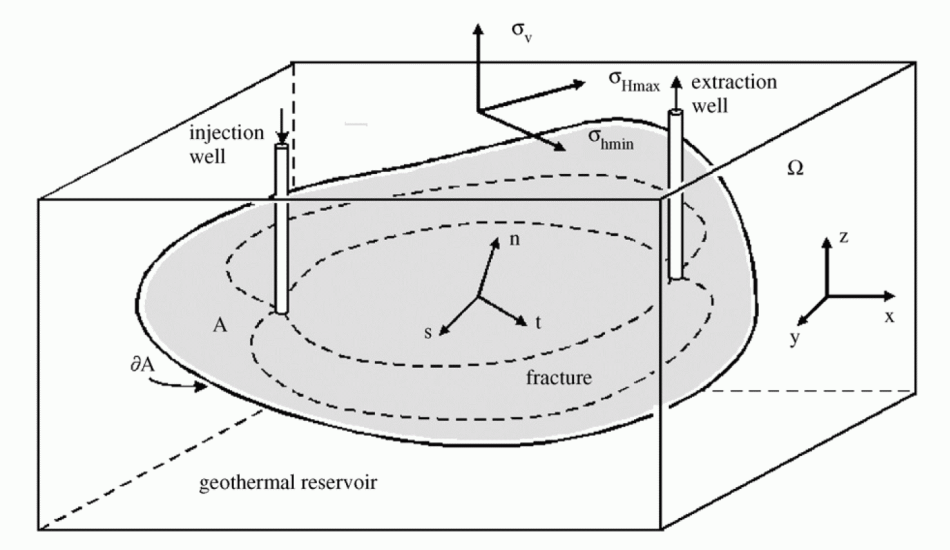

Figure 1: Heat extraction from a planar fracture. Also shown are the local fracture coordinates and the in situ stress orientation.

Segall and Fitzgerald [6] investigated both poro- and thermoelastic induced stresses and their impact on the reservoir, with the conclusion that thermoelastic stresses are more significant for geothermal reservoirs. Mossop [7] and Bruel [11] studied thermal stresses associated with injection and suggested that they could contribute to reservoir seismicity.

Poromechanical and thermomechanical processes can occur at different time scales, depending on the problem of interest and the formation properties involved. For example, the thermomechanical coupling is important during injection operations (time scale of months to years) [12,13]. It can be expected that changes in pore pressure may influence deformations on a discontinuity much more rapidly than temperature [5,14]. As a result, injectionrelated seismicity is often attributed to shear slip on natural fractures caused by a reduction of the normal stress across the fractures in response to an increase in the pore pressure field. It is, therefore, commonly suggested that microseismic activity is indicative of water flow and enhanced permeability. This is not necessarily the case though. As it has been pointed out, pore pressure increase does not necessarily correspond to the existence of flow [15,16]. Furthermore, injection pressure in geothermal reservoirs is often insufficient to open a fracture, pointing to the importance of ther-

mal stresses [7,11,17]. According to Stark [17], half the earthquakes in the Geysers geothermal field (northern California) appears to be related to cold water injection at less than critical injection pressures.

As the behavior of joints and other discontinuities plays an important role in heat extraction from EGS and reservoir seismicity, it would be beneficial to gain a better understanding of their response to various mechanisms related to cold water injection. Geomechanical models are particularly useful in this regard [18].

The study of thermal stresses, as well as its application to geomechanics, has a long history of development. Nowacki [19] provided a detailed exposition of theoretical and applied thermoelasticity and presents a broad array of solutions for stresses due to heat sources with many references going back to the early 1900s. He also showed detailed derivations of equations including Green functions for stresses associated with point heat sources. Thermoelasticity has been used to study inter- and intra-granular thermal cracking in certain igneous rocks [20]. Temperature, anisotropy and mismatch in grain thermal expansion coefficient, initial porosity, and grain size were found to control cracking. Also, experiments have shown that the presence of water enhances thermal cracking [20]. The importance of thermal stress to hydraulic fracture initiation and stress measurement was also investigated [21].

In the petroleum sector, the role of thermal stress in injection operations has been studied [22,23] with regard to the reduction of reservoir stresses and injection pressure, and fracture propagation. There have also been a number of early investigations of thermoelastic effects in geothermal systems and earth science [24–29]. Bodvarsson and Lowell [25], as well as Lister [28], discussed the interaction between thermoelastic effects and fluid circulation in the ocean floor. Bodvarsson [24] derived the stress field and surface deformation due to temperature changes in a geothermal system, and their impact on fracture aperture. A 1-D heat flow and elasticity model was used to calculate surface deformation of an infinite half-space, and the derived expressions were applied to calculate fracture opening/closure in response to non-isothermal flow. Lowell [29] applied the same approach to Black Smokers formation. Elsworth [30] used a 1-D heat transfer model to study the impact of thermal stress on fractured rock opening and permeability. Lowell *et al.* [31] coupled the 1-D model of Lowell [29] with a silica precipitation model and studied the permeability change in fractures in oceanic hydrothermal zones.Nygren and Ghassemi [32,33] and Nygren *et al.* [34] investigated the role of combined injection-induced thermoelastic and poroelastic stresses on joint slip, opening, and injection pressure, utilizing semi-analytical mod-

els of 1-D heat and fluid diffusion into the rock matrix. The 1-D approach to fracture opening in response to cooling has the shortcoming of predicting an unbounded fracture opening as time increases to infinity. Therefore, at least a 2- D elasticity is necessary to obtain a physically realistic long term behavior.

The heat extraction aspect of the problem has been numerically treated by many investigators [35–41]. The magnitudes of the 3-D thermal stresses associated with advective cooling for an axisymmetric model of injection into a planar reservoir have been obtained [7]. A coupled hydro-thermo-mechanical model has been developed by Kohl *et al.* [38] using the finite element method. Also, the problem of injection pressure variation in a fractured geothermal reservoir has been investigated [11,41,42] using a finite element model and a statistically generated fracture network. In those studies, the temperature field and the thermal stresses in the rock mass have been modeled using a 1-D approach. A 1-D heat transport model can underestimate the heat transfer from the rock to the fluid [35], and a 1-D treatment of the elasticity problem does not predict the correct distribution of thermal stresses. Rock cooling and the induced thermal stresses were previously studied using a 3-D heat flow model coupled with a 3-D thermoelasticity model [43].

In the present work, the 3-D heat extraction/thermal stress solution is coupled to a 3-D elastic stress/displacement analysis to obtain the opening and ride of a fracture under a given in situ stress field in response to cooling of the rock. The 3-D treatment is made possible by the use of Green's function to model not only the 3-D heat conduction, but also the 3-D thermal stress problem without the discretization of the reservoir. The fracture response is also modeled using a 3-D DD boundary element technique. The DD method is particularly suitable for studying faults and joints, and has been applied to fracture problems in plane strain [13,44], as well as in three dimensions [45–47].

It should be pointed out that Sekine and Mura [48] considered a penny-shaped crack in hot dry rock. Crack stability (i.e., condition of no change in radius or closure of the crack) with respect to mode 1 propagation in the presence of thermal stress was studied. A linear variation of temperature from the inlet to the outlet was assumed, resulting in a constant heat flux across the crack surfaces. It was found that the fracture toughness of the rock had little influence on the upper critical flow rate, and that the crack radius variation became more pronounced with larger inlet flow rates, indicating the impact of cooling. It should be emphasized that the above-cited work was based on a different conceptual model than the present study. It consid-

ered an injection fluid driven mode 1 (opening mode) fracture propagation based on the linear fracture mechanics criterion of stress-intensity-factor and fracture toughness. The focus of the present study is on fracture slip and induced seismicity during and after the injection operation. A 3-D model is used to study the contribution of thermal stresses to fracture slip. Both an infinite fracture and a finite irregularly shaped fracture are considered.

In the following, the 3-D fluid flow/heat extraction problem is briefly described, and then the 3-D DD formulation is presented. Following a concise exposition of the numerical procedures, application examples are provided to highlight the influence of thermomechanical processes on fracture slip and the potential seismicity.

2 Heat Conduction and Transport

Prior to dealing with the thermal stress and displacement analysis, the fluid flow and heat transport problem in the fracture and heat conduction in the reservoir need to be examined. The treatment of this problem, along with the assumptions and their justification, has been described in more detail in Ghassemi *et al.* [35,43]. Here, it is briefly presented for completeness and easy reference.

A schematic view of the heat extraction by circulating water in a natural or man-made fracture in rock is illustrated in Fig. 1. The fracture is assumed to be flat, of finite size, and of arbitrary shape. The geothermal reservoir is considered homogeneous, isotropic, and of infinite extent. Generally speaking, minerals are anisotropic both in elasticity and in thermal conductivity. However, it is reasonable to consider that a granite composed of a random distribution of these minerals to have isotropic properties [49]. On the other hand, the presence of cracks and other discontinuities with preferred orientation can cause the rock mass to become thermally and elastically inhomogeneous and anisotropic. However, in the absence of data regarding these properties under in situ conditions, the simpler homogeneity and isotropy assumptions are used in the present study.

Due to the computational difficulty associated with discretizing the 3-D reservoir geometry, in most studies the heat transport in the rock is considered in 1-D geometry perpendicular to the fracture surface [36,50,51]. There exist a few exceptions, however, such as the finite element solution by Kolditz [52], Kolditz and Clauser [39], and Kohl *et al.* [38], and the boundary element solution by Cheng *et al.* [53]. Particularly, in the boundary element solution [53], the difficulty in discretizing the 3-D, infinite reservoir

is circumvented by utilizing the integral equation formulation and the 3-D Green's function of heat conduction. Hence the 3-D problem is solved in a 2-D geometry [35].

In developing the model, a number of simplifying assumptions are made. Similarly to Cheng *et al.* [53], it is assumed that the geothermal reservoir is impermeable, hence the poromechanical effects are not considered in the present study. The reservoir has constant heat conduction properties. The heat storage effects i.e., is the transient heat storage in the fluid associated with $\partial T(x, y, 0, t)/\partial t$, and dispersion effects in the fracture fluid flow are negligible, as demonstrated in the early study [53]. It is further postulated that the flow, heat extraction, and elasticity problems are uncoupled. The flow in the fracture is considered to be laminar and governed by the lubrication flow equation; and the production rate of hot water is equal to the injection rate in the fracture. Although the single fracture geometry along with these simplifying assumptions represent an idealized system, such system can provide useful insight regarding the reservoir's thermomechanical response to cold water injection.

The heat transport occurs both in the geothermal reservoir and the fracture. For the geothermal reservoir rock, the heat conduction is governed by the 3-D diffusion equation [35] (see e.g., Nowacki [19] for a generic derivation):

$$K_r \nabla^2 T_d(x, y, z, t) = \rho_r c_r \frac{\partial T_d(x, y, z, t)}{\partial t}, \qquad x, y, z \in \Omega \tag{2}$$

where ρ_r is the rock density, c_r is the specific heat of rock, K_r is the rock thermal conductivity, Ω represents the infinite geothermal reservoir (Fig. 1), and T_d is the normalized temperature deficit with a value between zero and one:

$$T_d = \frac{T_0 - T}{T_0 - T_{inj}} \tag{3}$$

were T is the temperature, T_0 is the initial rock temperature, and T_{inj} is the temperature of injected water, both are assumed to be constant.

For heat transport in the fracture the governing equation is:

$$\mathbf{q}(x, y) \cdot \nabla T_d(x, y, 0, t) = \frac{2K_r}{\rho_w c_w} \left. \frac{\partial T_d(x, y, z, t)}{\partial z} \right|_{z=0^+} \tag{4}$$

where ρ_w is the water density, c_w is the specific heat of water, and

$$\mathbf{q}(x, y) = \int_0^{w(x,y)} \mathbf{v}(x, y, z)\, dz \tag{5}$$

is the discharge per unit width in the transverse direction of the flow, with $\mathbf{v}$ the flow velocity in the fracture and w the fracture width. The term on the left hand side of (4) represents the heat advection by fracture fluid flow, and the term on the right gives the heat supply through the fracture walls (two sides) by conduction. A single notation, $T_d(x, y, z, t)$, is used in (4) to denote the temperature of the rock and the fracture fluid. This is because the temperature is continuous across the two media. On the fracture plane ($z = 0$) the water temperature T_w equals the rock temperature i.e., $T_w(x, y, t) = T(x, y, 0, t)$, $x, y \in A$.

In arriving at (4), it has been assumed that the effects of heat dispersion due to a velocity gradient across the fracture and heat conduction in the fluid are negligible (advection dominant heat transport). The validity of these assumptions has been shown in Cheng *et al.* [53] and Nemat-Nasser and Ohtsubo [40].

These governing equations are subject to initial and boundary conditions. Prior to the heat extraction operation, the temperature of the rock and the fracture fluid is assumed to be a constant, $T(x, y, z, 0) = T_0$, and at the injection point $(x_i, y_i, 0)$, the temperature is equal to that of the injected water: $T(x_i, y_i, 0, t) = T_{inj}$. The extraction temperature $T(x_e, y_e, 0, t)$ is unknown. The initial and the boundary condition can be expressed in terms of T_d:

$$T_d(x, y, z, 0) = 0; \qquad T_d(x_i, y_i, 0, t) = 1 \tag{6}$$

Laplace transform is applied to the above equations to facilitate the treatment of the time variable:

$$K_r \nabla^2 \widetilde{T}_d(x, y, z, s) = s\rho_r c_r \widetilde{T}_d(x, y, z, s) \tag{7}$$

$$\mathbf{q}(x, y) \cdot \nabla \widetilde{T}_d(x, y, 0, s) = \frac{2K_r}{\rho_w c_w} \left. \frac{\partial \widetilde{T}_d(x, y, z, s)}{\partial z} \right|_{z=0^+} \tag{8}$$

$$\widetilde{T}_d(x_i, y_i, 0, s) = \frac{1}{s} \tag{9}$$

where the tilde overbar denotes the Laplace transform, and s is the transform parameter.

The system of equations (7)–(8) is defined in three spatial dimensions. It has been demonstrated that by utilizing Green's function of 3-D diffusion equation, the solution system can be reduced to a 2-D integral equation [35]. In this way, the temperature on the fracture surface ($z = 0$) can be

expressed as

$$\widetilde{T}_d(x,y,0,s) = -\frac{\rho_w c_w}{4\pi K_r}\int_A \left[\mathbf{q}(x',y')\cdot\nabla\widetilde{T}_d(x',y',0,s)\right] \frac{1}{r}\exp\left(-\sqrt{\frac{\rho_r c_r s}{K_r}}\,r\right)\,dx'\,dy'; \qquad x,y\in A \tag{10}$$

where $r=\sqrt{(x-x')^2+(y-y')^2}$. Equation (10) is entirely defined on the 2-D fracture plane A. Together with the boundary condition (9), it forms a complete solution system for fluid temperature in the fracture $\widetilde{T}_d(x,y,0,s)$. The solution of the system is in the Laplace transform domain. It is necessary to transform the solution back into the time domain. This is accomplished by solving the above system for a number of different values of s to produce data in the Laplace transform space. An approximate inversion method namely, the Stehfest method [54, 55], is chosen for this work. The numerical details of solving the integral equation (10) can be found in Ghassemi *et al.* [35], and are not repeated here.

3 Thermal Stress

The purpose of this paper to evaluate the mechanical response of the fracture to water injection and cooling of the rock. Thus, it is necessary to find the transient thermal stress induced by the temperature field obtained in the previous section.

For an isotropic, homogeneous, and elastic reservoir, the change in temperature $\Delta T=(T-T_o)$ can be related to the Goodier thermoelastic displacement potential Φ through the following Poisson equation:

$$\nabla^2\Phi = m\,\Delta T \tag{11}$$

where:

$$m=\frac{(1+\nu)\alpha_T}{(1-\nu)} \tag{12}$$

is the thermoelastic constant, α_T is the coefficient of linear thermal expansion, and ν is the Poisson ratio. Recall that the displacement field can be expressed as

$$\mathbf{u}=\nabla\Phi \tag{13}$$

where $\mathbf{u}$ is the displacement vector. Expression of displacement in terms of a potential is possible because thermally generated displacement field is irrotational.

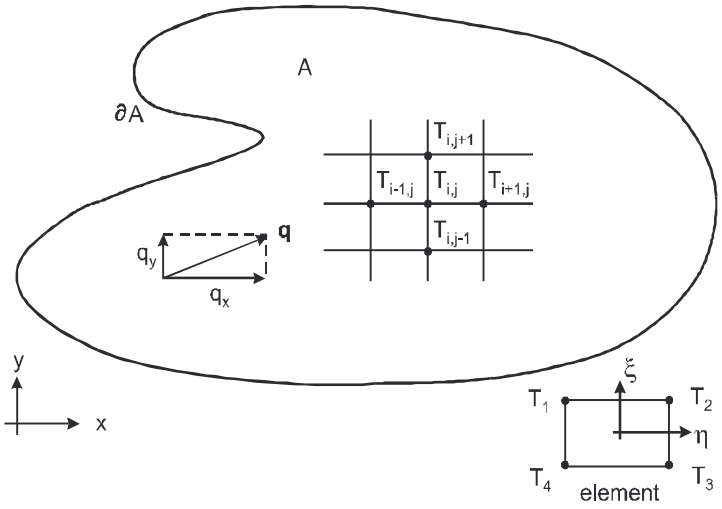

Figure 2: Computational mesh on the fracture plane showing element geometry, and nodal distribution where temperature, stress, and slip are calculated. The flow components q_x and q_y are also shown.

Given a distribution of temperature at any given time, the potential Φ can be calculated from the Poisson integral [19]:

$$\Phi(x,y,z,t) = -\frac{m}{4\pi}\int_{\Omega}\frac{\Delta T(x',y',z',t)}{R}\,dx'\,dy'\,dz' \tag{14}$$

where $R=\sqrt{(x-x')^2+(y-y')^2+(z-z')^2}$. Equation (14) can be directly evaluated to obtain the potential and the thermal stresses, but it is inefficient to integrate as the integration is in three dimensions over an infinite domain. The problem can be reduced to 2-D by using Green's function of 3-D diffusion in the Laplace domain as shown in Ghassemi *et al.* [43]:

$$\begin{aligned}\widetilde{\Phi}(x,y,z,s) &= \frac{m\,\rho_w\,c_w}{4\pi s\rho_r c_r}\int_A\Big[\mathbf{q}(x',y')\cdot\nabla\widetilde{T}(x',y',0,s)\Big] \\ &\quad\Big[\frac{1}{R}-\frac{1}{R}\exp\left(-\sqrt{\frac{s}{\kappa}}R\right)\Big]\,dx'\,dy'\end{aligned} \tag{15}$$

The right hand side of the above equation consists entirely of known quantities, because the fluid flow and the temperature in the fracture have been obtained from the previous stage of solution based on (10). In fact, the same grid system as shown schematically in Fig. 2 can be used in the evaluation.

So, the problem of finding thermal stresses induced by the injection of cooling fluid is reduced to integration on only the fracture surface. To obtain the displacement potential on the fracture surface, Eq. (15) is evaluated at $z = 0$:

$$\widetilde{\Phi}(x,y,0,s) = \frac{m\,\rho_w\,c_w}{4\pi s\rho_r c_r}\int_A \left[\mathbf{q}(x',y')\cdot\nabla\widetilde{T}(x',y',0,s)\right] \left[\frac{1}{r}-\frac{1}{r}\exp\left(-\sqrt{\frac{s}{\kappa}}r\right)\right]\,dx'\,dy' \tag{16}$$

The stresses are related to the displacement potential by the following formula [19]:

$$\widetilde{\sigma}_{ij} = 2G\left(\frac{\partial^2\widetilde{\Phi}}{\partial x_i\partial x_j}-\delta_{ij}\nabla^2\widetilde{\Phi}\right) \tag{17}$$

where δ_{ij} is the Kronecker delta. The stresses are evaluated using a finite difference approximation of (17).

4 Displacement discontinuity

As mentioned above, fracture permeability and reservoir seismicity are related to slip along preexisting discontinuities. Useful information can be obtained by studying the response of fracture to fluid pressure and rock cooling under a given state of stress. In this work, the fracture opening and slip are determined using a 3-D elastic DD method. The DD method is an indirect boundary element method which is based on the fundamental solution of a point DD in an infinite elastic or poroelastic medium. This technique has been used extensively in mining and hydraulic fracturing [44,45,47]. The most extensive developments are due to Crouch and Starfield [44] who used the solution of a constant line displacement discontinuity in an infinite elastic medium as the singular solution. Other investigators [56] use the 2-D and 3-D point DD as the fundamental solution. This solution is then integrated over a desired element shape to form the building block of the DD method. Then, a fracture is modeled by dividing its surface into a number of DD elements and requiring that the superposition of their effects satisfies the prescribed boundary conditions.

The tractions on the fracture surface (A) due to displacement discontinuities can be written in form of integral equation of the first kind:

$$\sigma_{ij}(\mathbf{x}) = \int_A \sigma^*_{ijkn}(\mathbf{x}',\mathbf{x})\;\Delta D_{kn}(\mathbf{x}')\;d\mathbf{x}' \tag{18}$$

with known values of σ_{ij} and unknown values of DD tensor, ΔD_{kn}. The kernel σ^*_{ijkn} represents the effect of a point DD at point $\mathbf{x}'(=(x',y',z'))$ on the stresses at point $\mathbf{x}(=(x,y,z))$. A general analytical solution of this equation is not possible, therefore it is necessary to solve it numerically by transforming the integral equation into a system of algebraic equations. The fracture surface is divided into number of elements. The induced stresses on element "m" due to a constant spatial distribution of normal and shear DD's on element "r" are given by

$$\sigma^m_{ij}(\mathbf{x}) = S^{rm}_{ijkn}(\mathbf{x}',\mathbf{x})\Delta D^r_{kn}(\mathbf{x}') \tag{19}$$

where ΔD_{kn} are the strength of the components of the DD tensor. The superscripts m and r refer to the influenced and the influencing elements, respectively. The quantities with those superscripts are in the local coordinate system of the influenced and influencing elements, respectively. The coefficients relating the DDs on the influencing elements (with surface S_r) to the stresses on the influenced elements are given by:

$$S^{rm}_{ijkn}(\mathbf{x}',\mathbf{x}) = a_{il}a_{jm}\int_{s_r}\sigma^*_{lmkn}(\mathbf{x}',\mathbf{x})d\mathbf{x}' \tag{20}$$

where a_{il} is the rotation matrix from the influencing to the influenced coordinate system. The spatial integration is a relatively easy process for constant elements in 3-D problems. Superposition of influences of all elements to element m gives a system of algebraic equations:

$$\sigma^m_{ij}(\mathbf{x}) = \sum_{r=1}^{N} S^{rm}_{ijkn}(\mathbf{x}',\mathbf{x})\Delta D^r_{kn}(\mathbf{x}'),\quad m=1,N \tag{21}$$

It should be noted that the stresses on the left hand side include both in-situ field stresses and those induced by the injection/extraction problem which is solved separately for a given time as described before. σ^*_{ijkn} represent the 3-D fundamental solutions for stresses σ_{ij} due to a point shear $(k \neq n)$ and normal $(k = n)$ displacement discontinuities at point $\mathbf{x}'$ in an infinite elastic medium. It is given as follows [47]:

$$\begin{aligned}\sigma^*_{lmkn} \;=\; & -\frac{G}{4\pi(1-\nu)R^3}\left[(1-2\nu)\left(\delta_{ik}\delta_{jn}+\delta_{jk}\delta_{in}\right)\right. \\ & -(1-4\nu)\,\delta_{ij}\delta_{kn}+3\,(1-2\nu)\left(\delta_{kn}R_{,i}R_{,j}+\delta_{ij}R_{,k}R_{,n}\right) \\ & -15R_{,i}R_{,j}R_{,k}R_{,n}+3\nu\left(\delta_{ik}R_{,j}R_{,n}+\delta_{jk}R_{\,,i}R_{,n}\right. \\ & \left.\left.+\;\delta_{in}R_{,j}R_{,k}+\delta_{jn}R_{\,,i}R_{,k}\right)\right]\end{aligned} \tag{22}$$

where $R_{,i} = \partial R/\partial x_i = (x_i - x_i')/R,\ i = 1, 2, 3$, and δ_{ij} is the Kronecker delta. For a distribution of point DD's on a given plane the above equations can be multiplied by a desired shape function and integrated with respect to $\mathbf{x}'$ to yield the stresses and displacements due to a given distribution of DD. For example, for a constant (unit) variation of normal DD ($k = n = z$) over a rectangle ($2a \times 2b$) the above procedure gives the expressions from which the influence coefficients may be calculated at any point. For example, σ_{zz} in the DD element coordinate system is given by [44]

$$\begin{aligned}\sigma_{zz} \quad = \quad & -\frac{G}{4\pi(1-\nu)}\left[\left[\frac{XY(r^2+Z^2)}{r(r^2Z^2+X^2Y^2)} - \frac{XYZ^2(X^2+Z^2+2r^2)}{R(X^2+Z^2)^2}\right.\right. \\ & \left.\left. - \frac{XYZ^2(Y^2+Z^2+2r^2)}{R(Y^2+Z^2)^2}\right]_{-a}^{a}\right]_{-b}^{b} \end{aligned} \tag{23}$$

where $r = \sqrt{X^2+Y^2},\ X = x - x',\ Y = y - y'$, and $Z = z$. It should be noted that shear stresses depend on both shear components of DD while the normal stress components depend only upon the normal component of DD. When the value of Z is set to zero, meaning that it is on the fracture plane, the above equation gives the normal traction component on the crack plane as

$$(\sigma_{zz})_{Z=0} = -\frac{G}{4\pi(1-\nu)}\left[\left[\frac{\sqrt{X^2+Y^2}}{XY}\right]_{-a}^{a}\right]_{-b}^{b} \tag{24}$$

The above expression is the stress component due to a constant DD over a rectangle. Similar expressions can be obtained for other components of stresses and displacements, and for different type of elements, such as triangular element.

5 Fracture Opening and Slip

As indicated before, for a planar fracture, shear stresses depend on both shear components of DD; while the normal stress components depend only upon the normal component of DD. Thus, the σ_{zz} stress component for the elements are independent of σ_{xz} and σ_{yz}; and can be solved separately. Applying Eq. (19) for normal and shear stress components and summing the influence coefficients over all elements, two systems of algebraic equations are formed for N closure and $2N$ ride unknowns:

$$\sigma_{zz} = K_{zz} D_{zz} \tag{25}$$

$$\begin{bmatrix} \sigma_{xz} \\ \sigma_{yz} \end{bmatrix} = \begin{bmatrix} K_{xx} & K_{xy} \\ K_{yx} & K_{yy} \end{bmatrix} \begin{bmatrix} D_{xz} \\ D_{yz} \end{bmatrix} \tag{26}$$

where K is the matrix of influence coefficients; K_{zz} represents the normal stresses due to normal DD's (in the z-direction), K_{xy} represents the shear stress in the x-direction due to shear DD's in the y-direction, and so on.

When the fracture remains open, these equations can be solved in a simple manner. In that case, the slip corresponds to the magnitude of shear displacement discontinuities. However, a different approach is needed when the fracture is closed. In this case, the fracture is modeled using a rigid perfectly plastic Mohr-Coulomb element. The shear strength of the Mohr-Coulomb element is given by

$$\tau = c_0 + \sigma_n \tan \phi_{ef} = c_0 + \sigma_n \tan(\phi_{in} + \varphi_{dil}) \tag{27}$$

where ϕ_{ef} is the effective friction angle of the joint/fault surface, ϕ_{in} is intrinsic friction angle, φ_{dil} is dilation angle, σ_n is the compressive stress acting on the fracture surface and c_0 is the cohesion. The standard Coulomb friction model assumes that no relative motion occurs if the equivalent shear stress

$$\tau_{eq} = \sqrt{\sigma_{xz}^2 + \sigma_{yz}^2} \tag{28}$$

is less than the critical stress, predicted by Eq. (27).

The fracture aperture is affected by the amount of shear displacement and is equal to

$$a = \sqrt{D_{xz}^2 + D_{yz}^2} \tan(\varphi_{dil}). \tag{29}$$

This is a simple joint dilation model; however, other and perhaps more complex dilation models [41] can be implemented in the solution procedure without restrictions.

To set up the system of equations for a given problem, the in situ stresses and hydraulic pressure are applied in the initial solution step. If the fracture aperture at a node associated with a fracture element is found to be negative (overlap), penalty stresses are applied to the overlapping portion of the fracture surface. The applied penalty stresses are proportional to the normal DD. Then, an iterative solution process is used until the fracture aperture becomes non-negative at any point.

During the course of the analysis, each element can be either in a state of "separation", "stick" or "slip". Separation elements do not require any additional treatment. Elements in the stick state have a fixed tangential DD during the current solution step. Elements in the slip state are allowed to slide in the tangential direction. After slip occurs, the excess shear stresses

are released in this zone and slipping elements may change their status back to stick state, but in the new deformed position (sometimes this approach is referred as "partial slip mode"). Such an element may remain in the stick mode for the rest of the analysis, or it might revert back to the slip mode due to an increase of shear stresses or a decrease of the normal compressive stresses. Therefore, each element can change its status several times during the course of the analysis. With an increase in the shear stresses or a decrease in the normal compressive stresses due to, e.g., thermally induced stresses, the slip increases with time.

The thermal stress is applied incrementally by increasing the load from zero to the calculated thermally induced stresses for a given time. Currently, a linear variation of thermal stresses (from zero until the given stress at a given time) is used. The new contact stresses are found for each load increment and the slip criterion is applied. Note that for the problem of a single injection well, the cooled zone (as well as thermal stresses) grows monotonically with time, therefore, approximating the increase in load using a linear variation is a good approximation, which provides good accuracy. However, for more complex situations with several injection wells or with several fractures, the time variation of the thermal load might become more complex, and more accurate description of the temporal variation of loads would be required. Doing so for the current problems would mean increased computational effort with negligible improvement in the results; hence it is not pursued.

The process of determining the magnitude of shear slip begins by initially setting the shear DD (ride) to zero or to a value that corresponds to the plastic deformation obtained from a previous solution step. By fixing these DD's and applying an increment of thermal stresses, the new shear stresses that act on the fracture plane are calculated. These stresses are then used in the MC slip (27). If shear slip is predicted, the value of friction forces is set to that given by Eq. (27), and the new slip value is calculated. Using these shear slip values, new shear stresses are calculated and the process continues until convergence for each loading step is achieved. Although fracture opening and compressive forces are updated after each iteration, the slip amount is assumed to be small enough so that the change in contact surface due to slip can be neglected. This means that element overlap due to slip is negligible and the upper part of the fracture is always in contact with the same element from the lower part, so that the change in element positions are neglected when calculating new influence functions. This is justified in view of the fact that slip values are of the order of a few mm and the element sizes are of the order of several meters. The solution algorithm

is as follows:

1. apply a new load increment m, and calculate the total load for the current increment:

$$\sigma_{ij} = \sigma_{ij}^{in-situ} + p^{hydr} * \delta_{ij} + \tau_{ij}^{friction} + \sigma_{ij}^{thermal} * \frac{m}{N} \qquad (30)$$

   which is the sum of in-situ stresses, hydraulic pressure, friction forces, and thermally induced stresses, respectively. The total number of load increments is denoted by N.

2. solve the system of equations (25) for D_{zz}. If any of the calculated D_{zz} is negative (overlap), apply penalty stresses (contact stresses on overlapped portion of fracture) to these elements, and solve for new D_{zz}. Adjust contact stresses until all D_{zz} values are non-negative;

3. apply the MC slip (27) for all elements using the compressive contact stresses acting on them calculated in step 2. If slip is predicted, then set friction forces:

   3.a for stick elements the friction forces are equal to the shear stresses in magnitude and opposite in direction; for slip elements the magnitude of friction forces is governed by Mohr–Coulomb criterion;

   3.b for elements for which slip was predicted (the shear DD's for non-slip elements remain fixed during this step) solve the system of equations (26) for shear;

   3.c after slip occurs, recalculate shear forces acting on the fracture plane for all elements using (26) and taking into account the new shear DD values;

   3.d calculate fracture aperture using (29);

   3.e go to step 2 and repeat until convergence is achieved;

4. apply another load increment and go to step 1, or stop in the case of last load step.

6 Numerical Examples

6.1 Injection into Infinite Fracture

E	Young's modulus	65.0	GPa
ν	Poisson's ratio	0.185	
ρ_r	rock density	2650	kg/m^3
ρ_w	water density	1000	kg/m^3
c_r	rock heat capacity	790	J/(kg K)
c_w	water heat capacity	4200	J/(kg K)
κ	thermal diffusivity	5.1×10^{-6}	m^2/ sec
α_T	rock linear thermal expansion coefficient	8.0×10^{-6}	1/K
Q	injection rate	40	ℓ/ sec
T_R	rock temperature	180	°C
T_{inj}	injection water temperature	30	°C
w	initial average fracture aperture for flow	10^{-3}	m

Table 1: Input parameter for infinite fracture problem.

A computer program is developed based on the above procedures. As a first example, we consider the problem of injection into an infinite planar fracture with the injection well located at the origin (e.g., Fig. 3). The fracture is considered to be at a depth of 2330m with an in situ stress of $\sigma_v = 60.13$ MPa, $\sigma_{h\,\min} = 34.81$ MPa, $\sigma_{H\,\max} = 50.88$ MPa, and a pore pressure of $P = 17.4$ MPa. The orientation of $\sigma_{H\,\max}$ is parallel to the fracture strike direction which is due north in the field (parallel to the local x-axis). This stress field can be rotated to the local fracture coordinate system to obtain $\sigma_{zz} = 41.1$ MPa, $\sigma_{xz} = 0$ MPa, and $\sigma_{yz} = 11.0$ MPa. The fracture surface has a dip angle of 60°, and it is assumed to have friction angle of $\phi = 30°$ and a dilation angle of 3°. The initial reservoir rock temperature is a constant $T = T_0$. At $t = 0^+$, water is injected at temperature T_{inj} with flow rate Q assumed to be 25 l/s. Other data for this problem are shown in Table 1. In the solid displacement analysis, the pressure in the fracture is assumed to be uncoupled to the pressure field that would be needed to drive the advective cooling fluid. It is set to a constant and equal to 20 MPa, i.e., slightly larger than the in situ pore pressure. Fluid flow analysis shows that this is a good assumption as the injection-induced pressure for the conditions considered is rather small (less than a few MPa) [33,34].

The mesh pattern used for the heat transport and thermal stress calculations in [43] (Fig. 2) is adopted for the numerical solution of the fracture response. Although the fracture is of infinite horizontal extent, the mesh covers only a finite region whose size is estimated such that the thermal perturbation is contained within it. For the current simulations, square el-

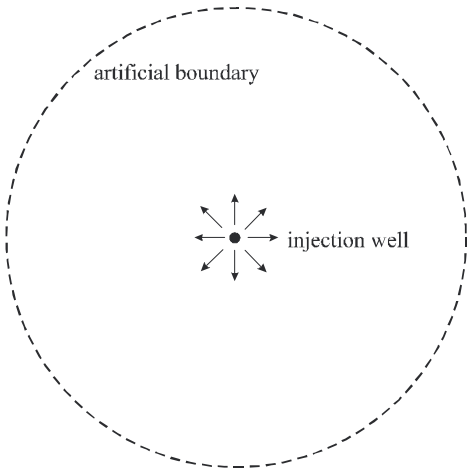

Figure 3: An infinite fracture with an injection well (plan view in the z-direction).

ements of size 4.25 m are used. An 80×80 mesh was selected based on error convergence, although a 60×60 mesh also provides satisfactory results. The same mesh is used for the fracture opening and slip calculations. The sensitivity of the results to element size and the suitability of the type and number of elements used have been discussed elsewhere [43,45]. The numerical results in terms of the cooling induced stresses are presented in Fig. 4 for one month of injection. The accuracy of the solution has been previously established [43], the solution compares very well with the semi-analytical solution by Mossop [7] for the problem of injection into a fracture of infinite extent. The error is localized around the injection well where a flow singularity exists. It is noticed in Fig. 4 that all three cooling-induced stress components shown have significant magnitudes. The induced thermal stresses near the injection well are tensile (meaning an reduction from the in situ compressive stress). The largest values occur near the well where the rock is cooled the most. Away from the well, the stresses decrease and σ_{zz} and σ_{yy} components eventually become compressive. This is the result of strain compatibility requirement in thermoelasticity—as rock contracts near the injection well due to cooling, it tends to pull on the exterior rock material inducing a compressive stress ahead of it. This transition from tension to compression would also be observed in a 2-D version of the thermoelastic problem. A 1-D formulation, on the other hand, would not capture it.

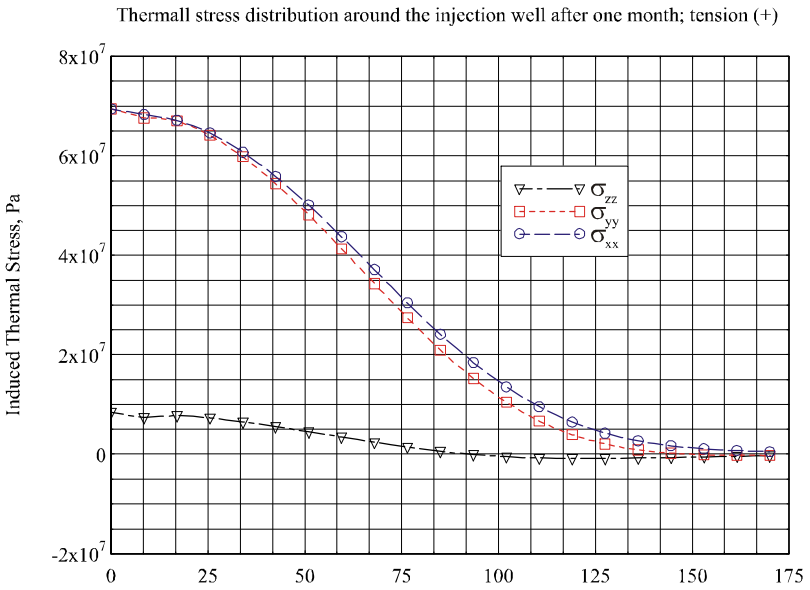

Figure 4: Thermally-induced stress distribution on a fracture surface around an injection well.

Near the injection zone, the values of induced σ_{yy} and σ_{xx} in Fig. 4 are an order of magnitude larger than σ_{zz}. These large stresses would cause new fractures to initiate and to open perpendicular to the original one. This possibility also has been suggested by other investigators [40]. Although their propagation and impact on the heat and fluid flow is beyond the scope of the current paper, their formation will have a microseismic signature that can be used in monitoring reservoir stimulation [57]. Similarly to the axial stress component, the σ_{yy} component also changes sign and becomes compressive away from the injection point. These compressive stresses can also contribute to slip on preexisting critically stressed cracks and potentially contribute to seismicity.

For the current problem, the σ_{zz} thermal stress component increases the fracture aperture through slip caused by a reduction in the effective normal stress. This is illustrated in Figs. 5 and 6 where we plot D_{yz} and D_{xz}, that is, the shear displacement in the local fracture coordinates directions y and x, respectively. The zone of slip and opening (light shade) is nearly circular and extends to about 50 m. The slight ellipticity in the distribution of slip is a result of the stronger σ_{yz} shear stress component forcing the slip zone to

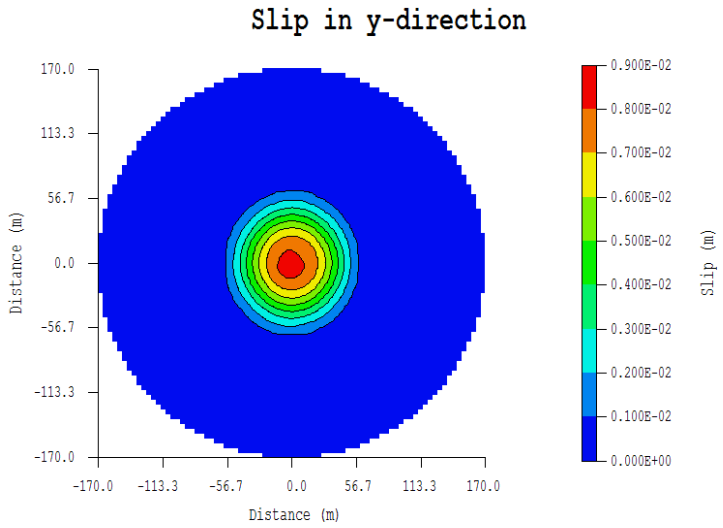

Figure 5: Distribution of D_{yz} displacement component on the infinite fracture.

grow more in the y-direction than in the x-direction. This is to be expected as the shear stress is also large in the y-direction, and the resolution of the field stresses yields a zero shear stress in the x-direction. The maximum slip in the y-direction occurs at the well and equals 9 mm. This shear slip causes some movement on the fracture in the x-direction with a maximum value of 0.16 mm. This small slip in the x-direction is entirely due to the slip in the y-direction that is caused by the in situ σ_{yz} stress component (see Eq. (26)) and the cooling-indued reduction of σ_{zz}. The distribution of the fracture opening is shown in Fig. 7, with the maximum opening of 0.45 mm. It is worth noting that the thermally induced shear stress components $\sigma_{xz} = \sigma_{yz} = 0$; while σ_{xy} is non-zero and small, but it does not contribute to shear slip on the fracture plane. The shear slip on the fracture plane can potentially manifest itself seismically. Furthermore, the cooling front and the stress perturbations (e.g., σ_{zz} in Fig. 8) will move into the rock mass, causing stress redistribution and possibly contributing to seismicity depending on factors such as coupled poro-thermoelastic mechanisms and rock mass fracture properties.

It is worth noting that for a constant injection rate, the injection pressure

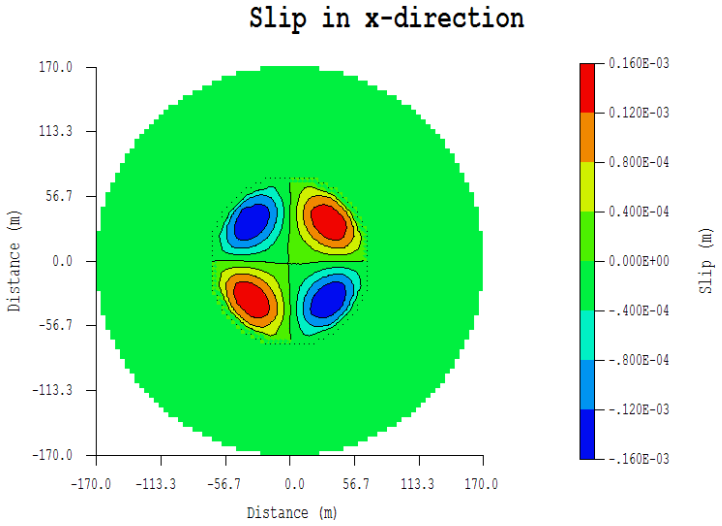

Figure 6: Distribution of D_{xz} displacement component on the infinite fracture.

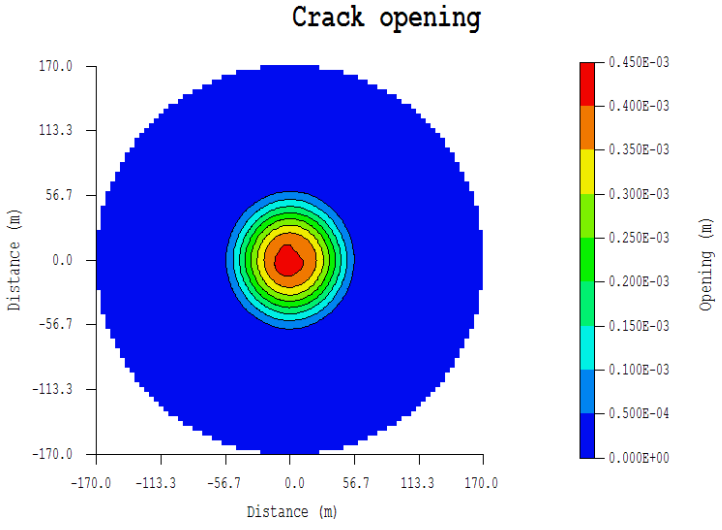

Figure 7: Fracture opening distribution for injection into an infinite fracture.

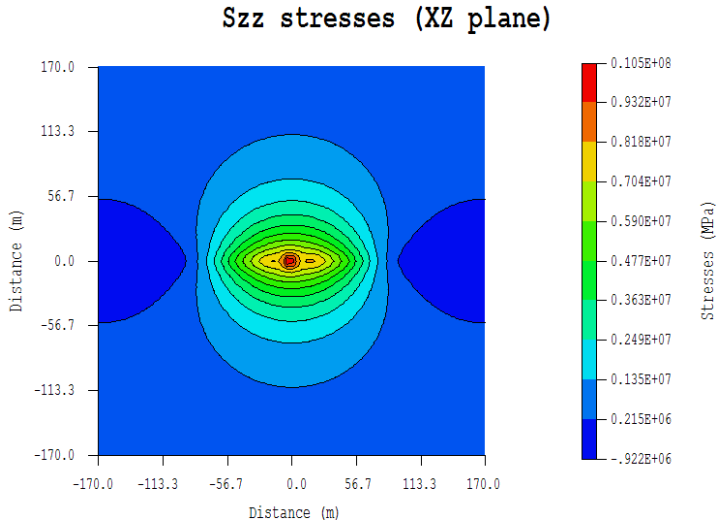

Figure 8: Distribution of cooling-induced σ_{zz} stress component in the rock after one month of injection.

will drop due to the increased fracture conductivity [23,32,33]. This is indeed observed in the injection experiment conducted in Well 83-16 of the Coso Geothermal Field [12]. This thermal stress induced aperture change will have an effect on the flow pattern, which in turn affects the heat transport. This coupled effect is not contained in the current model. However, if the injection is controlled by a constant flow rate, not by pressure, and the flow pattern remains radial, as is approximately the case here, then only the injection pressure will change without affecting the heat transport pattern so that the prediction of heat extraction is correct in spite of the thermal stress induced aperture change.

6.2 Injection/extraction in a Finite Fracture

The numerical procedures can also be applied to an injection/extraction operation involving an irregularly shaped fracture is shown in Fig. 9. The fracture is assumed to have an initial aperture of 1 mm under the action of the in situ stresses and pore pressure, due to existence of asperities or proppant. The fluid pressure in the fracture is assumed to be uniform and equal to 25 MPa, this applied fluid pressure by itself is insufficient to further

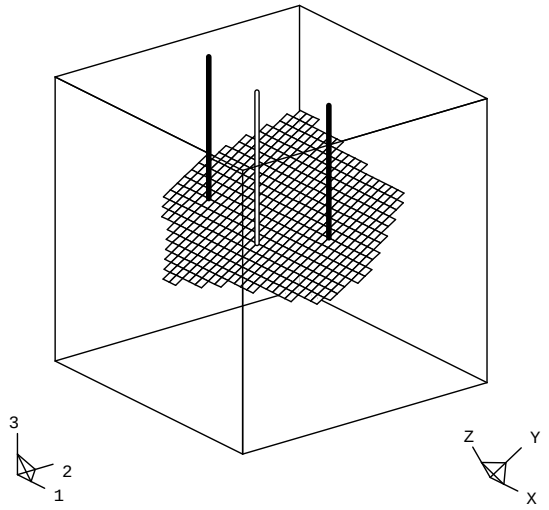

Figure 9: Injection/extraction operation in a fracture with arbitrary shape and orientation.

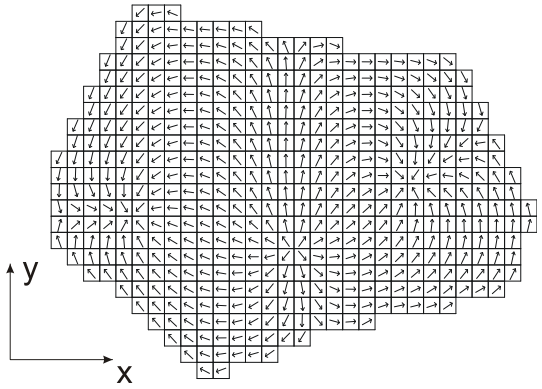

Figure 10: A fracture with irregular geometry; the computational mesh and fluid flow field for one injection well and two extraction wells (XY is the local fracture coordinate system).

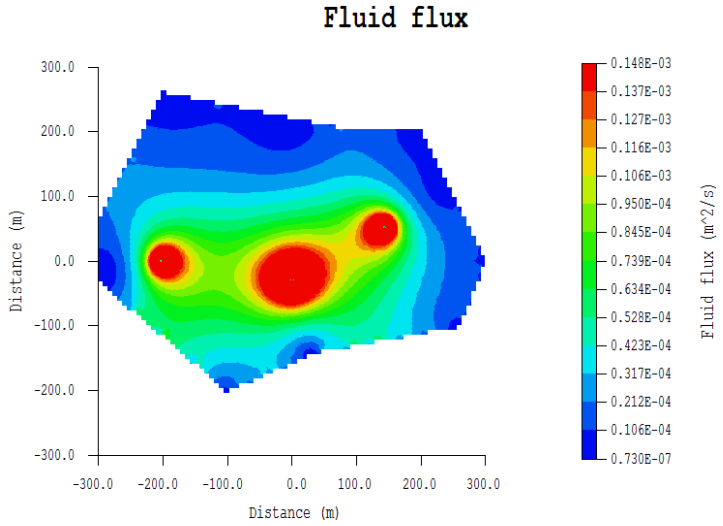

Figure 11: Flow magnitude in the fracture with one injection well and two extraction wells.

open the fracture. To calculate the actual flow field for the arbitrary shape fracture, the equation for the incompressible fluid flow is used [43]. For the current conditions, the resultant flow field and flow magnitude are shown in Figs. 10 and 11, respectively. The fracture surface is divided into 3384 elements. The heat extraction operation involves three wells: one injection well with flow rate 40 l/s, and two extraction wells each with flow rate 20 l/s. The rock and fluid properties are given in Table 1. The injection period is considered to be three months and the fracture orientation and in situ stress are the same as in the previous example.

The temperature distributions on the fracture surface after 3 months of operation are shown in Fig. 12. The small white region (about 30°C) around the injection well (see Fig. 9 for injection well location) indicates that heat depletion has not reached a large part of the reservoir at that time. Fig. 13 plots the net normal stress (contact) on the fracture surface after three months of injection. A large tensile region is developed around the injection well. This can be understood by noting that the compressive stresses are much reduced in that region (light shade). Zones of higher compressive stress (dark shade) are developed outside of the cooled area within

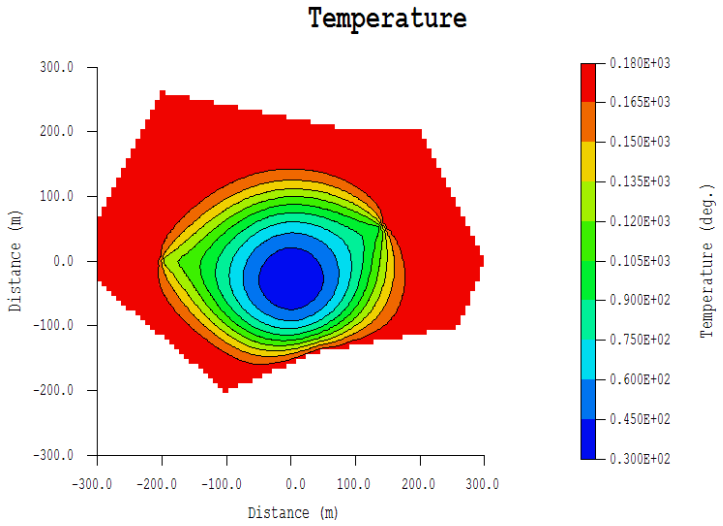

Figure 12: Temperature distribution in the fracture after 3 months of operation.

the fracture, which is consistent with the preceding case of a single injection well. Compression zones are also developed just behind the extraction wells. As noted before, these zones of increased compression can also contribute to slip of other fractures and induce seismicity. As before, there is some error at and near the injection/extraction wells, where a flow singularity exists. The fracture is assumed to have an initial aperture (10^{-3}), however, as can be seen in Fig. 14, after three months of injection the fracture aperture has increased in response to the fluid pressure, thermal stresses, and dilation with its maximum value of 4 mm at the injection well. The shear slip in the y- and x-direction is shown in Figs. 15 and 16, respectively. The fracture has undergone slip over a large area and we again note that the slip magnitude in the y-direction is dominant with a maximum value of 7 cm. Fig. 17 shows the slip in the y-direction when thermal stresses are not included in the analysis. It can be observed that the slip magnitude has decreased substantially. The maximum slip is now 9 mm. This is an explicit indication of the importance of thermal stresses in fracture slip which had previously been suggested as a potential contributor to seismicity in geothermal reservoirs [7]. In fact, the contribution of the hydraulic pressure will disappear once in-

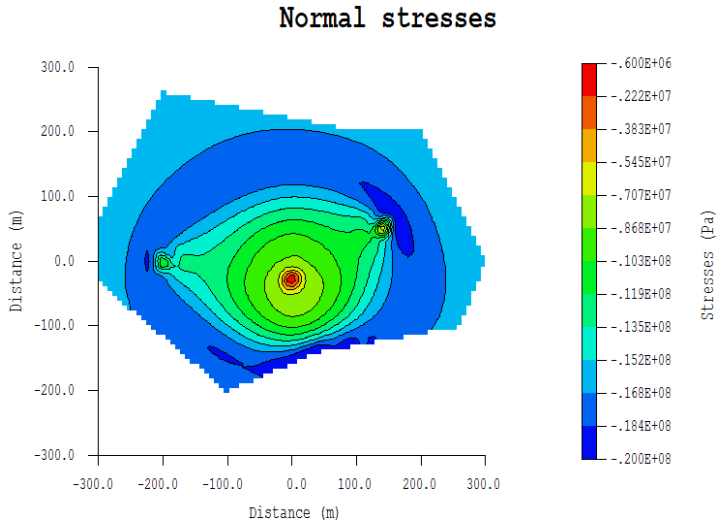

Figure 13: Normal stresses acting on the fracture plane after applying the in-situ stresses, pressure, and thermal stresses.

jection has ceased. But, the cooling front and the stress perturbations (e.g., σ_{zz} in Fig. 8) will continue to move into the rock mass, causing stress redistribution and possibly contributing to seismicity. A conclusive statement would require a more extensive modeling efforts as the stress redistribution is a function of many factors including porothermoelastic mechanisms and rock mass fracture properties that we have not included in our analysis.

7 Summary and Conclusions

A 3-D boundary element model for heat extraction/thermal stress has been coupled with a 3-D elastic DD method to investigate the fracture opening and slip in response to fluid injection pressure and cooling of the rock under a given in situ stress field. Using this approach, the effects of each mechanism on rock stress and fracture slip have been estimated. It has been found that not only tensile stresses develop due to the cooling, but also compressive stresses are generated in the range just outside the fracture or the fluid front, consistent with strain compatibility. We note that this mechanism is similar to the poroelastic effect used by Segall [8] to explain earthquakes triggered

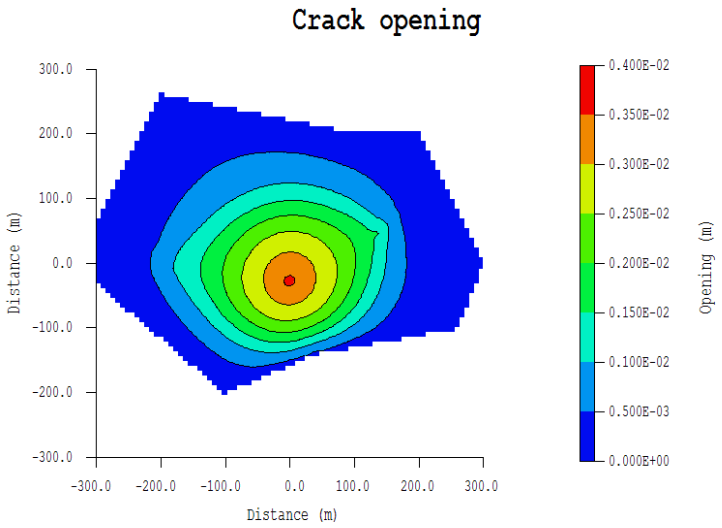

Figure 14: Crack opening after 3 months of injection (maximum opening is 4 mm).

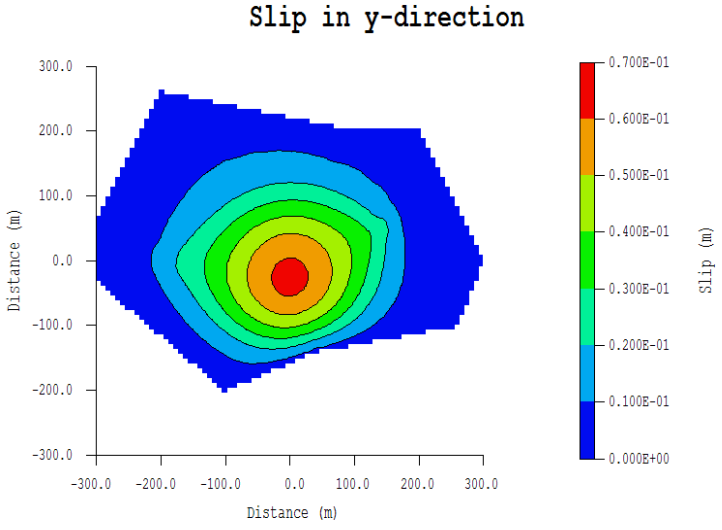

Figure 15: Slip in the y-direction (maximal slip values is about 7 cm).

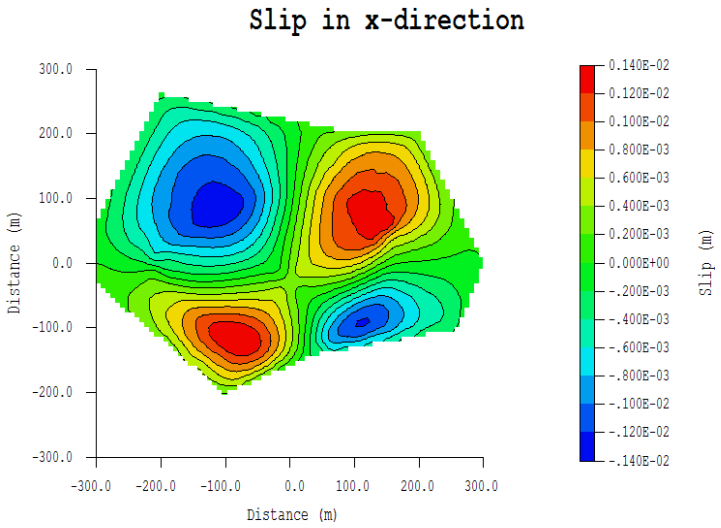

Figure 16: Slip in the x-direction (slip in this direction is very small, because the in-situ $\sigma_{xz} = 0$ on this plane).

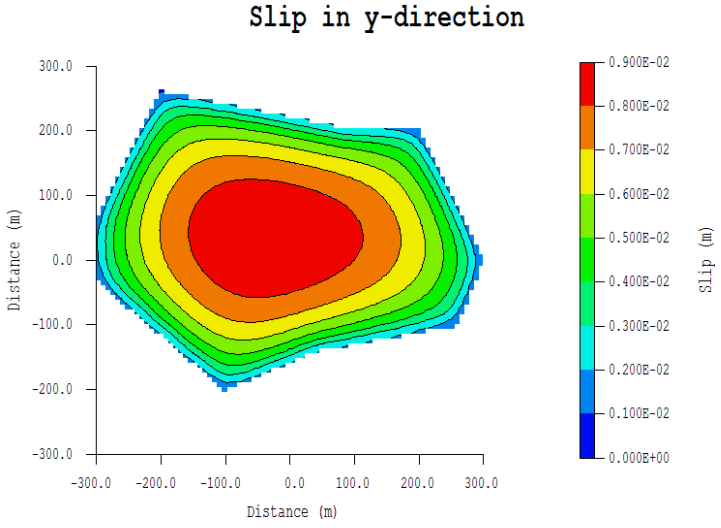

Figure 17: Shear slip in the y-direction in the absence of thermal stresses.

on the flanks of petroleum reservoirs due to fluid extraction. The results of displacement analysis indicate that under typical field conditions in Coso (in situ stress, pore pressure, rock/injection temperature, injection rate and duration), a substantial increase in fracture slip is observed when thermal stresses are taken into account. The amount of slip would depend on the rock joint properties, in situ stress, pressure, injection rate, and degree of cooling. For conditions similar to the Coso geothermal field, the predicted slip is of the order of several centimeter for a few months of injection/extraction. This slip can be accompanied by seismicity; it would also result in redistribution of stresses in the rock mass and may induce slip and seismicity elsewhere in the reservoir. The temporal distribution of the thermal stresses also suggests that their contribution to rock mass deformation will not stop upon cessation of water injection and can be a factor in delayed seismic activity. A more extensive modeling and analysis of the stress redistribution including porothermoelastic mechanisms for a given rock mass fracture properties would be necessary to assess the type and spatiotemporal extent of the events.

This work can be distinguished from other analytical and numerical studies that treat the heat conduction in the geothermal reservoir as 1-D and perpendicular to the fracture. For the few numerical works that treats 3-D heat flow and thermal stresses, the 3-D infinite reservoir needs to be discretized. In comparison, the present integral equation scheme only discretizes the planar fracture surface, which is a much reduced numerical solution system. Although the solution is in the Laplace domain, numerical inversion [55] can easily be performed without adding significant computational effort. It should be emphasized that previous studies of fracture response have been based on a different conceptual model namely that of a conventional hydraulic fracture growth. The focus of this work has been on fracture slip, a phenomenon that is generally believed to be true for geothermal reservoirs.

Acknowledgment

This project was supported by the US Department of Energy Office of Energy Efficiency and Renewable Energy under Cooperative Agreement DE-FC07-01ID14186. This support does not constitute an endorsement by the US Department of Energy of the views expressed in this publication. The financial support of the University of North Dakota and Texas A&M University are gratefully acknowledged.

References

[1] Rutledge JT, Phillips WS, Schuessler BK. Reservoir characterization using oil-production-induced microseismicity, Clinton County, Kentucky. *Tectono* 1998;**289**:129–52.

[2] Gutierrez-Negrin LCA, Quijano-Leon JL. Analysis of seismicity in the Los Humeros, Mexico geothermal field. *Geoth Res Council Trans* 2003;**28**:467–72.

[3] Pine RJ, Batchelor AS. Downward migration of shearing in jointed rock during hydraulic injections. *Int J Rock Mech Min Sci* 1984;**21**(5):249–63.

[4] Bommer JJ, Oates S, Cepeda JM, Lindolm C, Bird J, Torres R, et al. Control of hazard due to seismicity, induced by a hot fractured rock geothermal project. *Eng Geol* 2006;**83**:287–306.

[5] Ghassemi A, Zhang Q, Poro-thermoelastic mechanisms in wellbore stability & reservoir stimulation. In: Proceedings of the 29th workshop on geothermal reservoir engineering, Stanford University, CA, 2004.

[6] Segall P, Fitzgerald SD. A note on induced stress changes in hydrocarbon and geothermal reservoirs. *Tectono* 1998;**289**:117–28.

[7] Mossop A. Seismicity, Subsidence and strain at the Geysers geothermal field. PhD Dissertation, Stanford University; 2001.

[8] Segall P. Earthquakes triggered by fluid extraction. *Geol* 1989;**17**:942–6.

[9] Rudnicki JW. Alteration of regional stress by reservoirs and other inhomogeneities: stabilizing or destabilizing? In: Proceedings of the ninth international congress on rock mechanics, Paris, France, 1999. p. 1629–37.

[10] Germanovich LN, Chanpura RA, Ring LM, Filippov AG. Poroelastic mechanism of fault reactivation as a result of reservoir depletion. In: Proceedings of the Biot conference on poromechanics, 1998. p. 415–20.

[11] Bruel D. Impact of induced thermal stresses during circulation tests in an engineered fractured geothermal reservoir; example of the Soultzsous-Forets European Hot Fractured rock Geothermal Project, Rhine Graben, France. *Oil and Gas Sci Tech Rev IFP* 2002;**57**:459–70.

[12] Petty S. Thermal stimulation of well 83-16. In: Rose P, editor. EGS Quarterly Report, University of Utah Energy and Geoscience Institute, December 2002.

[13] Ghassemi A, Zhang Q. Poro-thermoelastic response of a stationary crack using the displacement discontinuity method. *ASCE J Eng Mech* 2006;**132**(1):26–33.

[14] Read RS. 20 years of excavation response studies at AECL's underground research laboratory. *Int J Rock Mech Min Sci* 2004;**41**:1251–75.

[15] Cornet FH, Jianmin Y. Analysis of induced seismicity for stress field determination and pore pressure mapping. *Pure Appl Geophys* 1995;**145**(3/4):677–700.

[16] Cornet FH, Helm J, Poitrenaud H, Etchecopar A. Seismic and aseismic slips induced by large-scale fluid injection. *Pure Appl Geophys* 1997;**150**:563–83.

[17] Stark MA. Imaging injected water in the Geysers reservoir using microearthquakes data. *Geoth Res Council Trans* 1990;1697–704.

[18] Scottie O, Cornet FH. In situ evidence for fluid-induced aseismic slip events along fault zones. *Int J Rock Mech Min Sci* 1994;**31**(4):347–58.

[19] Nowacki W. Thermoelasticity. New York: Pergamon Press; 1973.

[20] Fredrich JT, Wong T-F. Mechanics of thermally induced cracking in three crustal rocks. *J Geophys Res* 1986;**91**(B12):12743–54.

[21] Stephens G, Voight B. Hydraulic fracturing theory for conditions of thermal stress. *Int J Rock Mech Min Sci* 1982;**19**:279–84.

[22] Hagoort J, Weatherill BD, Settari A. Modeling the propagation of waterflood-induced hydraulic fractures. *SPE J* 1980;**8**:293–303.

[23] Perkins TK, Gonzalez JA. The effect of thermoelastic stress on injection well fracturing. *SPE J* 1985;**2**:78–88.

[24] Bodvarsson G. Thermoelastic phenomena in geothermal systems. In: Proceedings of the second UN symposium on the development and use of geothermal resources, San Francisco, CA; 1976. p. 903–7.

[25] Bodvarsson G, Lowell RP. Ocean-floor heat flow and the circulation of interstitial waters. *J Geophys Res* 1972;**77**:4472–5.

[26] Knapp RB, Norton D. Preliminary numerical analysis of processes related to magma crystallization and stress evolution in cooling pluton environments. *Am J Sci* 1981;**281**:35–68.

[27] Lister DRB. On the penetration of water into hot rocks. *Royal Astron Soc Geophys J* 1974;**39**:465–509.

[28] Lister DRB. On the thermal balance of a mid-ocean ridge. *Royal Soc Geophys J* 1972;**26**:515–35.

[29] Lowell RP. Thermoelasticity and the formation of black smokers. *Geophys Res Lett* 1990;**17**:709–12.

[30] Elsworth D. Thermal permeability enhancement of blocky rocks: one-dimensional flows. *Int J Rock Mech Min Sci* 1989;**26**(3/4):329–39.

[31] Lowell RP, Van Cappellen P, Germanovich LN. Silica precipitation in fractures and the evolution of permeability in hydrothermal upflow zones. *Science* 1993;**260**:192–4.

[32] Nygren A, Ghassemi A. Coupled poroelastic and thermoelastic effects of injection into a geothermal reservoir. In: Proceedings of the 40th US rock mechanics symposium, Golden, CO, 2006.

[33] Nygren A, Ghassemi A, Cheng AH-D. Effects of cold-water injection on fracture aperture and injection pressure. *Geoth Res Council Trans* 2005;**29**:183–7.

[34] Nygren A, Ghassemi A. Influence of cold water injection on critically stressed fractures in Coso geothermal field, CA. In: Proceedings of the 39th US rock mechanics symposium, Anchorage, Alaska, 2005.

[35] Ghassemi A, Tarasovs S, Cheng AH-D. An integral equation method for modeling three-dimensional heat extraction from a fracture in hot dry rock. *Int J Numer Anal Methods Geomech* 2003;**27**:989–1004.

[36] Heuer N, Kupper T, Windelberg D. Mathematical model of a hot dry rock system. *Geophys J Int* 1991;**105**:659–64.

[37] Hopkirk RJ, Sharma D, Pralong PJ. Coupled convective and conductive heat transfer in the analysis of hot dry rock geothermal sources. In: Numerical methods in heat transfer. New York: Wiley; 1981. p. 261–307.

[38] Kohl T, Evans KF, Hopkirk RJ, Ryback L. Coupled hydraulic, thermal, and mechanical considerations for the simulation of hot dry rock reservoirs. *Geothermics* 1995;**24**:345–59.

[39] Kolditz O, Clauser C. Numerical simulation of flow and heat transfer in fractured crystalline rocks: application to the hot dry rock site in Rosemanowes (UK). *Geothermics* 1998;**27**:1–23.

[40] Nemat-Nasser S, Ohtsubo H. Fluid flow and heat transfer through hydraulically induced fractures in hot dry rock masses. *ASME J Pressure Vessel Tech* 1978;**100**:277–84.

[41] Willis-Richards J, Watanabe K, Takahashi H. Progress toward a stochastic rock mechanics model of engineered geothermal systems. *J Geophys Res* 1996;**101**(B8):17481–96.

[42] Megel T, Kohl T, Rose P. Reservoir modeling for stimulation planning at the Coso EGS project. *Geoth Res Council Trans* 2005;**29**:173–6.

[43] Ghassemi A, Tarasovs S, Cheng AH-D. Integral equation solution of heat extraction induced thermal stress in enhanced geothermal reservoirs. *Int J Num Anal Methods in Geomech* 2005;**29**:829–44.

[44] Crouch SL, Starfield AM. Boundary element methods in solid mechanics. New York: Allen Unwin; 1983.

[45] Ghassemi A, Roegiers J-C. A three-dimensional poroelastic hydraulic fracture simulator using the displacement discontinuity method. In: Proceedings of the 2nd North American rock mechanics symposium, Montreal, Canada, 1996, p. 982–7.

[46] Kuriyama K, Mizuta Y. Three-dimensional elastic analysis by the displacement discontinuity method with boundary division into triangular leaf elements. *Int J Rock Mech Min Sci* 1993;**30**(2):111–23.

[47] Vandamme L, Curran JH. A three-dimensional hydraulic fracturing simulator. *Int J Numer Methods Eng* 1989;**28**:909–27.

[48] Sekine H, Mura T. Characterization of a penny-shaped reservoir in a hot dry rock. *J Geophys Res* 1980;**85**(B7):3811–6.

[49] Schon JH. Physical properties of rocks: fundamentals and principles of petrophysics. In: seismic exploration, vol. 18. Netherlands: Pergamon Press; 1996.

[50] Bodvarsson G, Tsang CF. Injection and thermal breakthrough in fractured geothermal reservoirs. *J Geophys Res* 1982;**87**:1031–48.

[51] Kruger P, Dyadkin YD, Gendler S, Artemieva E, Smirnova N. Comparison of thermal cooldown estimates in the Russkie Komarovtsy petrogeothermal reservoir. In: Proceedings of the 16th workshop on geothermal reservoir engineering, Stanford University, CA, 1991.

[52] Kolditz O. Modelling flow and heat transfer in fractured rocks: dimensional effect of matrix heat diffusion. *Geothermics* 1995;**24**:421–37.

[53] Cheng AH-D, Ghassemi A, Detournay E. A two-dimensional solution for heat extraction from a fracture in hot dry rock. *Int J Numer Anal Methods Geomech* 2001;**25**:1327–38.

[54] Stehfest H. Numerical inversion of Laplace transforms. *Commun ACM* 1970;**13**:47–9.

[55] Cheng AH-D, Sidauruk P, Abousleiman Y. Approximate inversion of the Laplace transform. *Mathematica J* 1994;**4**:76–82.

[56] Curran JH, Vandamme L. Numerical modeling of the stress and displacement fields around two- and three-dimensional cracks. In: Proceedings of the 25th US rock mechanics symposium, Evanston, Illinois, 1984, p. 223–30.

[57] Julian BR, Foulger GR, Richards-Dinger K, Monastero F. Timedependent seismic tomography of the Coso geothermal area, 1996–2004. In: Proceedings of the 31st workshop on geothermal reservoir engineering, Stanford University, CA, 2006.